



UNIVERSITÀ DEGLI STUDI
DI TRENTO

DEPARTMENT OF INFORMATION ENGINEERING AND COMPUTER
SCIENCE
ICT International Doctoral School
34th cycle
PhD Dissertation

DEVELOPMENT OF NOVEL APPROACHES TO
SNOW PARAMETER RETRIEVAL IN ALPINE
AREAS BY USING MULTI-TEMPORAL AND
MULTI-SENSOR REMOTE SENSING IMAGES

Valentina Premier

Advisor: **Prof. Lorenzo Bruzzone**
RSLab, University of Trento
Co-advisors: **Dr. Ing. Carlo Marin**
Dr. Claudia Notarnicola
Institute for Earth Observation, Eurac Research

July 2022

Abstract

Snow represents an important resource in mountainous regions. Monitoring its extent and amount is relevant for several applications, such as hydrology, ecology, avalanche monitoring, or hydropower production. However, a correct understanding of the high spatial and temporal variability of snow accumulation, redistribution and ablation processes requires its monitoring in a spatialized and detailed way. Recently, the launch of the Sentinel missions has opened the doors to new approaches that mainly exploit high resolution (HR) data having a spatial detail of few dozens of m. In this thesis, we aimed at exploiting these new sources of information to retrieve important parameters related to the snowmelt processes. In detail, we i) investigated the use of Sentinel-1 Synthetic Aperture Radar (SAR) observations to evaluate snowmelt dynamics in alpine regions, ii) developed a novel approach based on a hierarchical multi-resolution analysis of optical time-series to reconstruct the daily HR snow cover area (SCA), and iii) explored the combination of HR SCA time-series, SAR snowmelt information and other multi-source data to reconstruct a daily HR snow water equivalent (SWE) time-series. In detail, in the first work we analyzed the relationship between the snowmelt phases of a snowpack and the multi-temporal SAR backscattering. We found that the SAR is able to provide useful information about the moistening, ripening and runoff phases. In the second work, we exploited the snow pattern repetition on an inter-annual basis driven by the geomorphological features of a study area to carry out historical analyses. Thus, we took advantage of these repetited patterns to fuse low resolution and HR satellite optical data and set up a gap filling to derive daily HR snow cover area (SCA) time-series. These two research works are the pillars for the last contribution, which aims at combining all these information sources together with both in-situ data and a simple yet robust degree day model that provides an estimate of the potential melting to derive daily HR SWE time-series. These final results have an unprecedented spatial detail, that allows to sample the phenomena linked to the complex snow accumulation, redistribution and ablation processes with the required spatial and temporal resolution. The methodology and the results of each experimental work are illustrated and discussed in detail in the chapters of this thesis, with a look on further research and potential applications.

Keywords: Snowmelt, Snow Water Equivalent, Snow Cover Area, Sentinel missions, Multi-temporal, Multi-source

Acknowledgement

I would like to acknowledge all the people that supported these years of PhD work. In particular, my deepest thanks go to Carlo, that has been a friendly supervisor, always calm and open to discussion, available daily (often also out of the normal working hours) despite the distance imposed by the Covid situation. Thanks for having shared with me some of your knowledge and passion about the topic! A big thank to Lorenzo for welcoming me in the RSLab group. There, I had the chance to meet nice and prepared people working on topics that I did not even know existed before! Thank you especially for your professional support. Also, thanks to Claudia for being a very human boss that has contributed in making the working environment very pleasant. A special mention goes also to my PhD colleagues Paulina and Riccardo, that have shared with me not only the office but also a lot of thoughts. Your preparation and hard work have contributed to motivate me! Tanks also to all other Eurac's colleagues that have contributed to make my days more enjoyable with cakes and nice talks. Last but not least, I thank my parents that have always lovely supported me.

Contents

List of Figures	viii
List of Tables	x
List of Abbreviations	xiii
1 Fundamentals and Background	7
1.1 Physics of Snow	7
1.2 Ground Observations	9
1.3 Remote Sensing of Snow	11
2 Use of Sentinel-1 Radar Observations to Evaluate Snowmelt Dynamics in Alpine Regions	14
2.1 Introduction	15
2.2 Background	18
2.2.1 Snow melting process	18
2.2.2 SAR backscattering response to wet snow	20
2.3 Dataset description	22
2.3.1 Test sites description, and in situ data	22
Zugspitze (Werdenfeller Alps, Germany)	24
Alpe del Tumulo (South Tyrol, Italy)	24
Clozner Loch (South Tyrol, Italy)	25
Malga Fadner (South Tyrol, Italy)	25
Weissfluhjoch (Graubünden, Switzerland)	25
2.3.2 SNOWPACK model set up	25
2.3.3 Remote sensing observations	27
2.4 Data analysis and proposed approach to the melting phases identification from S1	27
2.4.1 Data analysis	28
Zugspitze	32
Alpe del Tumulo	33
Clozner Loch	33
Malga Fadner	34
Weissfluhjoch	34
2.4.2 Temporal Evolution of the Backscattering	35
2.5 Application of the proposed approach to 1D and 2D cases	38

2.5.1	Identification of snow phases from Sentinel-1 in the five alpine test sites	38
2.5.2	Extension to a 2D analysis of the runoff onset: the Zugspitzplatt catchment	40
2.6	Discussion	40
2.7	Conclusions	44
3	A Novel Approach Based on a Hierarchical Multi-Resolution Analysis of Optical Time Series to Reconstruct the Daily High-Resolution Snow Cover Area	46
3.1	Introduction	47
3.2	Proposed Method	51
3.2.1	Gap-filling driven by the historical HR snow pattern persistence	54
3.2.2	Downscaling driven by the LR historical snow pattern persistence	55
3.2.3	Spatial correction of SCF	56
3.2.4	Temporal interpolation of SCF	57
3.2.5	GAM based reconstruction	57
3.3	Dataset Description	59
3.4	Experimental Results	61
3.4.1	Results of the Gap-filling	61
3.4.2	Results of the Downscaling	64
3.4.3	Results of the GAM	67
3.4.4	Results of the Full Proposed Method	69
3.5	Discussion	74
3.6	Conclusion	75
4	Exploring the Use of Multi-source High-Resolution Satellite Data for Snow Water Equivalent Reconstruction over Mountainous Catchments	77
4.1	Introduction	78
4.2	Proposed approach to HR SWE reconstruction	81
4.2.1	Identification of the catchment state	82
4.2.2	Characterization of the snow season from regularized SCA time-series	85
4.2.3	HR SWE reconstruction	89
4.3	Study Areas and Dataset Description	90
4.4	Experimental Results	93
4.4.1	South Fork catchment	93
4.4.2	Schnals catchment	97
4.5	Discussion	99
4.5.1	Error in the determination of the catchment state	99
4.5.2	Error in the SCA derivation and regularization	101
4.5.3	Error in the SWE reconstruction	102
4.6	Conclusions	105

Appendices	127
A Supplementary Material to Chapter 4	127
A.1 In-situ snow measurements	127
A.2 Degree day estimation	127
A.3 SWE results for the South Fork catchment	128

List of Figures

1	Overview of some of the main satellite missions that are of interest for snow monitoring. It is possible to notice that during the years, there has been an improvement in terms of both spatial and temporal resolution.	3
1.1	Principal physical processes that affect snow. Image inspired by SLF (see https://www.wsl.ch/en/services-et-produits/logiciels-sites-internets-et-apps/snowpack.html)	10
1.2	Example of a traditional snow pit analysis.	11
1.3	Reflectances of different surfaces. Credit: Andreas Kaab, University of Oslo.	12
2.1	Example of transitions in snow status during the melting season obtained by sampling the snow in the morning (M), when the S1 descending observations are taken, and in the evening (A) when the S1 ascending data are taken. The upper part of the figure illustrates the simplified temporal transportation of the free liquid water (blue area) in the dry snowpack (white area). The lower part of the figure illustrates the respective temporal evolution of LWC (yellow line) and SWE (red line). In detail, by starting from a dry situation, the liquid water is introduced into the snowpack by either a rain event or the melt due to the incoming flux of shortwave radiation. In this moistening phase the LWC (yellow line) varies with a diurnal cycle. Repeated cycles of partial melting and refreezing lead the snowpack to the isothermal state. During the ripening period, a combination of different situations can occur depending on the weather conditions but an increasing trend of the LWC is visible. Once the snowpack is isothermal and it cannot retain water anymore, it starts to produce water output until it melts totally. This last phase starts with a significant decrease of the SWE (red line).	19
2.2	Main SAR backscattering mechanisms in presence of dry and wet snow at C-band. The dry snow is almost transparent, and the radar echo can penetrate the snow for several meters. The presence of LWC, causes high dielectric loss, which increases the absorption coefficient.	21

2.3	Overview map with the five stations located in Germany (Zugspitze), Switzerland (Weissfluhjoch) and Italy (Malga Fadner, Clozner Loch and Alpe Tumulo) used for the presented study (©2019 Microsoft Corporation ©2019 Digital Globe ©CNES(2019) Distribution Airbus DS). The red points indicate the exact location of the stations. The black squares indicate the S1 footprints. The footprints were selected in order to minimize any possible interference of the EM wave with the homemade structures but maintaining a certain correlation with the in situ measurements. The panoramic images give an idea about the land cover type and the topography around the stations.	23
2.4	Temporal evolution of the coefficient of backscattering acquired over the five test sites. The two polarization VV (continuous line) and VH (dashed line) are reported for the different available tracks with different colours. It is compared to LWC and SWE measured in situ at the stations (when available) and modeled with SNOWPACK (contains modified Copernicus Sentinel data, 2016/2018, processed by Eurac Research). The three phases during the melting have been identified from the in situ/modeled data. The first phase of moistening is reported in light yellow, the ripening phase in light red and the runoff in light green. For all the test sites we found that the multi-temporal SAR measurements confirm the identification of the three melting phases. In detail, we systematically found that the SAR backscattering decreases as soon the snow starts containing water and increases as soon as SWE starts decreasing, which corresponds to the release of meltwater from the snowpack.	30
2.5	Schematic representation of the evolution of the backscattering coefficient acquired in the morning (green line) and in the afternoon (blue line) compared with LWC (yellow line) and SWE (red line) evolution. The offset between the morning and afternoon signals is due to the generally different local incidence angle of the ascending and descending acquisitions in mountainous regions. The three melting phases are identified from the LWC and SWE information. Correspondingly, the rules for the identification of each phase from the time series of σ^0 is highlighted: a decreases of at least T [dB] from the mean value in dry snow condition applied to the afternoon and morning signals identifies the moistening and ripening onsets respectively. The local minima of the signals indicate the runoff onset.	35

2.6	Runoff onset for the Zugspitzplatt catchment. (a) Test site presentation (©2019 Microsoft Corporation ©2019 Digital Globe ©CNES(2019) Distribution Airbus DS) (b) Map of the runoff onset (contains modified Copernicus Sentinel data, 2018, processed by Eurac Research). The runoff started at lower altitude and at the south exposed slopes. The last areas to have the runoff in the catchment are the high-altitude area, the north exposed and glacierized areas. (c) The multi-temporal backscattering time series for the selected points along the transect identified in (b) with red dots. All the time series present the characteristic “U-shaped” pattern.	41
3.1	Problem definition. We consider three spatial levels: i) the catchment scale, defined by the HR and LR pixel included in the geographical area of the catchment (grey line, black pixel are masked out), for which we can calculate the SCA, i.e., the fraction of the catchment covered by snow; ii) the low-resolution scale and the associated SCF calculated for each LR pixel X_j , i.e., the fraction of a LR pixel covered by snow; and iii) the high-resolution scale, in which each HR pixel x_i is binary classified either as ω_s or ω_{sf} . Note that HR pixels are spatially resampled and aligned to fit within the LR pixel.	52
3.2	Workflow of the proposed method. It is composed by two main blocks, i.e., the historical block (gap-filling, correction and downscaling) and the GAM block (GAM and final correction). The two blocks are joined by an intermediate step composed of the interpolation and correction.	53
3.3	Gap-filling: historical statistical analysis to infer the snow presence conditioned by the partial SCA. First, the cloud mask of the date to be reconstructed is applied to the entire HR TS. The dates with similar \widehat{SCA} are then used to compute the CP (Eq. 3.3) and infer the HR label (Eq. 3.4).	54
3.4	Downscaling: historical statistical analysis to infer the snow presence given the LR SCF. Given a LR acquisition on the date to be down-scaled, we consider SCF_{LR} for each LR pixel X_j . We aggregate the HR TS (Eq. 3.1 and we select the P pixels which show a similar SCF for X_j . Hence we compute the CP (Eq. 3.5 and we perform the downscaling (Eq. 3.6).	55
3.5	Example of spatial correction of SCF. It is applied to a $SCF_{LR,j}$ (observed or interpolated) when classified HR pixels within the considered pixel X_j are available.	56
3.6	Overview of the study area: a catchment located in the Sierra Nevada, California. The DTM is represented on the right.	60
3.7	Example of the application of the gap-filling step to infer the snow presence conditioned by the partial cloud-free SCA: (a) reference image, (b) artificial cloud mask before the cloud filling procedure applied to elevations between 2800 e 3300 m, (c) conditional probability map, and (d) results after the gap-filling procedure.	63

3.8	Performances achieved by the gap-filling step. The plot shows the overall accuracy (OA) (solid lines –) and the reconstructed pixels (dashed lines - -) for variable cloud masks and variable T_δ thresholds. The percentage of the reconstructed pixels is calculated w.r.t. the cloud covered area. $T_S = 10$ is used.	63
3.9	Example of the application of the gap-filling step to infer the snow presence conditioned by the partial cloud-free SCA: (a) reference image, (b) artificial cloud mask before the cloud filling procedure applied to elevations lower than 2800 m, (c) conditional probability map, and (d) results after the gap-filling procedure.	64
3.10	Example of the application of the proposed reconstruction step to downscale the SCF: (a) SCF map to be downscaled, (b) conditional probability map, and (c) map downscaled with the proposed method.	65
3.11	Sensitivity analysis for the downscaling step. OA (solid line –) and the percentage of reconstructed pixels (dashed line - -) for: (a) different discretization steps $\Delta_{SCF,HR}$, (b) different threshold values T_P for the number of considered pixels, and (c) different buffer size ε for the CP computation (see Eq. 3.5). The trends are shown for different scan angles θ	66
3.12	Overall accuracy (OA) of the proposed downscaling and SCF_{LR} RMSE trends for the LR dataset with $\theta \leq 20$. RMSE is calculated between SCF_{LR} and SCF_{HR} . $\Delta_{SCF,HR} = 10\%$, $T_P = 10$ and $\varepsilon = 10\%$ are chosen.	67
3.13	Partial dependence plots for the features used for the GAM model, i.e., elevation, slope and aspect. The blue continuous lines represent the smoothing functions and the red dashed lines represent the 95% confidence intervals. The y-axes have been fixed to the scale of the CP ($P(\omega_s SCF)$) which is the feature that shows the largest predicted outcome.	68
3.14	Performances achieved by three considered reconstruction approaches: i) standalone history, i.e., reconstruction with the historical block and application of a threshold (0.5) to the CP; ii) standalone GAM, i.e., GAM trained on all the CPs resulting from the historical block (also when equal to 0 or 1) without direct reconstruction in the historical block; iii) the proposed method, i.e., reconstruction with the historical block and, later, with GAM.	69
3.15	False color composition (R:SWIR,G:NIR,B:RED) (a-d) and reference map (g) for three reconstructed dates. Results before (b-e-h) and after applying the GAM (c-f-i) in terms of overall accuracy (OA) and reconstructed pixels (REC). True positive (TP) in dark green, true negative (TN) in light green, false positive (FP) in red, false negative (FN) in orange, and no data in white.	72

3.16	SCA trends and measured SWE at the Volcanic Knob station for the hydrological seasons 2017-18 (a-b-c), 2018-19 (d-e-f) and 2019-20 (g-h-i). The reconstructed SCA is compared with the SCA observations from the HR (a-d-g) and LR acquisitions (b-e-h), with relative SCA (orange dots) and cloud percentage (vertical olive line). The validation dates are also indicated with a black x.	73
4.1	Workflow of the proposed approach showing the three main steps: i) state identification, ii) characterization of snow season from SCA, and iii) SWE reconstruction. The inputs are: i) a HR SCA time-series and daily spatialized DD maps derived from AWS, ii) SAR backscattering time-series, and iii) SWE or HS from automatic weather stations (AWS). As output, we obtain the daily HR SWE maps.	82
4.2	Definition of the three possible catchment states: <i>accumulation</i> , <i>ablation</i> and <i>equilibrium</i> . The description of the possible events that characterize the catchment between two consecutive dates is reported together with the difference in terms of SWE and SCA. As one can notice only ΔSWE can be used to unambiguously identify the three states. The illustrations represent the SCA in an idealized catchment where white and brown areas are the <i>snow</i> and <i>snow-free</i> areas, respectively and the dashed lines represent the contour lines.	84
4.3	Illustration of the reconstruction and temporal reallocation of the SWE for a given pixel. Starting from the left side of the figure, the catchment state is identified for each day of the snow season (delimited by t_{SA} and t_{SD}) and the potential melting is estimated according to Eq.4.1. The sum of all the potential melting at the different days represent the total amount of SWE for that pixel. This is redistributed during the <i>accumulation</i> day using Eq.4.4. For this illustrative example, a constant k is considered. As one can notice the reconstructed SWE can represent <i>accumulation</i> (even as late spring snowfall), <i>ablation</i> and <i>equilibrium</i> conditions.	91
4.4	Overview of the two test sites: a) South Fork catchment, California, USA, and b) Schnals catchment, South Tyrol, Italy (©2022 Google Maps).	92
4.5	Proposed SWE map (on the left), ASO SWE map (in the centre) and bias map calculated as difference between the proposed and ASO SWE (on the right) for the 9th of June 2019. A zoom is shown under the correspondent maps. A transect is shown with three green dots in the North area of the catchment (©2022 Google Maps).	94
4.6	SWE temporal trends for: the proposed approach (continuous lines) and ASO (crosses) for the considered transect reported in Fig. 4.5.	94
4.7	SWE obtained by the proposed approach (in orange) against the measured SWE (in blue) at the Volcanic Knob test site for the hydrological seasons a) 2018/19, b) 2019/20 and c) 2020/21.	96
4.8	Temporal trends of the total SWE for the South Fork catchment over the three analyzed seasons. Crosses represent the ASO reference.	96

4.9	Trends of the maximum of SWE for the hydrological seasons 2018-2021 w.r.t. the elevation (up), slope (centre) and aspect (low) for the South Fork catchment.	98
4.10	SWE proposed (continuous line) against the manual measured SWE (crosses) at some locations in the Schnals catchment (see Fig. A.1).	98
4.11	Maximum of SWE for the Schnals catchment for the hydrological seasons a) 2019/20 and b) 2020/21.	99
4.12	Trends of the maximum of SWE for the hydrological seasons 2019-2021 w.r.t. the elevation (up), slope (centre) and aspect (low) for the Schnals catchment.	100
4.13	SWE for the Schnals catchment for the hydrological seasons 2019-2021. Continuous lines represent SWE, dashed lines represent the discharge measured at Schnalsbach - Gerstgras.	100
4.14	SCA time-series in the South Fork catchment for the hydrological seasons a) 2018/19, b) 2019/20 and c) 2020/21. Original input version (in blue) and corrected version (in orange) after the application of the proposed regularization. The background colors correspond to the ablation state (in cyan) and the accumulation state (in pink).	103
4.15	SCA time-series in the Schnals catchment for the hydrological seasons a) 2019/20 and b) 2020/21. Original input version (in blue) and corrected version (in orange) after the application of the proposed post-filter. The background colors correspond to the ablation state (in cyan) and the accumulation state (in pink).	104
4.16	Example of a regularized snow map on the date 12/01/2020 for the South Fork catchment: a) false-color composition (R:SWIR,G:NIR,B:RED), b) input snow cover map, and c) regularized snow cover map.	104
A.1	Overview of the measurements ((©)2022 Google Maps).	128
A.2	Leave-one-out cross validation results for the South Fork catchment for the hydrological seasons a) 2018/19, b) 2019/20 and c) 2020/21.	128
A.3	Leave-one-out cross validation results for the Schnals catchment for the hydrological seasons a) 2019/20 and b) 2020/21).	128
A.4	Proposed SWE (left), ASO SWE (centre) and bias (right) for the 12 analyzed dates over the three hydrological season (2018-2021) for the South Fork catchment. ((©)2022 Google Maps)	133
A.4	Proposed SWE (left), ASO SWE (centre) and bias (right) for the 12 analyzed dates over the three hydrological season (2018-2021) for the South Fork catchment (cont.). ((©)2022 Google Maps)	134
A.4	Proposed SWE (left), ASO SWE (centre) and bias (right) for the 12 analyzed dates over the three hydrological season (2018-2021) for the South Fork catchment (cont.). ((©)2022 Google Maps)	135
A.4	Proposed SWE (left), ASO SWE (centre) and bias (right) for the 12 analyzed dates over the three hydrological season (2018-2021) for the South Fork catchment (cont.). ((©)2022 Google Maps)	136

A.5	Total SWE [Gt] distributed for each elevation, slope and aspect belt. The proposed product (in yellow) is evaluated against ASO (in blue) for the 12 analyzed dates over the three hydrological season (2018-2021) for the South Fork catchment.	137
A.5	Total SWE [Gt] distributed for each elevation, slope and aspect belt. The proposed product (in yellow) is evaluated against ASO (in blue) for the 12 analyzed dates over the three hydrological season (2018-2021) for the South Fork catchment (cont.).	138
A.6	Boxplots of the bias calculated as the SWE generated by the proposed approach minus the ASO product for each elevation, slope and aspect belt. The results are represented for the 12 analyzed dates over the three hydrological season (2018-2021) for the South Fork catchment. .	139
A.6	Boxplots of the bias calculated as the SWE generated by the proposed approach minus the ASO product for each elevation, slope and aspect belt. The results are represented for the 12 analyzed dates over the three hydrological season (2018-2021) for the South Fork catchment (cont.).	140

List of Tables

2.1	Simplified SAR backscattering response to wet snow divided in volumetric, σ_{vol}^0 , and surface backscattering, σ_{sup}^0 , contributions. Considering a sufficiently thick snowpack the contribution of σ_{grd}^0 can be neglected.	21
2.2	Details of the meteorological and snow parameters measured at each station. Wind velocity (VW), wind direction (DW), air temperature (TA), relative humidity (RH), snow depth (HS), snow temperature at depth x (TS_x), surface temperature (TSS), soil temperature (TSG), incoming shortwave radiation (ISWR), incoming longwave radiation (ILWR), outgoing shortwave radiation (OSWR), snow water equivalent (SWE), snow density (DS), liquid water content (LWC) and ice content (IC).	22
2.3	SNOWPACK calibration results for each test site. Pearson correlation coefficient (ρ) and the mean absolute error (MAE) have been computed for snow depth (HS), snow temperatures at three different depth TS1 (0 m from the ground), TS2 (0.2 m from the ground), TS3 (0.5 m from the ground) and SWE, according to the availability of the ins situ data.	26
2.4	List of the Sentinel-1 acquisitions and their main characteristics over the five test sites.	28
2.5	Onset times for the melt phases identified in the five test sites using the LWC and SWE (reference - Ref) and Sentinel-1 (S1) with the method proposed in the previous section.	39
3.1	Values of the parameters used in the historical block selected through the experimental sensitivity analysis.	62
3.2	Overview of the scenes considered for the evaluation of the downscaling step considering the different acquisition scanning angles.	65
3.3	Smoothing parameters used for the GAM reconstruction.	68
3.4	Results in terms of OA [%], confusion matrix (CM) and reconstructed pixels obtained by the different blocks of the proposed method on nine dates (three for each hydrological season) evaluated against selected HR scene and five dates evaluated against the ASO dataset. The CM reports the TP, FP, TN and FN (clockwise from the upper left), normalized by row.	70

- 4.1 Results of the comparison between the proposed SWE and ASO products for the South Fork catchment. Bias, RMSE and correlation are calculated pixel-wise. SWE tot is the SWE integrated over space. . . 97

List of Abbreviations

ASO	Airborne Snow Observatory
AVHRR	Advanced Very-High-Resolution Radiometer
AWS	Automatic Weather Stations
BC	Boundary Conditions
CM	Confusion Matrix
CP	Conditional Probability
CRNS	Cosmic-ray neutron sensing
DD	Degree Day
DEM	Digital Elevation Model
DL	Deep Learning
DS	Density of Snow
DW	Direction of Wind
EC	European Commission
EM	Electromagnetic
ESA	European Space Agency
FN	False Negative
FP	False Positive
GAM	Generalized Additive Model
GPS	Global Positioning System
GS	Grain Size
HR	High Resolution
HRU	Hydrological Response Units

HS	Height of Snow
IC	Ice Content
ILWR	Incoming Longwave Radiation
ISWR	Incoming Shortwave Radiation
IW	Interferometric Wide Swath Mode
LIA	Local Incidence Angle
LOO	Leave One Out
LR	Low Resolution
LWC	Liquid Water Content
MAE	Mean Absolute Error
ML	Machine Learning
MODIS	Moderate Resolution Imaging Spectroradiometer
NASA	National Aeronautics and Space Administration
NDSI	Normalized Difference Snow Index
NDVI	Normalized Difference Vegetation Index
NIR	Near infrared (wavelength)
OA	Overall Accuracy
OSWR	Outgoing Shortwave Radiation
RH	Relative Humidity
RMSE	Root Mean Square Error
RS	Remote Sensing
RT	Radiative Transfer
SAR	Synthetic Aperture Radar
SCA	Snow Cover Area
SCF	Snow Cover Fraction
SDC	Snow Depletion Curve
SR	Surface Roughness
SPA	Snowpack Analyzer

SR	Surface Roughness
SVM	Support Vector Machine
SWE	Snow Water Equivalent
SWIR	Shortwave infrared (wavelength)
S1	Sentinel-1
S2	Sentinel-2
TA	Temperature of Air
TN	True Negative
ToA	Top of Atmosphere
TP	True Positive
TS	Time Series
TS_x	Temperature of Snow at Depth x
TSG	Temperature of Snow Ground
TSS	Temperature of Snow Surface
VIS	Visible (wavelength)
VW	Velocity of Wind

Introduction

This chapter offers an introduction to the PhD thesis. The aim of this research is the retrieval of snow parameters through innovative approaches based on remote sensing techniques. We briefly introduce the framework where this thesis has been developed by presenting the topic, a brief overview of the existing techniques and the opportunities that arise by the use of recent satellite missions. This allows to highlight and discuss the motivation, the objectives and the novel contributions of this thesis. Finally, the structure of the document is reported.

Background

Snow is an essential component of the cryosphere. In the Northern Hemisphere, the snow extent can cover more than half of the land area when reaching its maximum annual expansion (Groisman 2001). Consequently, snow cover has a large influence on the global water cycle and climate. In snow dominated regions, snowmelt is the main contributor to streamflow runoff and groundwater recharge affecting much larger downstream areas (MacDonald & Stednick 2003). Indeed, the percentage of snow stored during winter and released as liquid water during spring can represent at least 50% of the total flow sometimes going over 95% (Shafer et al. 1982, Cline 1997). The snow contribution to mountain hydrology is of crucial impact not only for flood predictions but also for its socio-economic impacts, as hydropower contribution (Magnusson et al. 2020) and ski-tourism (Hanzer et al. 2020). Moreover, snow affects the Earth's energy budget due to its interaction with soil and atmosphere. Being snow one important weather and climate forcing, its anomalies in terms of snow cover area (SCA) are essential for evaluating climate change variations (Notarnicola 2020). Nonetheless, changes in SCA also influence the ecosystems (Starr & Oberbauer 2003). Not least, an accurate knowledge of the snowpack is fundamental for avalanche forecasting. Combination of steep slopes, gravity, accumulation and deformation of snow cover and short-term fluctuations in weather phenomena can lead to detachment of large snow masses. The repercussions are damages to transportation, infrastructure, resource industries, private properties and eventually represent a cause of human lives loss (Stethem et al. 2003).

It is obvious that an accurate monitoring of the snow distribution and availability is thus essential for several scopes. In this sense, a key variable is the snow water equivalent (SWE) that represents the total amount of water stored in the snowpack that would be released upon complete melting. This variable is the most important

from a hydrological point of view. Together with other common snow properties, it is traditionally investigated through ground-based observations. However, this approach implies limited spatial coverage and intrinsic difficulties in monitoring remote areas, but provides the best understanding of the environmental physics associated with snow. Mathematical models have also been exploited to represent the physics of the phenomena linking climate forcing and snowpack micro- and macro-structure (Brun et al. 1992, Lehning et al. 1999, Bartelt & Lehning 2002, Lehning et al. 2002). The main drawbacks of such a tool is represented by uncertainties and errors related to model structure (Avanzi et al. 2016), meteorological forcing (Raleigh et al. 2015) and model parameterizations (Engel et al. 2017), that may result in poor model performances.

Remote sensing (RS) represents a valid alternative as well as a complementary information source to ground-based observations and physical modeling. In the last decade, the European Commission (EC) and the European Space Agency (ESA) have financed the launch of the well-known Sentinel missions in the framework of the Copernicus program. This has opened new interesting opportunities, given the improved spatial and temporal resolution of the provided data that are available free-of-charge. In detail, the missions of interest for snow monitoring are:

- the Sentinel-1 (S1) mission that is made up of a constellation of two identical satellites with a C-band SAR mounted on board. The images acquired by S1 have a nominal resolution of 20 m and are acquired in dual-polarization (VV and VH) over Europe. The first satellite (S1A) is operating since April 2014 while the twin (S1B) since April 2016. Hence, starting from this date an acquisition every 6 days is available. However, since December 2021 S1B has experienced a power failure. Hence, S1C is planned to be launched in winter 2022;
- the Sentinel-2 (S2) constellation that is made up of two identical satellites operating a multi-spectral sensor with 13 bands in the visible (VIS), near infrared (NIR), and shortwave infrared (SWIR) parts of the spectrum. The spatial resolution varies from 10 m to 60 m. The first satellite (S2A) is operating starting from June 2015 and the twin (S2B) from March 2017. The revisit time with 2 satellites is about 5 days at the equator and 2-3 days at mid-latitudes.
- the Sentinel-3 (S3) mission that is composed of two twin satellites that carry multiple sensing instruments among which we recall the Sea and Land Surface Temperature Radiometer (SLSTR) and the Ocean and Land Colour Instrument (OLCI). These optical sensors can acquire medium resolution images, i.e., from 300 to 500 m in the VIS, NIR, and SWIR part of the spectrum every day for every location on the Earth. The first satellite was launched in February 2016 and the second one in April 2018.

Beside these recent missions, further datasets are also available to provide long-term observations over the past years. In detail, we cite:

- the Moderate Resolution Imaging Spectroradiometer (MODIS) mounted on Terra and Aqua. These satellites were launched in December 1999 and in May

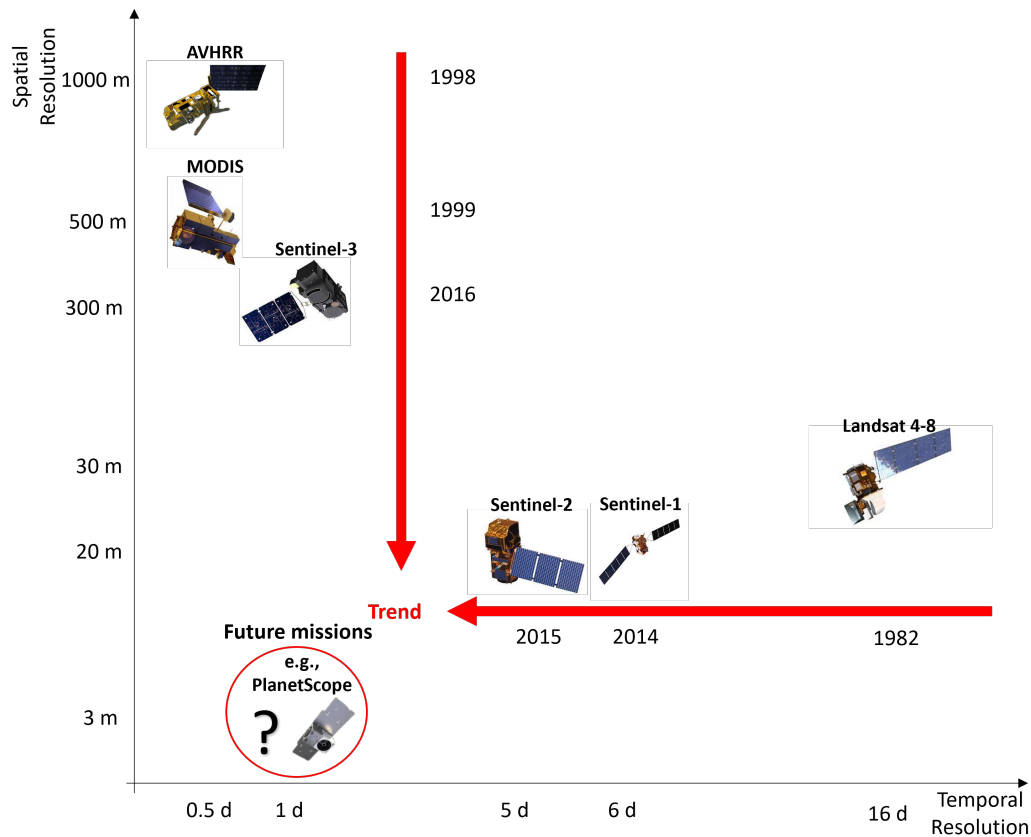


Figure 1: Overview of some of the main satellite missions that are of interest for snow monitoring. It is possible to notice that during the years, there has been an improvement in terms of both spatial and temporal resolution.

2002, respectively, by the National Aeronautics and Space Administration (NASA). The instrument is able to acquire over 36 spectral bands with a spatial resolution of 500 m in the VIS, NIR and SWIR. The two satellites provide two acquisitions per day.

- the Landsat missions, with a total number of 8 satellites that provide high spatial resolution acquisitions. These multi-spectral sensors operate since 1982 (from Landsat-4) with spatial resolution ranging from 15 to 60 m in the VIS, NIR, SWIR and thermal red part of the spectrum and a revisit time of 16 days.

An overview of the most relevant missions for snow monitoring is presented in Fig. 1. Together with the above mentioned missions, we also reported the Advanced Very-High-Resolution Radiometer (AVHRR) instrument that has operated in five spectral bands (red, thermal, mid infrared, and NIR bands) and was mounted on board of different satellites, such as the National Oceanic and Atmospheric Administration (NOAA) Polar-Orbiting Environmental Satellite (POES). Moreover, we reported also the PlanetScope constellation that acquires images with a high spatial

(3 m) and temporal resolution (1 day) but has the disadvantages that it acquires data only over VIS and NIR spectral bands and that images are not available free of charge. However, the increase in spatial and temporal resolution represents a future trend for most of the missions. In this context, it still exists a clear trade-off between spatial and temporal resolutions that needs to be solved by merging information from different satellites. Furthermore, the availability of historical observations together with more recent and improved data - in terms of spatial detail and temporal availability - creates new opportunities for developing novel data fusion methods. In particular, multi-temporal and multi-source data can be integrated in order to fulfill the current gaps in the state-of-the-art methods and develop improved products that are relevant for snow monitoring. Hence, the main aim of this thesis is to provide novel approaches to monitor the snow cover and relevant parameters related to snow hydrology with high spatial and temporal detail. Such a result is needed for a proactive management of the water resources. Moreover, an improvement in terms of spatial and temporal resolution provides not only a meaningful information for countless environmental applications but also a tool to better understand the complexity and heterogeneity of the environmental phenomena that govern the snow cover evolution.

Thesis Objectives and Contributions

In this thesis we aim at developing novel approaches based on RS techniques to derive relevant information about the snow accumulation and melting, with the final scope to derive a high detail information about SWE distribution. As mentioned in the previous section, this is a variable of great interest for most of the applications. However, as we will explain more in detail through the thesis, the state-of-the-art methods developed so far for SWE retrieval are in general not able to extract sufficient spatial and temporal detail as required for an accurate monitoring of this important parameter. Advancements in terms of both spatial and temporal resolution are important to depict the high spatial variability of snow accumulation, redistribution and melting phenomena. These are linked to both the high heterogeneity of weather forcings as well as the geomorphological features of the analysed area. Hence, RS represents an excellent tool in this sense. The recent context of large data availability coming from heterogeneous sources has opened the doors to development of novel approaches that exploit the large amount of multi-temporal and multi-source data that we have. Hence, the main objective of this thesis is to overcome the limitations of the current state-of-the-art methods by exploiting data from new missions that represent a step forward in terms of spatial and temporal resolution as presented in the previous section. Moreover, the results of this thesis are developed in the future perspective of a data assimilation framework where RS and in-situ observations are used together with physically based models since all these outcomes should go hand in hand, always keeping in mind the physical processes that drive the phenomena. In the following subsections the main objectives and novelties for each contribution of the thesis will be briefly described.

Use of Sentinel-1 Radar Observations to Evaluate Snowmelt Dynamics in Alpine Regions

A correct understanding of the characteristics of the snowpack requires a proper information about the snowmelt and the runoff timing. This information is essential for many hydrological applications and especially in the context of SWE retrieval. The Synthetic Aperture Radar (SAR) mounted on board of the S1 mission offers the opportunity to retrieve information about the snowpack status with a temporal and spatial accuracy never seen before. Indeed, it is highly sensitive to the LWC of the snowpack. The high sampling time (e.g., 6 days) allows to set up a multi-temporal analysis between the SAR backscattering and the key snow properties, as LWC and SWE, with an unprecedented spatial detail. This allows us to identify the three melting phases that characterize the melting process, i.e., moistening, ripening and runoff. In detail, we can observe that the C-band SAR backscattering decreases as soon as the snow starts containing liquid water, and that the backscattering increases as soon as SWE starts decreasing, which corresponds to the release of meltwater from the snowpack. A set of simple rules is defined to identify the melting phases starting from the multi-temporal SAR backscattering. The S1 backscattering is compared with snow properties derived from in-situ observations and physically-based snow modeling simulations for five alpine test sites in Italy, Germany and Switzerland considering two hydrological years showing a good agreement. A spatially-distributed application of the identification of the runoff onset from SAR images for a mountain catchment, i.e., the Zugspitze catchment in Germany, is also proposed. The results show great potentiality being able to well represent the spatial and temporal variability of the snowmelt over large regions.

A Novel Approach Based on a Hierarchical Multi-Resolution Analysis of Optical Time Series to Reconstruct the Daily High-Resolution Snow Cover Area

The snow cover area (SCA) is also a relevant preliminary input for retrieving an accurate information about the extent of the snow cover and, in turn, on its persistence on the ground. Given the large variability of the snow cover dynamics, a proper monitoring requires daily and high spatial resolution sampling. However, the current satellite missions do not provide such observations. We propose a novel approach that merges multi-source and multi-scale acquisitions to infer the daily HR snow cover area for mountainous basins. The approach is based on the assumption that inter-annual snow patterns are both affected by the local geomorphometry and meteorology. To derive these patterns, we exploit a hierarchical multi-step approach based on historical statistical analyses on a long and sparse HR time-series. The inference is secondly reinforced by using a generalized additive model (GAM) that exploits not only the historical data but also explicit geomorphometric, global snow and multi-temporal properties. The results show an average overall accuracy of 92% when evaluated in a catchment in the Sierra Nevada, USA, for three hydrological years (2017-2019).

Exploring the Use of Multi-source High-Resolution Satellite Data for Snow Water Equivalent Reconstruction over Mountainous Catchments

The information derived in the previous works can be exploited with the final purpose to retrieve the snow water equivalent (SWE) that represents the variable of greatest hydrological interest. Multi-source data are exploited here to reconstruct daily SWE time-series at a final spatial resolution of 25 m by proposing a novel approach designed for mountainous catchments. In detail, we exploit i) daily HR time-series of snow cover area (SCA) obtained by high- and low-resolution optical images to define the days of snow presence (derived in the framework of this thesis, as explained previously), ii) a degree-day model driven by in-situ temperature to determine the potential melting, iii) in-situ snow depth to derive the presence of a snowfall, and iv) SAR images to determine the occurrence of melting (derived in the framework of this thesis, as explained previously). The product derived in the framework of this PhD thesis allows to sample more adequately than standard products the snow distribution, resulting in a highly detailed spatialized information that represents an important novelty. The proposed SWE reconstruction approach also foresees a novel SCA time-series regularization from impossible transitions, i.e. the change of the pixel class from snow to snow-free when it is supposed to be subjected to an accumulation event or, the other way round, the change from snow-free to snow during a melting event. Moreover, it reconstructs SWE for the whole hydrological season, i.e., both accumulation and melting phase, without the need of spatialized precipitation information as input, which is usually affected by uncertainty. Despite the simple approach based on a set of empirical assumptions, it shows good performances when tested in two different catchments: the South Fork catchment, California, and the Schnals catchment, Italy. The results show a good agreement with an average bias of -40 mm when evaluated against a HR spatialized reference product and of 38 mm when evaluated against manual measurements. Such a high detail product is of great interest for several hydrological and ecological applications.

Thesis Organization

The thesis is organized in five main chapters. Chapter 1 illustrates the fundamentals and the background notions useful for understanding the dissertation. Chapter 2 presents the proposed approach to the evaluation of the snowmelt dynamics in alpine regions by using Sentinel-1 SAR observations. Chapter 3 describes the novel approach based on a hierarchical multi-resolution analysis of optical time series to reconstruct the daily high-resolution snow cover area. Chapter 4 presents the novel use of multi-source high-resolution satellite data for SWE reconstruction over mountainous catchments. Finally, in the last chapter the conclusions of the thesis are drawn and proposals for future research developments are discussed.

Chapter 1

Fundamentals and Background

In this chapter we present the fundamentals of snow physics, a brief overview of the in-situ techniques to measure the most relevant snow parameters and an introduction to remote sensing of snow techniques. This provides the basic concepts and basics that are needed in the next chapters of the thesis and introduces the main parameters that are of interest for this work.

1.1 Physics of Snow

Snow is a porous, multiphase medium made up by ice, air and water. The ice crystals form a solid continuous structure that is connected through the pores. The three phases usually coexist having the snowpack a temperature that is nearby the melting point. However, their fractions continuously vary due to the exposure to external forcings (temperature, solar radiations, precipitation, wind, gravity, etc.). This results in internal changes that lead to the melting of the ice structure and the percolation of the water fraction within the pores due to gravity. The continuous transformation of the snowpack microstructure is known as snow metamorphism and leads to the formation of clear distinguishable layers (Fierz et al. 2009). Due to its unique characteristics, the snow represents an energy bank that stores and releases energy as well as an insulator and reservoir of water, thus representing an ideal ecosystem for many organisms.

The snowpack is characterized by the snow height (HS). However, most important property is the snow water equivalent (SWE). SWE represents the height of the water stored in the snowpack and that would be released upon complete melting of the snowpack. Hence, we need to count both for the free water and the water stored as ice matrix. SWE is usually expressed in [mm] and it is define as follows:

$$\text{SWE} = \frac{V_w + \frac{\rho_i}{\rho_w} V_i}{A} \quad (1.1)$$

where V_x is the volume of the x-phase (w : water, i : ice, and a : air), ρ_x the density of each phase and A is the base area of the considered volume. However, it is impossible to measure V_w and V_i and consequently SWE is determined by estimating

the vertically-integrated density of the snowpack ρ_{snow} :

$$\text{SWE} = \text{HS} \cdot \frac{\rho_{snow}}{\rho_w} \quad (1.2)$$

Generally, each volume component is normalized w.r.t. to the total volume of the snowpack by defining the three volumetric fractions:

- $\theta_i := \frac{V_i}{V_i+V_w+V_a}$ the ice fraction;
- $\theta_w := \frac{V_w}{V_i+V_w+V_a}$ the water fraction;
- $\theta_a := \frac{V_a}{V_i+V_w+V_a}$ the air fraction.

Of course, it is always valid:

$$\theta_i + \theta_w + \theta_a = 1 \quad (1.3)$$

θ_w is also known as liquid water content (LWC). The presence of water inside snow is very important and alters for example its electromagnetic properties. When no water is present inside snow - as it usually happens when snow accumulates - we refer to *dry snow*; on the other hand, we refer to *wet snow* when $\theta_w > 0$.

A quick insight into the equations that describe the snowpack and are used in the physically based snow models is given (e.g., Bartelt & Lehning 2002, Vionnet et al. 2020, Endrizzi et al. 2014, Strasser et al. 2011). They are derived from the mass and the energy conservation. By applying the mass conservation, neglecting the air mass, and dividing by ρ_w , it is possible to obtain the following:

$$\frac{\partial \theta_w}{\partial t} + \frac{\rho_i}{\rho_w} \frac{\partial \theta_i}{\partial t} + \vec{\nabla} \cdot \vec{J}_w + S_w = 0 \quad (1.4)$$

where the first two terms represent the variation in time of the liquid and ice component, respectively, the third term represents the water flux (by neglecting the ice flux) and the last term represents the phase change sink or source term arising from evaporation or sublimation. Moreover, it is possible to impose the following boundary condition:

$$\frac{\partial M_*}{\partial t} = P - E_v - G_p \quad (1.5)$$

that expresses the variation in terms of snow mass ($M_* := M_w + M_i + M_a$) as balance between the different contributes that arise from the precipitation P , the sublimation E_v and the percolation G_p .

From the energy balance, we can instead derive the following equation:

$$\frac{dU_*}{dt} = R_{nlw} + R_{nsw} - H - \lambda_s E_v + G + P_e \quad (1.6)$$

where the variation of internal energy U_* is expressed as contribution of the net longwave radiation R_{nlw} , the net shortwave radiation R_{nsw} , the sensible heat flux H , the latent heat flux $\lambda_s E_v$, the ground heat flux G and the energy arising from

the precipitation P_e .

A correct understanding of the snowpack implies a correct characterization of the phases that lead to its formation and evolution. First of all, snow accumulation that is linked to the geomorphology of the study area but is still challenging to predict. At a large scale snowfalls are mainly controlled by the weather dynamics and consequently by the geographic area, elevation and aspect. At a smaller scale local effects as wind or gravitational distribution that are linked to the micro-topography and canopy presence strongly influence the spatial snow distribution (Seibert et al. 2021). Due to this strong variability, the phenomenon needs to be monitored at the appropriate spatial scale. Nevertheless, it is possible to recognize seasonal SWE spatial patterns that are associated with elevation, slope, aspect and vegetation (Mendoza et al. 2020). Once snow is accumulated on the ground, it is subjected to redistribution due to wind or gravity, sublimation and ablation. In this thesis, we focus on the snowmelt processes that are strongly related to the energy inputs. It is during the melting phase that we can notice the major variations of SWE and LWC. An accurate estimation of these parameters is thus essential for characterizing the snowpack. Moreover, the release of liquid water during the melting phase is of interest for most of the applications, as flood predictions or hydropower management. However, being that melting is a nonlinear process affected by the strong variability of both the snowpack characteristics and the meteorological forcings, it is challenging both to measure or to predict the variables of interest. The melting phase starts when the wetting front penetrates through the snowpack due to the energy exchanges that happen at the surface of snow, as increasing air temperature, solar radiation or rain on snow. This results in an increase of LWC. The snowpack becomes isothermal and when no more liquid water can be retained, the runoff phase starts, thus resulting in a strong decrease of SWE.

Further information about the snowpack properties will be given in Chapter 2, where we will discuss in more detail the evolution of LWC within the snowpack during the hydrological season and how this is detectable by the satellite. In chapter 4, we will propose an attempt to reconstruct SWE by mean of RS data and other auxiliary information. However, in the next Section we want to give a quick overview of the existing methods to determine these variables through in-situ manual or automatic observations.

1.2 Ground Observations

Traditional snow profiles consist in a snow pit that is dug to the ground level. The observer identifies the stratigraphy, i.e. the different layers, and characterizes the snowpack by performing different kind of qualitative and quantitative measurements, e.g., temperature, snow density, grains size and form, permittivity. Manual snow depth measurements are collected during field campaigns simply by mean of one or more snow stakes that are inserted in the snowpack. The measurements can be collected in several points, for example along a transect, in order to identify

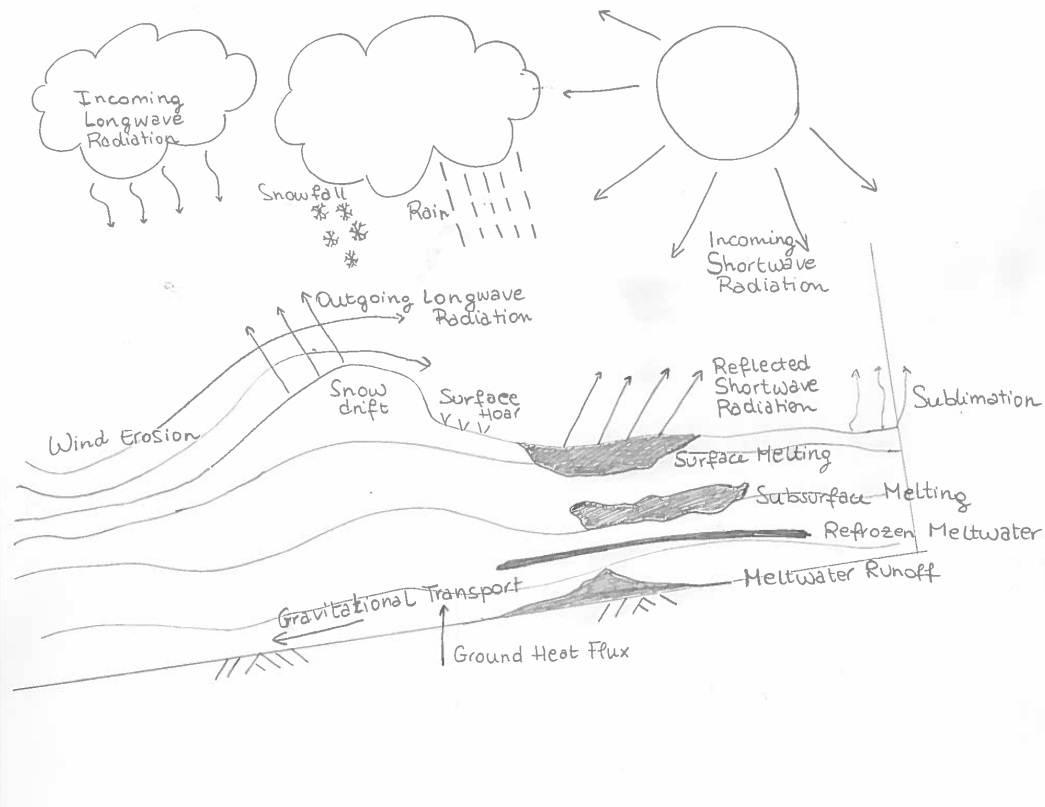


Figure 1.1: Principal physical processes that affect snow. Image inspired by SLF (see <https://www.wsl.ch/en/services-et-produits/logiciels-sites-inter-nets-et-apps/snowpack.html>)

the spatial heterogeneity of the investigated area. In fact, topographically complex environments, such as the European Alps, present a snowpack with high spatial variability. SWE manual measurements consist in weighing samples of each layer of a snow profile in order to estimate an averaged snowpack density ρ_{snow} that can be used in Eq. 4.6. A faster alternative is represented by SWE coring samplers that are long tubes (up to 2 m) that allow to core the snow and weight the entire column. Another alternative method is to take advantage of changing dielectric properties of snow to measure density and LWC by mean of the so-called Denoth probe (Denoth 1989).

Automatic meteorological stations managed by local authorities or private bodies are also available throughout the territory. The measurement is usually carried out thanks to an ultrasonic sensor that measures the time needed by a pulse to travel from and back to a target. This instrument represents a low-cost and widespread method to measure snow depth and it is usually coupled with other automatic sensors that measure other weather variables, such as air temperature, wind speed and direction, and incoming/outgoing radiation. However they are representative of a very restricted spatial area. Well-equipped networks also provide continuous SWE measurements. The most common instruments are represented by the snow scale



Figure 1.2: Example of a traditional snow pit analysis.

or the snow pillow. The first measures the weight of snow that accumulates on the scale and converts it into SWE. The second measures the hydrostatic pressure of snow that accumulates on the pillow on a bladder filled with anti-freeze and water. Innovative, low-cost and non-invasive methods to derive SWE are also based on Global Positioning System (GPS) signals Koch et al. (2019) or on Cosmic-ray neutron sensing (CRNS) Schattan et al. (2019). Both methods measure the attenuation of a signal that comes from different sources - in the first case, the GPS L-band signal and in the second case, the cosmic-ray induced neutron flux.

1.3 Remote Sensing of Snow

Satellite remote sensing represents a valid tool to monitor snow given its applicability over large and remote areas. On one hand, optical multi-spectral sensors that operates within the wavelengths of the visible (VIS), near (NIR) and shortwave infrared (SWIR), are able to detect the presence of snow. In fact, due to its high albedo, snow reflects up to 90% of the radiation in the VIS wavelengths ($0.4\text{-}0.8\mu\text{m}$). The reflectance of snow decreases for longer wavelengths (NIR) and it is approximately 0 for the SWIR region. This results in the typical spectral signature of snow that can be easily distinguished from other surfaces (see Fig. 1.3). These properties allow to easily distinguish snow from other land surfaces by mean of optical multi-spectral sensors that operate in the aforementioned regions of the electromagnetic spectrum. For example, the normalized difference snow index (NDSI) is established as follows:

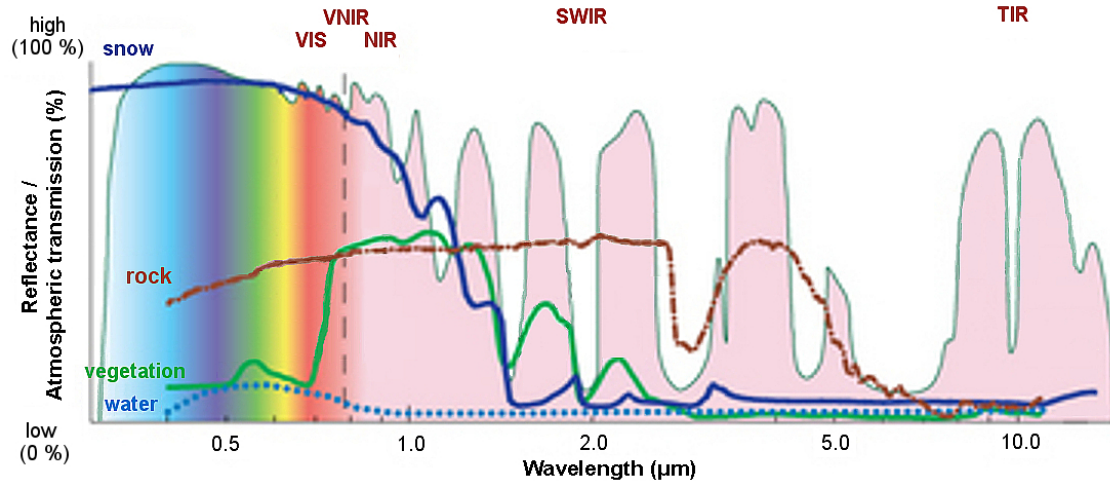


Figure 1.3: Reflectances of different surfaces. Credit: Andreas Kaab, University of Oslo.

$$NDSI = \frac{VIS - SWIR}{VIS + SWIR} \quad (1.7)$$

The NDSI is used as threshold for the snow classification in many state-of-the-art methods (e.g., Crane & Anderson 1984, Dozier 1989, Lopez et al. 2008, Klein et al. 1998). Furthermore, by performing a regression on the NDSI it is also possible to retrieve information about the snow cover fraction (SCF), i.e. the percentage of snow within a pixel Salomonson & Appel (2006). The SCF can be retrieved also by mean of methods based on the spectral unmixing, i.e., the spectral signature of a pixel is derived as combination of reference spectral signatures and in this way it is possible to determine the abundance of each reference surface Painter et al. (1998), Bair et al. (2021). More advanced methods exploit all the available spectral information combined eventually with other features (e.g., digital elevation model (DEM) derived features) by mean of machine learning (ML) techniques, such as neural networks, support vector machine (SVM) up to more complex deep learning (DL) architectures (e.g., Dobрева & Klein 2011, Nijhawan et al. 2019). Methods based on NDSI or multi-spectral unmixing are often used for operational snow detection being easy to implement, with the main disadvantage that may lack in robustness especially in challenging situations. For example, problems arise when we face with conditions as mixed pixels that are not completely covered by snow, snow under canopy, presence of semi-transparent clouds or cirrus, or scarce illumination conditions as in shadowed areas that result in difficulties in detecting snow.

Another important limitation of optical sensors is represented by cloud obstruction that reduces considerably the number of available scenes. Moreover, optical sensors are useful to identify the presence/absence of snow but do not provide an information about the mass of snow on the ground. However, the temporal persistence of snow on a pixel is a very important indicator that is linked to the SWE stored in the snowpack (e.g., Cline et al. 1998, Molotch & Margulis 2008, Margulis et al. 2006). This parameter can be integrated with other sources of information, such as hydrological models or other RS tools that provide knowledge on the snowpack mass.

In this context, sensors that operate in the microwave portion of the electromagnetic spectrum can be used to provide some important information about the snow mass. In detail, SWE information may be extracted by mean of passive microwave sensors (Pulliainen et al. 2020). This is possible by exploiting the correlation between the brightness temperature and SWE. However, these data are limited by a poor spatial resolution, i.e., 25 km. Active microwave sensors such as Synthetic Aperture Radars (SAR) represent also an important tool for SWE retrieval (Shi et al. 1994, Baghdadi et al. 1997, Ulaby et al. 1981, Rott et al. 2010) and differential SWE (Gunteriusen et al. 2001, Leinss et al. 2015). Since the presence of liquid water within the snowpack alters its electromagnetic properties causing dielectric losses, these sensors are able to detect important information about the snowmelt. For example, dry snow is almost transparent for SAR sensor at C-band meanwhile the presence of water in the snowpack causes dielectric losses Baghdadi et al. (1997). However, also these sensors present some limitations especially due to the intrinsic difficulty in the signal interpretation that is affected by a multitude of non-linear effects due for example to surface roughness, snow density, grain type and size which in turn are affected by the complex snow metamorphism. Moreover, all these techniques work only in dry conditions while the scarce penetration of the electromagnetic signal in wet conditions is invalidating their applicability in monitoring the SWE evolution during the melting season. Several review articles are available for more details about SWE retrieval using SAR acquisitions (e.g., Tsang et al. 2021).

Another limitation that affect both active and passive sensors is represented by the trade-off between spatial and temporal resolution, as illustrated in Fig. 1. In fact, due to limitations in current satellite technologies linked to the swath angle, it is possible either to provide daily or sub-daily data with poor spatial resolution (e.g., hundreds of km) or high spatial detail (e.g., tens of m or even less) with low resampling time. However, a proper characterization of the snow properties requires a high spatial and temporal detail. In fact, the spatial heterogeneity of the snow accumulation/redistribution is very strong and it is linked to weather phenomena as well as geomorphological properties of the study area. The detail of tens of m can even be not representative of this variability, but it represents an important improvement in the monitoring of the snow cover area and can introduce relevant benefits when assimilating this information in hydrological models (Li, Lettenmaier, Margulis & Andreadis 2019). Furthermore, at least a daily (or even sub-daily) detail is desired to represent quick changes in the snow cover area.

Chapter 2

Use of Sentinel-1 Radar Observations to Evaluate Snowmelt Dynamics in Alpine Regions

Knowing the timing and the evolution of the snow melting process is very important, since it allows the prediction of: i) the snow melt onset; ii) the snow gliding and wet-snow avalanches; iii) the release of snow contaminants and iv) the runoff onset. The snowmelt can be monitored by jointly measuring snowpack parameters such as the snow water equivalent (SWE) or the amount of free liquid water content (LWC). However, continuous measurements of SWE and LWC are rare and difficult to obtain. On the other hand, active microwave sensors such as the Synthetic Aperture Radar (SAR) mounted on board of satellites, are highly sensitive to LWC of the snowpack and can provide spatially distributed information with a high resolution. Moreover, with the introduction of Sentinel-1, SAR images are regularly acquired every 6 days over several places in the world. In this chapter¹, we analyze the correlation between the multi-temporal SAR backscattering and the snowmelt dynamics. We compared Sentinel-1 backscattering with snow properties derived from in situ observations and process-based snow modeling simulations for five alpine test sites in Italy, Germany and Switzerland considering two hydrological years. We found that the multi-temporal SAR measurements allow the identification of the three melting phases that characterize the melting process i.e., moistening, ripening and runoff. In detail, we found that the C-band SAR backscattering decreases as soon as the snow starts containing liquid water, and that the backscattering increases as soon as SWE starts decreasing, which corresponds to the release of meltwater from the snowpack. We discuss the possible reasons of this increase, which are not directly correlated to the SWE decrease, but to the different snow conditions, which change the backscattering mechanisms. Finally, we show a spatially-distributed application

¹This chapter has been published in:

Marin, C., Bertoldi, G., Premier, V., Callegari, M., Brida, C., Hürkamp, K., Tschiersch, J., Zebisch, M., Notarnicola, C. (2020), 'Use of sentinel-1 radar observations to evaluate snowmelt dynamics in alpine regions', *The Cryosphere* **14**(3), 935–956.

of the identification of the runoff onset from SAR images for a mountain catchment, i.e., the Zugspitze catchment in Germany. Results allow to better understand the spatial and temporal evolution of melting dynamics in mountain regions. The presented investigation could have relevant applications for monitoring and predicting the snowmelt progress over large regions.

2.1 Introduction

Seasonal snowpack is one of the most important water resources present in nature. It stores water during the winter and releases it in spring during the melting. In mountain regions, snow storage is essential for the freshwater supply of the lowlands, making the mountains the water towers of the downstream regions Viviroli & Weingartner (2004). In fact, the temporally delayed release of the water from the head-watersheds to the forelands is essential for a large number of human activities such as agriculture irrigation, drinking water supply and hydropower production (Beniston et al. 2018). In particular, in the Alps, discharges in May and June are largely dictated by snowmelt, while from July to September are influenced by glacier melt (Wehren et al. 2010) and liquid precipitation. On the other hand, wet snow may contribute to natural disasters such as wet snow avalanches (Bellaire et al. 2017) or wet-snow gliding (Fromm et al. 2018). Moreover, in case of accumulated contaminant release from a snowpack, initial runoff meltwater can be highly enriched and is able to cause severe impact on the water quality (Hürkamp et al. 2017). In this context, knowing the temporal and spatial evolution of the snow melting process is very important for a proactive management of the water resources and for hazard mitigation.

The melt period can be generally separated in three phases (Dingman 2015): i) moistening, ii) ripening and iii) runoff. The moistening is the initial phase of the snowmelt. The air temperature and solar radiation increase and due to heat exchanges and/or rain the superficial layers of the snowpack start melting. The ripening phase begins when the maximum retention capacity of the pores is exceeded. The wetting front penetrates through the snowpack, driven by repeated cycles of melting and refreezing, but the meltwater is not yet released. During this phase, the snowpack becomes isothermal and when no more liquid water can be retained, the runoff phase starts. The snowmelt process is a non-linear process affected by the strong variability of both the snowpack characteristics and the meteorological forcings that affect the snow. In order to obtain useful information about the progression of the melting process, non-invasive techniques that allow performing multiple measurements at the same location should be exploited. For this purpose, measurements of meteorological variables such as air temperature, snow temperature, relative humidity, wind speed, precipitation, and solar radiation are usually employed to extract information on snow melt dynamics (Kinar & Pomeroy 2015). However, the most significant state variables to properly identify the three melting phases are the snow water equivalent (SWE), i.e. the total mass of liquid and solid water stored in form of snow, and the liquid water content (LWC), i.e. the mass of liquid water inside the snowpack. An increase of LWC in time indicates a moistening process going on. The downward penetration of the water front into the snowpack

brings first, to a partial, and later to a complete isothermal state. This leads to the generation of water runoff, and consequently to a significant decrease of SWE. It is worth mentioning that sublimation may also contribute to SWE decrease (Strasser et al. 2008).

Continuous measurements of SWE and LWC is therefore essential to monitor the snowpack melting dynamics. So far, the most common method to manually measure SWE is using snow sampling tubes, while the most spread techniques for automatic SWE measurement include snow pillows and snow scales (Kinar & Pomeroy 2015). The installation and the maintenance of these kinds of measurements are very costly and a relatively limited number of continuous measurements of SWE are available in the Alps. Direct measurements of LWC are usually performed through empirical estimations (e.g. the hand test), or indirect assessments based on snow temperature. Recently, some promising systems that exploit the dielectric properties of the snow in the microwave region of the electromagnetic (EM) spectrum have been presented to allow a continuous and nondestructive measuring of LWC. In particular, three systems have demonstrated to be effective and robust in operational conditions: i) the snowpack analyzer (SPA) (Stähli et al. 2004); ii) the snow sense (Koch et al. 2014) based on GPS signals; and iii) the upward-looking Ground Penetrating Radar (upGPR) (Schmid et al. 2014). All of them are commercial systems buried under the snowpack and rely on different methods for the dielectric constant estimation. Interestingly, these EM devices can be used to measure the SWE as well. However, all these ground-based measurements are limited in application to a single point, require calibration to relate the dielectric constant to volumetric snow LWC, and some of them are expensive, power intensive and laborious to be installed and maintained. These limitations complicate the possibility to monitor and understand the meltwater runoff and the snow stability considering also the spatial variability of the snowmelt dynamics.

To mitigate these limitations, energy based, multilayer physically based snow models can simulate SWE and LWC at high spatial and temporal resolution (Essery et al. 2013). Such kind of models account for shading, shortwave and longwave radiation, and turbulent fluxes of sensible and latent heat (Mott et al. 2011), but can differ in the way they parametrize snow metamorphism, grain size evolution, snow layering and liquid water percolation (Wever et al. 2014). They can range from very detailed approaches with a Lagrangian representation of snow layers as avalanche-forecasting models like CROCUS (Brun et al. 1992) or SNOWPACK/ALPINE3D (Bartelt & Lehning 2002, Lehning et al. 2006) to more simplified approaches as the ones of hydrologically-oriented Eulerian models as AMUNDSEN (Strasser et al. 2011) or GEOtop (Endrizzi et al. 2014). Therefore, snow models can provide detailed information about the snow properties starting from observed meteorological conditions, which can be reliably acquired especially at plot-scale. However, model performances are affected by uncertainties and errors related to model structure (Avanzi et al. 2016), meteorological forcing (Raleigh et al. 2015) and model parametrizations (Engel et al. 2017, Günther et al. 2019). Therefore, there is the need of snow observations with high temporal and spatial resolution, distributed over a large area and systematically acquired.

In the past years, Synthetic Aperture Radar (SAR) was shown to be a valid tool

to identify the wet snow i.e., snow that contains a given amount of free liquid water (Nagler & Rott 2000, Dong 2018). In fact, SAR measurements are highly sensitive to the liquid water in the snowpack and the increase of the LWC causes a high dielectric loss that increases the absorption coefficient generating backscattered signal with low intensity (Ulaby et al. 2015). This physical principle has been exploited for the generation of wet snow maps by the bi-temporal algorithm proposed by (Nagler & Rott 2000) and further improved in (Nagler et al. 2016). However, the increase of the liquid water content explains only partially the decrease of the backscattering coefficient. Indeed, as pointed out in Shi & Dozier (1995) and Baghdadi et al. (2000), the relationship between the coefficient of backscattering and the snow wetness can cause an increment of the backscattering value depending on the conditions of the snow roughness, snow density, snow layering, snow grain size and local incidence angle. This large number of unknowns, upon which the SAR backscattering is dependent on, defines a complex multiparametric problem that is difficult or even impossible to solve without introducing some simplification assumptions. So, even though some works have been presented that try to extract the LWC using C-band SAR images (Shi & Dozier 1995, Longepe et al. 2009), at the best of our knowledge there are no attempts to use the SAR as source of information for describing the multi-temporal evolution of the snow melting process. Progress has been hampered by: i) the lack of ground truth information; ii) the relative high number of sources of uncertainty of the SAR signal; and iii) the difficulty to access SAR data in the past. This has changed since 2014 with the introduction of the Sentinel-1 (S1) mission from the European Space Agency (ESA) and the European Commission (EC) guarantying the availability of C-band SAR images free of charge. In detail, S1 is a constellation made up of two near-polar sun-synchronous satellites that acquire images early in the morning and late in the afternoon, with a revisit time of 6 days at the equator. Moreover, as discussed before, an increasing number of data on relevant snow parameters related to the snowmelt are collected by operational systems (e.g. by SPA) or derived by physically based snow models. The information on SWE and LWC provided by independent sources opens new opportunities for better understanding the relationship between the snowpack properties during the melting phase and the multi-temporal SAR backscattering.

The aim of this work is to evaluate the information that S1 can provide on monitoring the snowmelt dynamics. In particular, we provide the theoretical EM background for understanding the impact on the multi-temporal SAR backscattering of a melting snowpack. Then, we analyze the relationship between the multi-temporal SAR signal acquired from S1 and in situ measurements of LWC and SWE in the Alps. Given the limited number of point-related continuous SWE and LWC measurements available in the test area, we made use of the physically based model SNOWPACK to simulate the snow properties in other locations where only meteorological data and snow depth were available. This allowed us to define five test sites at different altitudes in the Alps, where the interactions of S1 backscattering with the snowpack were studied in detail during two melting seasons. On the basis of the outcomes of the study, we propose an interpretation scheme to be applied to multi-temporal dual polarization C-band SAR data in order to identify the different snow melting phases of moistening, ripening and runoff. Finally, we demonstrate

the effectiveness of the proposed approach in a real application scenario to provide a spatially distributed information about the melting phases of the snowpack in alpine terrain, which can be used for monitoring and predicting the snowmelt progress over large regions.

2.2 Background

In this section we report the theoretical background on which this work is based on. First, the snow melting process is explained from a physical point of view and the different phases are identified considering the information of LWC and SWE. Then, the response of the SAR backscattering to the wet snow is described in detail.

2.2.1 Snow melting process

Fig. 2.1 illustrates the snow cover development during the melting season considering the snow status in the morning and in the afternoon, when the S1 descending and ascending data is acquired respectively. Hypothetical values of LWC and SWE are reported on the right side of the figure. In general, the liquid water is introduced in the snow by rain and/or melt due to heat exchange and the incoming flux of shortwave radiation flux, which varies with slope, aspect and elevation. In both cases, the snowpack starts melting at the surface (Techel & Pielmeier 2011). This superficial moistening phase can be identified by comparing observations from the coldest and warmest period of the day i.e., a diurnal cycle is visible. Interestingly, the SAR acquisitions are approximately acquired around these two periods. The liquid water released or absorbed from the superficial layers gets in contact with the subfreezing snow present underneath and freezes. This releases latent heat that causes the snowpack to warm up starting the process of snow ripening. Repeated cycles of partial melting during the day and refreezing during the night induce the development of the wetting front into the snow. This is generally not uniform, since infiltrations usually start through isolated “flow fingers” which enlarge into meltwater channels due to the passing of time. Therefore, the ripening of the snowpack may be different year by year or considering different areas. In fact, climatic factors or snowpack stratifications may induce different behaviors. At the point of full water saturation, the snow layer cannot retain any more liquid water. Further absorption of energy produces water output, which, depending on soil properties, ice and water content, could infiltrate in the soil or appear as surface runoff (DeWalle & Rango 2008*a*). The runoff phase is characterized by a significant decrease of SWE.

During the melting, the presence of liquid water inside the snowpack directly affects the grain size, the grain shape and the density of the pack (Pomeroy & Brun 2001). Indeed, during the melt process the snow undergoes to a rapid metamorphism that leads to a growing and a rounding of the grains linked to an increase of the snow density. Moreover, it is important to underline that during the melt season a general increase of the roughness of the snow surface is observed (Fassnacht et al. 2009) due to localized melting pattern (i.e., flow fingers) and rain on snow events.

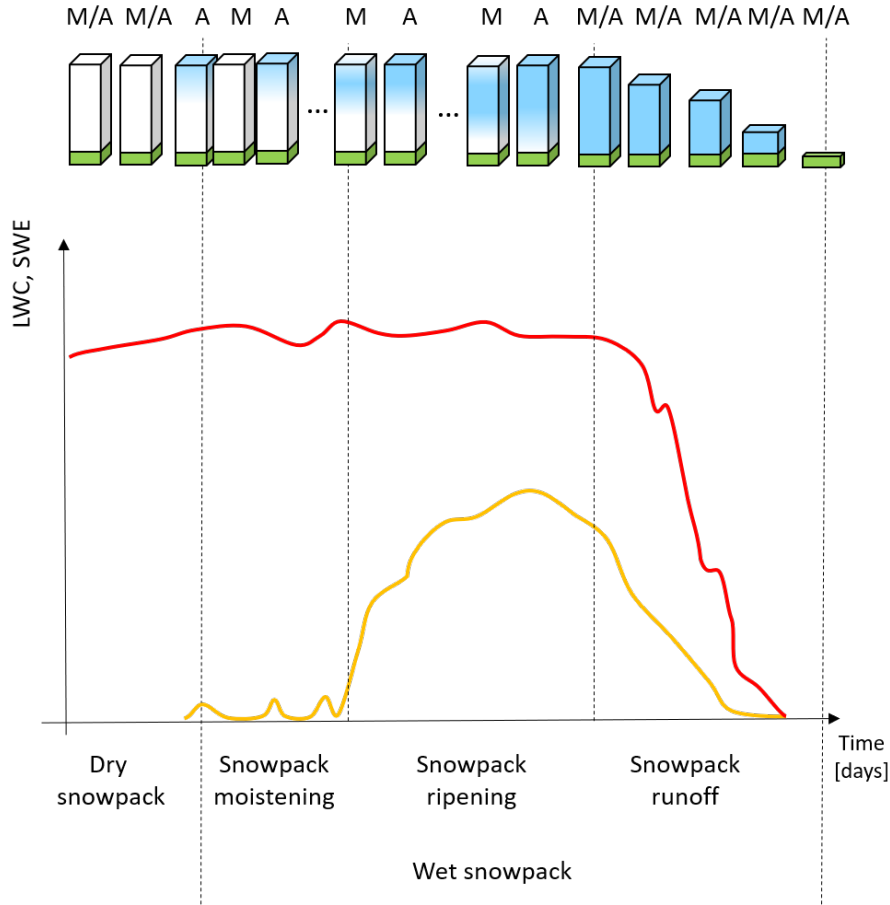


Figure 2.1: Example of transitions in snow status during the melting season obtained by sampling the snow in the morning (M), when the S1 descending observations are taken, and in the evening (A) when the S1 ascending data are taken. The upper part of the figure illustrates the simplified temporal transportation of the free liquid water (blue area) in the dry snowpack (white area). The lower part of the figure illustrates the respective temporal evolution of LWC (yellow line) and SWE (red line). In detail, by starting from a dry situation, the liquid water is introduced into the snowpack by either a rain event or the melt due to the incoming flux of shortwave radiation. In this moistening phase the LWC (yellow line) varies with a diurnal cycle. Repeated cycles of partial melting and refreezing lead the snowpack to the isothermal state. During the ripening period, a combination of different situations can occur depending on the weather conditions but an increasing trend of the LWC is visible. Once the snowpack is isothermal and it cannot retain water anymore, it starts to produce water output until it melts totally. This last phase starts with a significant decrease of the SWE (red line).

2.2.2 SAR backscattering response to wet snow

From an EM point of view, the snowpack is an inhomogeneous medium composed of scattering elements with different sizes, shapes, orientations and permittivity values. The backscattering σ^0 produced by an EM wave generated by SAR over such a medium can be modeled as an incoherent sum of three contributions (Shi & Dozier 1995, Ulaby et al. 2015): the surface scattering produced at the air-snow interface, σ_{sup}^0 , the surface scattering produced at the snow-ground interface attenuated by the snowpack, σ_{grd}^0 , and the volumetric scattering of the snowpack, σ_{vol}^0 . The intensity of these contributions depends on parameters related to: i) the sensors i.e., frequency, local incidence angle (LIA) and polarization; ii) the snowpack properties i.e., liquid water content (LWC), density (DS), ice particle size and shape (GS), surface roughness (SR), which is usually described by the standard deviation of the height and the correlation length of the surface; and iii) the ground properties. In this chapter, we focus on the use of the C-band SAR mounted on board of S1, and therefore all the parameters related to the sensor are known. Nonetheless, deriving the theoretical behavior of the time series of σ^0 for a given LIA for one hydrological year is complex. Indeed, the relationship between the backscattering and the snow parameters forms a non-linear system of equations. In the following we identify the main scattering mechanisms isolating the contribution of each parameter to the total backscattering.

During the accumulation period, dry snow is almost transparent for C-band, and the radar echo can penetrate the snow for several meters. In this situation, the main scattering source is the snow-ground interface (see Fig. 2.2) and the backscattering is almost insensitive to different snow parameters (Rott & Mätzler 1987, Shi & Dozier 1993). During the melting period, the increase of the free liquid water inside the snowpack causes high dielectric losses, which increase the absorption coefficient. By considering a sufficiently thick snowpack, this leads to a rapid decrease of σ_{grd}^0 , which can be then neglected. By assuming constant all the parameters but the LWC, the increase of LWC causes the volume scattering to decrease and the backscattering becomes sensitive to surface roughness (Shi & Dozier 1995). When the surface is smooth e.g., according to the Fraunhofer criterion (Ulaby et al. 2015), volume scattering dominates and therefore the increase of LWC results in a decrease of the total backscattering. Whereas, when the surface is rough the surface scattering dominates, thus with the increase of LWC the total backscattering tends to increase. The amount of wetness from which the surface scattering becomes predominant depends mainly on the surface roughness and LIA and may vary from about 1% to 6% of the total volume (Magagi & Bernier 2003). However, other parameters play a role in this mechanism: by assuming constant all the parameters but the snow density, the volume scattering decreases at the increase of the snow density, if all the other parameters are kept fixed. Vice versa, the grain size increases the volume scattering. It is finally worth stressing the fact that the response to the wet snow becomes more complex in case of the snowpack in forest (Koskinen et al. 2009). In this case the total backscattering σ^0 is a function also of the forest stem volume. This can be estimated and taken into account, nonetheless in this work we focus on the identification of snow melting phase in open areas.

The main scattering mechanisms and their influence on the backscattering, as

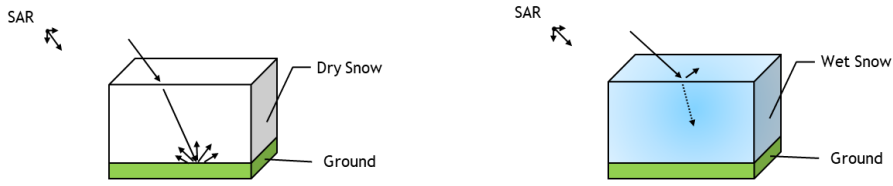


Figure 2.2: Main SAR backscattering mechanisms in presence of dry and wet snow at C-band. The dry snow is almost transparent, and the radar echo can penetrate the snow for several meters. The presence of LWC, causes high dielectric loss, which increases the absorption coefficient.

Table 2.1: Simplified SAR backscattering response to wet snow divided in volumetric, σ_{vol}^0 , and surface backscattering, σ_{sup}^0 , contributions. Considering a sufficiently thick snowpack the contribution of σ_{grd}^0 can be neglected.

Parameter	σ_{vol}^0	σ_{sup}^0
Liquid water content (LWC)	negative correlation	positive correlation
Snow density (DS)	negative correlation	positive correlation
Snow grain size (GS)	positive correlation	-
Surface roughness (SR)	-	positive correlation

studied in the literature, are reported in Table 2.1. Even though the table is reporting the main backscattering mechanisms of the different snow conditions during the melting process, the complete multi-temporal behavior that characterizes the three phases of moistening, ripening and runoff has not yet been studied. In particular, from an EM modeling point of view or real-data analysis, the implications of the wet-snow metamorphism i.e., increase of LWC, density, snow grain size and superficial roughness remain mainly unsolved. Indeed, state-of-the-art radiative transfer (RT) models, particularly designed for studying the snow melting process, such as Shi & Dozier (1995), Nagler & Rott (2000), Magagi & Bernier (2003), are not able to model the microstructure scattering interactions. Whereas, RT models that take into account the microstructure interactions, such as for example the modes developed in SMRT (Picard et al. 2018) or MEMLS3&a (Proksch et al. 2015) are not able to model the contribution from the superficial roughness and have never been specifically tested for the characterization of the melting phases. Therefore, without further research and validation activities, this invalidate the possibility to use state-of-the-art RT models to better understand the multi-temporal EM mechanisms during the snowmelt at C-band (e.g., Veyssi re et al. (2018) found a significant deviation between observations and simulations with MEMLS3&a during the melting period).

In the following, as first attempt to fill this gap, we will consider the real time series of backscattering recorded by S1 during two hydrological years in the proximity of five test sites where LWC and SWE were measured or simulated. The outcome of this study will be exploited to: i) understand if a characteristic relation can be recognized from the comparison between the multi-temporal SAR signal and the melting phases; and ii) define some rules to automatically identify the beginning of each melting phase from the time series of σ^0 .

Table 2.2: Details of the meteorological and snow parameters measured at each station. Wind velocity (VW), wind direction (DW), air temperature (TA), relative humidity (RH), snow depth (HS), snow temperature at depth x (TS_x), surface temperature (TSS), soil temperature (TSG), incoming shortwave radiation (ISWR), incoming longwave radiation (ILWR), outgoing shortwave radiation (OSWR), snow water equivalent (SWE), snow density (DS), liquid water content (LWC) and ice content (IC).

Station	Lat, Long	Altitude [m a.s.l.]	Available measurements
Zugspitze (Germany)	10.9835, 47.4064	2420	VW, DW, TA, RH, HS, TSS, ISWR, OSWR, SWE, DS, LWC, IC
Alpe del Tu- mulo (Italy)	11.1487, 46.9136	2230	VW, DW, TA, RH, HS, TS_x , TSS, TSG, ISWR
Clozner Loch (Italy)	11.0283, 46.5134	2165	VW, DW, TA, RH, HS, TS_x , TSS, TSG, ISWR
Malga Fadner (Italy)	11.8614, 46.9256	2155	VW, DW, TA, RH, HS, TS_x , TSS, TSG, ISWR
Weissfluhjoch (Switzerland)	9.8096, 46.8296	2455	VW, DW, TA, RH, HS, TSS, TSG, ISWR, OSWR, SWE

2.3 Dataset description

In this section, we present the experimental sites and we describe the collected in situ data, the SNOWPACK set up and S1 data.

2.3.1 Test sites description, and in situ data

For ground truth and as input for the simulations with SNOWPACK, we consider five snow and meteorological weather stations with different location in terms of place and altitude in the European Alps, equipped with different installed sensors. Among these, one is located in Bavaria (Germany), three in South Tyrol (Italy) and one in Graubünden (Switzerland). In detail, considered parameters are wind velocity (VW), wind direction (DW), air temperature (TA), relative humidity (RH), snow depth (HS), snow temperature at depth x (TS_x), surface temperature (TSS), soil temperature (TSG), incoming shortwave radiation (ISWR), incoming longwave radiation (ILWR), outgoing shortwave radiation (OSWR), snow water equivalent (SWE), snow density (DS), liquid water content (LWC) and ice content (IC). The considered data records started from the October 1, 2016 in order to cover the two winter seasons 2016/2017 and 2017/2018. An overview of the location of the stations is presented in Fig. 2.3 and a summary with the available parameters is presented in Table 2.2.

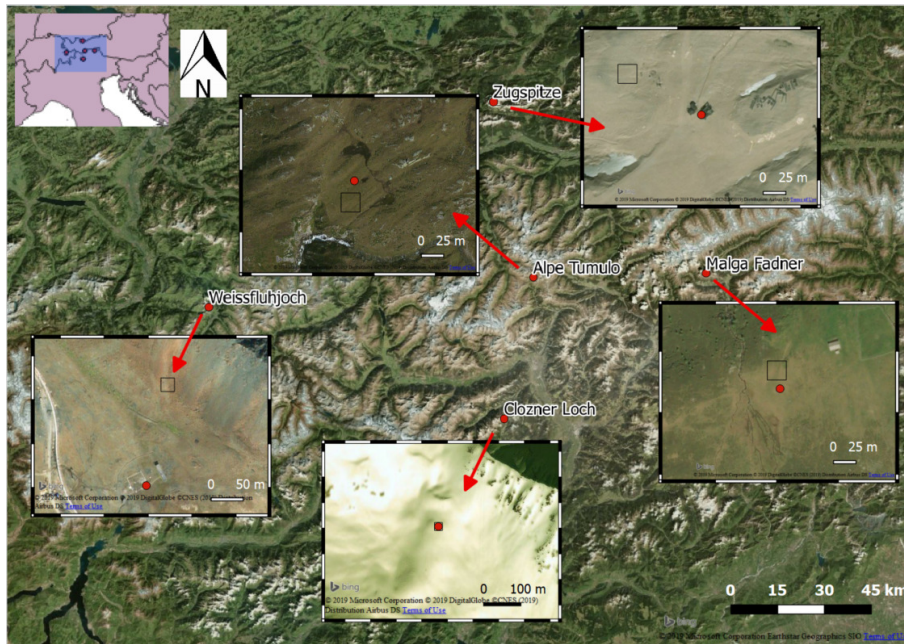


Figure 2.3: Overview map with the five stations located in Germany (Zugspitze), Switzerland (Weissfluhjoch) and Italy (Malga Fadner, Clozner Loch and Alpe Tumulò) used for the presented study (©2019 Microsoft Corporation ©2019 Digital Globe ©CNES(2019) Distribution Airbus DS). The red points indicate the exact location of the stations. The black squares indicate the S1 footprints. The footprints were selected in order to minimize any possible interference of the EM wave with the homemade structures but maintaining a certain correlation with the in situ measurements. The panoramic images give an idea about the land cover type and the topography around the stations.

Zugspitze (Werdenfelser Alps, Germany)

The station is located in the Northern Calcareous Werdenfelser Alps, being part of the Zugspitze massif. It is part of the snow monitoring stations network of the Bavarian Avalanche Warning Service (Lawinenwarnzentrale Bayern) and located on a flat plateau at the southern slope of Mt. Zugspitze summit (2962 m a.s.l.), the so-called Zugspitzplatt (1500-2700 m a.s.l.), which is surrounded by several summits in the north, south and west and drained by the Partnach River to the east. Beside a standard meteorological station, the site is additionally equipped with a snow scale and a snow pack analyzer (SPA) to record SWE, DS, LWC and IC. The SPA uses a time-domain reflectometry (TDR) at high frequencies and a low-frequency impedance analyzer. By exploiting different frequencies, the SPA is able to determine the volumetric ice, air and water content as well as the density by measurement of the complex impedance of the snow layer. The EM pulse propagates along three 5 m long sensor bands, horizontally installed in 10 cm, 30 cm and 50 cm above ground in 2016/2017. In 2017/2018 the heights of the bands were changed to 10 cm, 20 cm and 30 cm due to a frequent failure of the uppermost sensor in the preceding years. This allows the measurement of the bulk properties of the snowpack rather than a point measurement as well as a tracking of the downward penetrating water front inside the snowpack. Combined with information on the snow height bulk, LWC is determined. The SPA has not been calibrated for the test site, but it is used with standard set-up parameters and an internal calibration by the manufacturer. This results in unreliable LWC values of about 2-3 % when the snowpack is dry. Moreover, given that no bulk information of LWC for the total thickness of the snowpack is provided by the SPA, we did not use the SPA LWC in this study. Snow height is recorded by an ultrasound sensor, installed at 6 m height. The sensors for the meteorological parameters are installed at a crossbar of the 6 m mast, too, besides the wind sensor, which is at 6.5 m height. The maximum snow height was 3.3 m during winter 2016/2017 and 3.9 m in January 2018. The area is continuously covered by snow between December and May each year. During the accumulation period, the stations records showed that no significant snowmelt runoff at the snow base occurred at any time since 2012 (Hürkamp et al. 2019). During the observed winter seasons the mean monthly wind velocity exceeded 3 m s^{-1} in the winter months, therefore wind drift could likely alter snow accumulation. The amount of mean annual precipitation is 2000 mm.

Alpe del Tumulo (South Tyrol, Italy)

The station is located on an alpine pasture in the North of Val Passiria. For this and the other South Tyrolean stations, the temperature sensor is installed at a 2.8 m height and the wind sensor at 5.5 m. The site is weakly windy, with mean monthly velocity usually around 2 ms^{-1} . The maximum snow height was around 1.5 m during winter 2016/2017 and around 2 m during the winter 2017/2018. No continuous measurements of LWC and SWE are available for this and the other South Tyrolean stations.

Clozner Loch (South Tyrol, Italy)

The station is located in Lauregno (Alta Val di Non) on an almost flat site. The mean monthly wind velocity seldom exceeds 2 ms^{-1} . The snow height never exceeded 1 m during the winter 2016/2017 and the maximum height reached during the winter 2017/2018 was around 1.5 m.

Malga Fadner (South Tyrol, Italy)

The station is located on an alpine pasture in Valle Aurina. The mean monthly wind velocity never exceeds 2 m s^{-1} . The maximum snow height was less than 1.5 m during winter 2016/2017 and around 2 m during the winter 2017/2018.

Weissfluhjoch (Graubünden, Switzerland)

The automatic weather station is located at Weissfluhjoch, Davos, Switzerland. It is maintained by the WSL Institute for Snow and Avalanche Research SLF. The data are regularly updated and made freely available (WSL Institute for Snow and Avalanche Research SLF 2015). The wind sensor is installed at 5.5 m and the temperature sensor at 4.5 m. The site is quite windy, with mean monthly velocity usually around 2 ms^{-1} or sometimes greater than this value. The maximum snow height was around 2 m during winter 2016/2017 and around 3 m during the winter 2017/2018. In this study, SWE GPS-derived measurements are used (Koch et al. 2019), which are also freely made available upon request.

2.3.2 SNOWPACK model set up

As described in the introduction, the proper identification of the melting phases requires a precise knowledge of the evolution of LWC and SWE. However, these parameters are not always available for the selected test sites. For this reason, there is the need to set up snowpack simulations for obtaining the missing parameters. In this work we used the physically-based model SNOWPACK, a one-dimensional (1-D) model developed by the WSL Institute for Snow and Avalanche Research, SLF (Bartelt & Lehning 2002). The model solves 1-D partial differential equations governing the mass, energy and momentum conservation. Heat transfer, water transport, vapor diffusion and mechanical deformation of a phase changing snowpack are modeled assuming snow as a three-component (ice, water and air) porous material. Meteorological data are used as input for the model. Required parameters are air temperature, relative humidity, wind velocity, incoming longwave radiation and/or outgoing shortwave radiation, incoming longwave radiation and/or surface temperature, precipitation and/or snow depth and soil temperature. The data were taken or derived from the in situ measurements at the test sites. Meteo-IO (Bavay & Egger 2014) is used as pre-processing tool to check erroneous data, fill the gaps and generate missing parameters. In the current case, the ground temperature is generated as a constant value assumed to be equal to the melting temperature if missing, and the incoming longwave radiation is calculated through an all-sky parametrization, which makes use of air temperature and humidity (Unsworth & Monteith 1975, Dilly &

Table 2.3: SNOWPACK calibration results for each test site. Pearson correlation coefficient (ρ) and the mean absolute error (MAE) have been computed for snow depth (HS), snow temperatures at three different depth TS1 (0 m from the ground), TS2 (0.2 m from the ground), TS3 (0.5 m from the ground) and SWE, according to the availability of the ins situ data.

Station	Roughness [m]	Calibration results ρ [-]/MAE [$^{\circ}$ C]				
		HS	TS1	TS2	TS3	SWE
Zugspitze	0.005	0.99/3.7	-/-	-/-	-/-	0.99/47.8
Alpe Tumulo	0.03	0.99/3.6	0.90/0.4	0.93/0.4	0.88/0.5	-/-
Clozner Loch	0.01	0.99/4.1	0.87/0.8	0.78/1.8	-/-	-/-
Malga Fadner	0.01	0.99/2.8	0.83/0.6	0.83/0.7	0.85/1.2	-/-
Weissfluhjoch	0.002	0.99/2.8	-/-	-/-	-/-	0.99/35.1

O’Brien 1998). Fresh snowfall must be provided as initial condition. Since direct snow precipitation measurements are not available, the amount of new snow is forced by subtracting the model snow depth to the measured snow depth. This difference is assumed to be fresh snow only if reliable humidity and temperature conditions are verified, using the approach proposed and validated by (Mair et al. 2016) and implemented in the SNOWPACK model. This approach has been validated against snow pillow observations and resulted more reliable compared to heated tipping bucketed rain gauges, which may underestimate solid precipitation up to 40% (Sevruk et al. 2009). The energy exchanges on the snowpack surface are imposed either using a Neumann boundary condition (BC), i.e. the energy fluxes are forced, or a Dirichlet BC, i.e. imposing the surface temperature except during ablation when again a Neumann BC is imposed. Additionally, a Dirichlet BC is imposed at the ground interface. A neutral atmospheric surface layer using the Monin – Obukhov similarity theory is imposed. The used water transport model is the NIED scheme proposed by Hirashima et al. (2010). A typical time step of 15 minutes is used for the simulations.

Since the SNOWPACK simulations are used in this work as reference data to be compared against the SAR backscattering, we calibrated the model considering the best agreement in the analyzed years 2016-2018 with in situ snow depth, snow temperatures at three different depth TS1 (0 m from the ground), TS2 (0.2 m from the ground) and TS3 (0.5 m from the ground) and SWE, when available. Pearson correlation coefficient (ρ) and the mean absolute error (MAE) have been computed for these variables. The aerodynamic roughness length, i.e. a parameter for the Monin – Obukhov similarity theory that represents the height at which the wind speed becomes zero under neutral conditions, is used as calibration parameter. The roughness is strongly influenced by the topography and the geometric features of the study area, as for example the presence of canopy. Several tests have shown that SNOWPACK is mostly sensitive to variations of this parameter, that is why it has been chosen as unique calibration parameter. The results are reported in Table 2.3.

2.3.3 Remote sensing observations

S1 is a two satellites constellation with a revisit time of 6 days with the same acquisition geometry and able to acquire dual polarimetric C-band (central frequency of 5.405 GHz) SAR images with a nominal resolution of 2.7×22 m to 3.5×22 m in Interferometric Wide swath mode (IW). S1 works in a pre-programmed way in order to build a consistent long-term data archive of images all around the world. IW acquisitions have a swath of about 250 km. This, together with the cycle length of the satellites of 175 orbits, allows the acquisition of more tracks over a given location at the middle latitudes such as the Alps. Therefore, in 6 days more than one acquisition may be available for the area of interest. Table 2.4 indicates the most relevant parameters related to the data acquisition for each of the selected locations. For the five test sites a total of about 1300 acquisitions were considered. The data used for the presented study are Level-1 ground range detected data, consisting of focused SAR data that have been detected, multi-looked and projected to ground range using an earth ellipsoid model by the data provider. The resulting products have approximately square spatial spacing of 10 by 10 m. Phase information is lost for this data. This data can be downloaded free of charge from the Copernicus data hub (<https://scihub.copernicus.eu/>). In order to correct the complex topographic terrain, typical of mountain regions, and to reduce the speckle noise that affects SAR acquisitions, a tailored pre-processing has been applied for all the analyzed data. In detail, the pre-processing operations are performed using the tools included in SNAP (Sentinel Application Platform) version 6.0 and some custom tools developed in Python by the authors. In detail, the S1 backscatter pre-processing operations are the following (S indicates SNAP tool, C indicates custom tool): 1) application of the precise Sentinel orbit to the data (S); 2) removal of the thermal noise present in the images (S); 3) removal of the noise present at the border of the images (C); 4) beta nought calibration (S); 5) assembly of the S1-tiles coming from the same track (S); 6) co-registration of the multi-temporal images (S); 7) multi-temporal filtering with a window size 11x11 pixels (C); 8) gamma-MAP spatial filtering 3x3 pixels (S); 9) geo-coding and sigma nought calibration (S); 10) masking of the layover and shadow by considering the local incidence angle (LIA) for each pixel (C). It is worth noting that we use the multi-temporal filter proposed by (Quegan & Yu 2001). This filter, which is suited for long time-series, allows a suppression of the speckle noise by preserving at the same time the geometrical detail. The final spatial resolution of the geo-coded S1 images is 20 by 20 m.

2.4 Data analysis and proposed approach to the melting phases identification from S1

In this section, the time-series of SWE, LWC and σ^0 for the identification of the melting phases are compared. From this analysis and the background information described in Sec. 2.2, we present the general temporal evolution of the backscattering during the melting process. Finally, on the basis of this analysis we propose a set of simple rules for the derivation of the onsets of each snow melting phase.

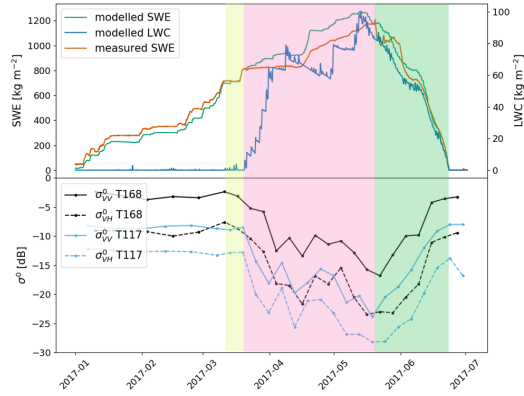
Table 2.4: List of the Sentinel-1 acquisitions and their main characteristics over the five test sites.

Test Site	Relative orbit number*	Time of the acquisition	Orbit Direction	Local incidence angle (LIA)
Zugspitze	117	Afternoon	Ascending	38°
	168	Morning	Descending	39°
Alpe Tumulo	095	Morning	Descending	47°
	117	Afternoon	Ascending	35°
	168	Morning	Descending	40°
Clozner Loch	095	Morning	Descending	43°
	117	Afternoon	Ascending	39°
	168	Morning	Descending	36°
Malga Fadner	044	Afternoon	Ascending	34°
	095	Morning	Descending	48°
	117	Afternoon	Ascending	46°
	168	Morning	Descending	38°
Weissfluhjoch	015	Afternoon	Ascending	43°
	066	Morning	Descending	31°
	117	Afternoon	Ascending	33°
	168	Morning	Descending	41°

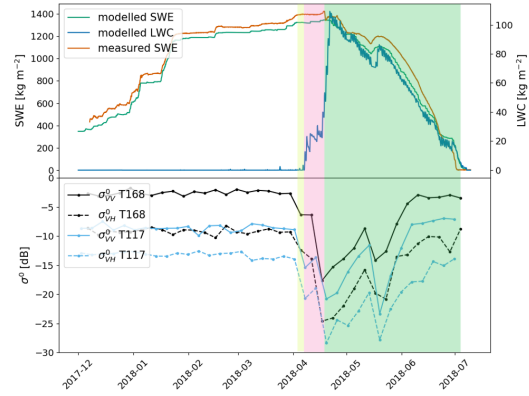
* i.e., track number

2.4.1 Data analysis

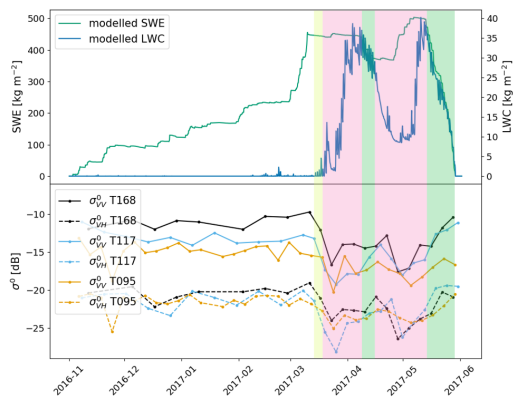
Fig. 2.4 shows the time series of the backscattering coefficient against the measured and/or modeled SWE and LWC for the five test sites during the hydrological years 2016/2017 (left column) and 2017/2018 (right column). Yellow, red and green areas highlight the moistening, ripening and runoff phases respectively. These phases have been identified from the SWE and LWC data according to Sec. 2.2.1. In detail, the moistening phase onset is identified by looking at the liquid water content (LWC) of the snowpack. We empirically established a threshold of 1 kg/m² that has to be satisfied for at least two consecutive days. In other words, a significant melting (and refreezing) cycle should be observed within two days. Among all the isolated moistening events, in this work we focus only on the moistening preceding a ripening phase. However, this does not mean that the SAR cannot detect isolated peaks of melting, if the acquisitions are performed simultaneously to those events. Regarding the ripening phase, we impose the rule to observe an increase of LWC exceeding 5 kg/m² and not decreasing to 0 kg/m² during the diurnal cycles. If the LWC returns to 0 kg/m² for a timing of at least 5 days, we assume that the ripening phase is interrupted. Otherwise, we assume that there is enough penetration of the waterfront into the snowpack to initiate the ripening. Finally, the runoff phase is identified when SWE starts decreasing from its maximum (after the ripening phase is activated). In the case we have both measured and modelled SWE available, we consider measured SWE as reference. The runoff phase ends when SWE has a value of 0 kg/m². The rules are shown in Algorithm 1.



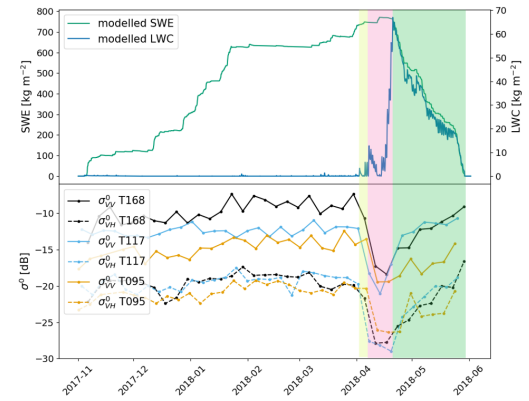
(a) Zugspitze, season 2016/2017



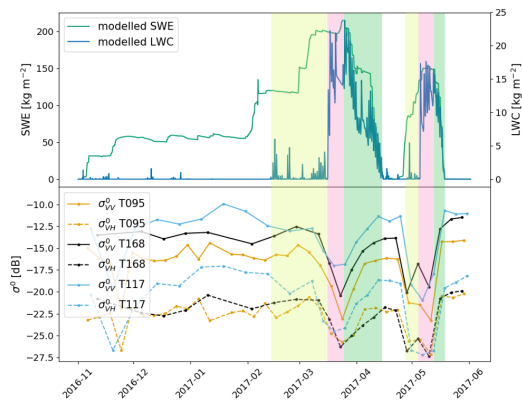
(b) Zugspitze, season 2017/2018



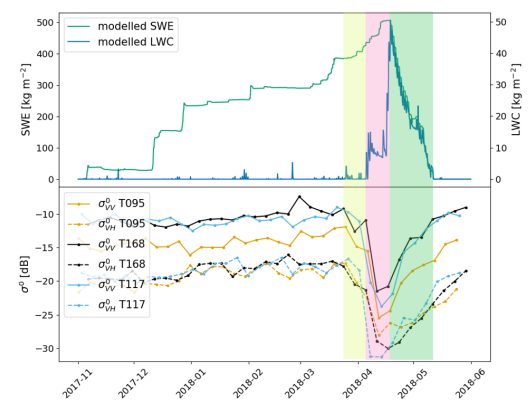
(c) Alpe del Tumulo, season 2016/2017



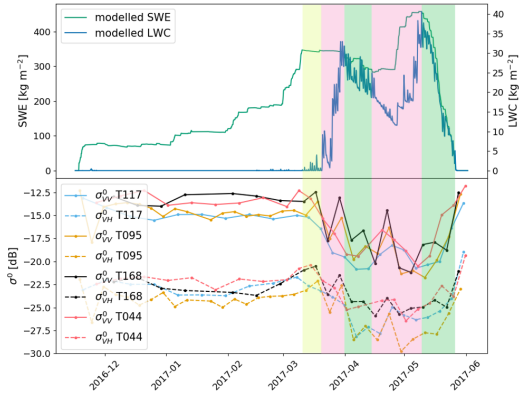
(d) Alpe del Tumulo, season 2017/2018



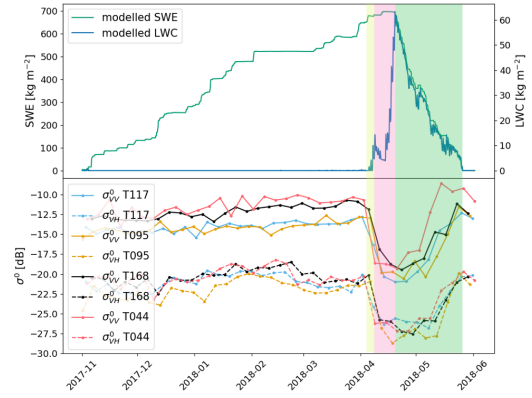
(e) Clozner Loch, season 2016/2017



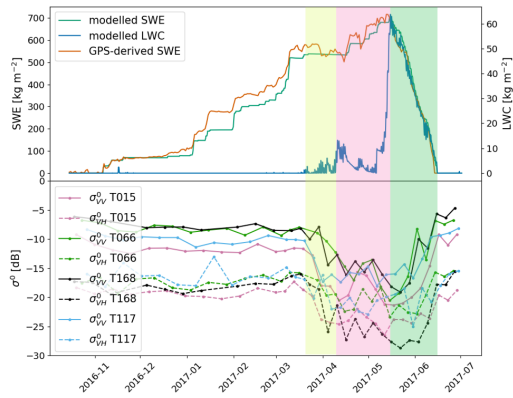
(f) Clozner Loch, season 2017/2018



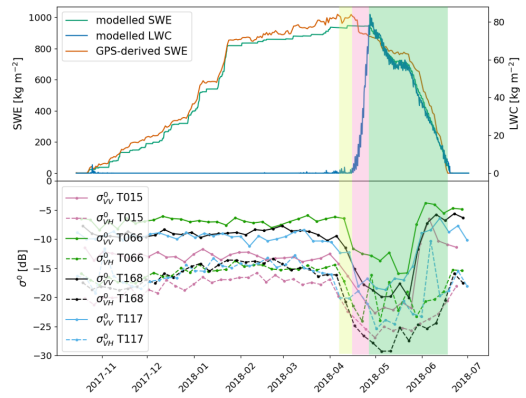
(g) Malga Fadner, season 2016/2017



(h) Malga Fadner, season 2017/2018



(i) Weissfluhjoch, season 2016/2017



(j) Weissfluhjoch, season 2017/2018

Figure 2.4: Temporal evolution of the coefficient of backscattering acquired over the five test sites. The two polarization VV (continuous line) and VH (dashed line) are reported for the different available tracks with different colours. It is compared to LWC and SWE measured in situ at the stations (when available) and modeled with SNOWPACK (contains modified Copernicus Sentinel data, 2016/2018, processed by Eurac Research). The three phases during the melting have been identified from the in situ/modeled data. The first phase of moistening is reported in light yellow, the ripening phase in light red and the runoff in light green. For all the test sites we found that the multi-temporal SAR measurements confirm the identification of the three melting phases. In detail, we systematically found that the SAR backscattering decreases as soon the snow starts containing water and increases as soon as SWE starts decreasing, which corresponds to the release of meltwater from the snowpack.

Algorithm 1: Identification of the melting phases

Input: Liquid Water Content LWC and Snow Water Equivalent SWE observations for a given day d , $d \in \{1, 2, \dots, D\}$ with D total number of days with $SWE > 0$, SWE_{max}

Output: Onset moistening T_M , onset ripening T_R , onset runoff T_{RO}

```
while  $d \leq D$  do
  if  $LWC_{max,d} > 0 \text{ kg/m}^2$  then
    # Snowpack is wet
    # Check moistening phase
    if  $(LWC_{max,d} > 1 \text{ kg/m}^2)$  and  $(LWC_{min,d} = 0 \text{ kg/m}^2)$  for at least 2 days then
       $T_M = d$ 
      # Do not check this condition anymore
      continue
    end
    # Check ripening phase
    if  $(LWC_{max,d} > 5 \text{ kg/m}^2)$  and  $(LWC_{min,d} > 0 \text{ kg/m}^2)$  then
       $T_R = d$ 
      # Do not check this condition anymore
      continue
    end
    # Check runoff phase
    if  $(SWE_d == SWE_{max})$  then
       $T_{RO} = d$ 
      # Do not check this condition anymore
      continue
    end
  end
  else
    | # Snowpack is dry
  end
   $d ++$ 
end
```

In the following, for each of the five test sites i.e., Zugspitze, Alpe Tumolo, Clozner Loch, Malga Fadner and Weissfluhjoch, we will present the detailed comparison of LWC, SWE and the S1 σ^0 time series during the melting process. This will allow the derivation of important information about the possibility to identify the three melting phases in general. In the next section, the outcome of this comparison will be exploited to describe the characteristic behavior of the multi-temporal SAR signal during the melting process.

Zugspitze

For this station, SWE was both measured and simulated and LWC was simulated with SNOWPACK. The temporal evolution of SWE measured by the snow scale and the one simulated with SNOWPACK shows a good agreement. For this station, the tracks T168 (descending, morning) and T117 (ascending, afternoon) are available. The local incidence angle for the two tracks differs of about 1 degree. For the hydrological year 2016/2017 the backscattering remains almost constant during the accumulation phase until the beginning of the moistening phase (Fig. 2.4a). Here, as described in Sec. 2.2.2, the increase of the LWC is accompanied by a decrease of the backscattering from -8.5 dB and -12.7 dB to -14.3 dB and -20.0 dB for respectively VV and VH of the afternoon track T117 between the 19th and the 25th of March 2017 and from -5.8 dB and -12.7 dB to -12.5 dB and -18.1 dB for respectively VV and VH of the morning track T168 between the 27th of March and the 4th of April. The difference in the dropping of the signal acquired by the morning and afternoon track is due to the diurnal melting and refreezing cycles. After this phase, the ripening phase began with oscillations of the backscattering coefficient which on average presented low values. As described in Sec. 2.2.2, the oscillations are due to the snowpack metamorphism, snow stratification and the meteorological conditions. Since the ripening phase is characterized by an increase of the LWC, the time series of the backscattering presents a decreasing trend. Interestingly, the minimum of σ^0 is reached in correspondence to the finishing of the ripening phase and the beginning of the runoff phase i.e., 20th of May 2017. The runoff is instead characterized by a monotonic increase of the backscattering until all snow is melted. This characteristic behavior is unexpected since the backscattering at C-band is not explicitly dependent on SWE. It can be interpreted as follow: when the considered snowpack reaches its saturation condition in terms of the LWC, snow density and internal structure, the backscattering recorded in C-band reaches its minimum value. These snowpack conditions seems to represent the isothermal state before the release of melt water i.e., the end of the ripening phase. After the saturation point is reached, the monotonic increase of σ^0 could be explained by a dominance of the superficial scattering that becomes more and more prominent due to a monotonic increase of the LWC per volume (see Sec. 2.2.2). This behavior continues until the snow disappears. This period corresponds to the runoff formation phase, when SWE starts decreasing. In Sec. 2.4.2 we will discuss a possible explanation of this apparently surprising behavior. Regarding the winter 2017/2018 similar observations were made, but here the snow ripening phase was limited to a very short period and the runoff started very early in mid-April due to strong insolation and high mean daily temperatures up to 5°C the days before. Interestingly, during the runoff phase,

σ^0 started increasing as expected, then it decreased in correspondence of a snow fall (probably wet) followed by a relatively colder period which lasted some days at the end of May 2018 and finally it increased again until the end of the snow season (Fig. 2.4b).

It is worth noting that the two polarizations acquired by S1 provided coherent information. However, few cases in which there is a depolarization of the signal can be spotted during the ripening phase. Here the repeated cycles of melting and refreezing can generate ice layers (Kattelmann & Dozier 1999), which affect the polarization in different ways.

Alpe del Tumulo

For this station, the information about the LWC and SWE were derived through SNOWPACK. The calibration of the model was performed in order to achieve a high agreement in terms of snow height and snow temperature (see Table 2.3). For this station, the tracks T168 (descending, morning), T117 (ascending, afternoon) and T095 (descending, morning) are available. The LIAs for the three tracks are 40, 35 and 47 degrees, respectively.

A very short moistening phase can be identified in both years from the modeled LWC and SWE time series (Fig. 2.4c, 2.4d). These phases are well identified in the σ^0 time series by a drop of the morning and afternoon signal. The situation of the runoff phase 2016/2017 looks similar to Zugspitze for the season 2017/2018: from the LWC and SWE time series two modes are visible suggesting that the runoff was stopped by a cold period (with a new snowfall). This situation is reflected in the time series of the S1 backscattering by the two characteristic “U-shaped” behaviors indicating that a first runoff started after the first minimum of σ^0 and continued for some days in correspondence of the monotonic increase of σ^0 , but then the process was stopped by a new wet snowfall that forced the backscattering to a new minimum. Finally, the runoff phase restarted, and the SAR signal increased again. However, the runoff phases identified from the SAR local minima seem to be anticipated by about two weeks with respect to the modeling results. Regarding the season 2017/2018, the runoff phase showed a more linear behavior which is represented by the characteristic shape of σ^0 time series as the one identified in the Zugspitze test site. It is finally worth noting that, the three tracks (T095 and T168, descending, and T117, ascending) acquired with different LIA show very similar trends.

Clozner Loch

For this station, the information about the LWC and SWE were simulated with the SNOWPACK model. The calibration of the model was performed in order to achieve a high agreement in terms of snow height and snow temperature (see Table 2.3). The tracks T168 (descending, morning), T117 (ascending, afternoon) and T095 (descending, morning) are available for this station. The LIAs for the three tracks are 43, 36 and 39 degrees, respectively.

The season 2016/2017 is characterized by two melting phases (Fig. 2.4e). In fact, the snow was completely melted in the first half of April with a new fresh snowfall at the end of the month. For this reason, we highlighted two different times

the snowpack alteration sequence moistening – ripening – runoff. Interestingly, the time series of the backscattering seems to properly follow the two melting processes with two characteristic “U-shaped” behaviors. The melting process for the season 2017/2018 was more linear (Fig. 2.4f) and the σ^0 time series of the three tracks provides coherent information with the one extracted by analyzing the time series of LWC and SWE.

Malga Fadner

For this station, the information about the LWC and SWE were derived through the SNOWPACK model. The calibration of the model was performed in order to achieve a high agreement in terms of snow height and snow temperature (see Table 2.3). Four tracks are available for this station: T168 (descending, morning), T117 (ascending, afternoon), T044 (ascending, afternoon) and T095 (descending, morning). The LIAs for the three tracks are 46, 48, 38 and 34 degrees, respectively.

The trend of the melting process over the two seasons looks similar to Alpe del Tumulo. The season 2016/2017 is characterized by a consistent snowfall, which happened after an initial runoff phase of the snowpack. This together with a cold period, stopped the process, which was resumed in May (Fig. 2.4g). The time series of the four tracks recorded by S1 backscattering showed two characteristic “U-shaped” behavior indicating that a first runoff started after the first minimum of σ^0 and continued for some days in correspondence of the monotonic increase of σ^0 , but then the process was stopped by a new wet snowfall that forced the backscattering again to the minimum. Nonetheless, the timings are different from the one identified with the modeled data of LWC and SWE. The strong depolarization may indicate a complex structure of the snowpack with different ice layers. The melting process for the season 2017/2018 was more linear and the σ^0 time series of the four tracks provides coherent information with the one extracted by analyzing the time series of LWC and SWE (Fig. 2.4e).

Weissfluhjoch

For this station, the information about the LWC and SWE were simulated with SNOWPACK, additionally SWE GPS-derived measurements were available. The calibration of the model was performed in order to achieve a high agreement in terms of snow height and SWE (see Table 2.3). The tracks T168 (descending, morning), T117 (ascending, afternoon), T015 (ascending, afternoon) and T066 (descending, morning) are available for this station. The LIAs for the three tracks are 41, 33, 43 and 31 degrees, respectively.

The season 2016/2017 is characterized by an initial moistening phase, followed by a ripening phase that was delayed by a cold period, when the LWC decreases almost to 0 (Fig. 2.4i). In the middle of May a runoff phase started. The backscattering followed the different phases as expected. The season 2017/2018 is more regular, with a monotonic increasing of LWC indicating a short moistening followed by a regular ripening and the runoff. In this case the measured SWE anticipated the runoff onset of about one week w.r.t. the modeled SWE, which seems more in accordance with the S1 data. The backscattering shows a similar behavior of other

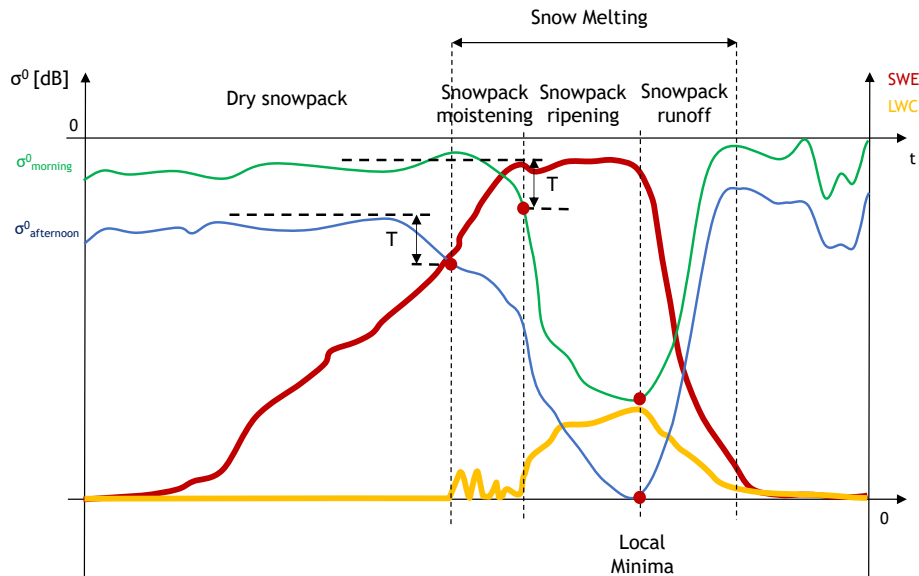


Figure 2.5: Schematic representation of the evolution of the backscattering coefficient acquired in the morning (green line) and in the afternoon (blue line) compared with LWC (yellow line) and SWE (red line) evolution. The offset between the morning and afternoon signals is due to the generally different local incidence angle of the ascending and descending acquisitions in mountainous regions. The three melting phases are identified from the LWC and SWE information. Correspondingly, the rules for the identification of each phase from the time series of σ^0 is highlighted: a decreases of at least T [dB] from the mean value in dry snow condition applied to the afternoon and morning signals identifies the moistening and ripening onsets respectively. The local minima of the signals indicate the runoff onset.

previously discussed cases with the characteristic “U-shaped” signal except for the T066 that present several oscillations in the VH polarization.

2.4.2 Temporal Evolution of the Backscattering

From the comparison carried out in the previous section and by taking into account the main backscattering mechanisms described in Sec. 2.2.2, it is possible to derive and explain the temporal behavior of σ^0 generated by a C-band SAR over a sufficiently deep snowpack located in an open space that present a linear transition between the three melting phases. By analyzing the backscattering time series of the same pixel, the contribution of the LIA is always the same, making the values of the time series comparable. Fig. 2.5 shows an illustrative evolution of σ^0 for a complete hydrological year that summarizes both the state-of-the-art background and the observations done on real data. As described later, this conceptual time signature will allow to derive a set of rules for the identification of the melting phases also in time series of backscattering never observed before or in independent dataset (e.g., Veyssi re et al. 2018, Lievens et al. 2019).

Before the snow covers the terrain, σ^0 is influenced by the fluctuation of the soil moisture (Ulaby et al. 1996). Then, generally the first snow fall is wet or it covers

relatively warm terrain resulting in a wet snowpack. This generates low backscattering values in the SAR response. This situation, which in alpine environments usually lasts for short periods, ends either with a significant decrease of the temperature that brings the snowpack to a dry condition or with a complete melting of the snowpack. It is also possible that the soil freezes before the first snowfalls. In this case the coefficient of backscattering decreases and stabilizes around a given value, not being affected by the soil moisture anymore.

As soon as the snowpack starts incorporating liquid water, the melting period starts. It can be divided into three important phases as described in Sec. 2.2.1, i.e., the moistening, the ripening and the runoff phases. The first phase is related to the initial moistening of the snowpack. As discussed previously, the liquid water is introduced in the snow by rain and/or melt due to temperature and the incoming flux of shortwave radiation. At the beginning of the process the value of LWC is low and therefore the SAR backscattering experiences a relevant decrease in its value since the volumetric scattering dominates the total backscattering. The drop of the signal is recognizable by imposing a given threshold T . During the moistening, the wetting front may be visible only during the afternoon and not in the morning since the snowpack is still subjected to the diurnal cycles of melting and refreezing. As soon as the wetting front has penetrated the superficial insulating layer of the snowpack, the wet snow becomes visible also in the SAR early morning acquisitions. Please note that the systematic offset between the morning and afternoon signals represents the generally different local incidence angle of the ascending and descending acquisitions in mountainous region. At this point the phase of snowpack ripening starts. In this phase, the wetting front keeps penetrating the snowpack conducting it to an isothermal condition. During the ripening phase, which is influenced by the weather and the snowpack conditions, σ^0 varies according to the snow conditions but with an overall decreasing trend due to the increase of LWC.

We observed that the minimum of σ^0 is reached in correspondence of the finishing of the ripening phase and the beginning of the runoff phase for all the ten time series observed (see Sec. 2.5). The runoff is instead characterized by a monotonic increase of the backscattering until all the snow is melted. To our knowledge, this characteristic behavior has been never observed in the literature before. Our interpretation is as follow: when the considered snowpack reaches its saturation condition in terms of LWC and snow structure, the backscattering recorded in C-band reaches its minimum value. This snowpack condition seems to correspond with the isothermal condition i.e., the end of the ripening phase. After the saturation point is reached, the monotonic increase of σ^0 could be explained by one or the combination of the following factors: i) an increase of the superficial roughness; ii) a change in the snow structure i.e., increase of the density and increase of grain size and; iii) at the end of the melting, the presence of patchy snow creates a situation of mixed contribution inside the resolution cell of the SAR and therefore a further increase of the total backscattering is recorded.

On the basis of this analysis, we propose here a simple set of rules to identify the snow melting phases on the basis of the multi-temporal SAR signal. The start of the melting process can be identified by a decrease of the multi-temporal SAR signal recorded in the afternoon of 2 dB or more w.r.t. the general winter trend.

This threshold has been also proposed by (Nagler et al. 2016). As soon as also the backscattering time series recorded in the morning experience a decrease of more than 2 dB, we assume that the ripening phase begins. This phase, characterized by several oscillations, ends when both the morning and afternoon σ^0 reach their local minimum. We propose the mean date among the local minima as the start of the runoff phase, which is characterized by a monotonic increase of the coefficient of backscattering. These rules are summarized in Algorithm 2. It is worth noting that, the rules are not calibrated on the observations done in Sec. 2.2.1, but reflect the literature background.

Algorithm 2: Identification of the melting phases

Input: Multitemporal backscattering observations for different tracks,
 $\sigma_{morning}$ and $\sigma_{afternoon}$, for a given day d , $d \in \{1, \dots, d, \dots, D\}$ with D
total number of observations

Output: Onset moistening T_M , onset ripening T_R , onset runoff T_{RO}

while $d \leq D$ **do**

if $\sigma_{afternoon,d} - \sigma_{dry} \geq -2$ dB **then**

Snowpack is wet

Check moistening phase

if $(\sigma_{morning,d} - \sigma_{dry} < -2$ dB) **then**

$T_M = d$

Do not check this condition anymore

continue

end

Check ripening phase

if $(\sigma_{morning,d} - \sigma_{dry} \geq -2$ dB) **then**

$T_R = d$

Do not check this condition anymore

continue

end

Check runoff phase

if $(\sigma_d == \sigma_{min})$ **then**

$T_{RO} = d$

Do not check this condition anymore

continue

end

end

else

Snowpack is dry

end

$d ++$

end

In the next section we applied these simple set of rules in order to identify the melting phases for each of the five considered test sites. Moreover, the same rules

are used to identify the runoff onset for each SAR pixel in the topographically well-defined catchment of the Zugspitzplatt obtaining a spatially distributed map of the runoff timing.

2.5 Application of the proposed approach to 1D and 2D cases

In this section, we present the results obtained for the snow melting phases identification from the time series of backscattering recorded from S1 over the five selected alpine test sites. The results are compared with the derivation of the melting phases considering the observed and modeled measurements of LWC and SWE. Finally, we present the result of the runoff onset identification in the two dimensional space of the original 20 m SAR images for the Zugspitze catchment.

2.5.1 Identification of snow phases from Sentinel-1 in the five alpine test sites

Table 2.5 reports the comparison of the onset dates for the melting phases for each of the considered test sites. The phases were identified from the backscattering time series according to the rules expressed in the previous section. If more than two acquisitions i.e., ascending and descending are available for one test site, the first date representing the onset for the moistening and ripening phase among all available tracks is selected. The runoff onset is identified as the mean date among the local minima. These rules can be automatically applied without any human supervision.

On average, the moistening phase was identified with a r.m.s. error of 6.5 days. For the ripening phase the SAR time series allowed the identification with 4.5 days of r.m.s. error. Finally, the runoff was identified with a r.m.s. of 8 days (4 days r.m.s. error without considering Alpe del Tumolo for the years 2016/2017 and Weissfluhjoch for the years 2017/2018 where the runoff process were articulated). Considering the repetition frequency provided by S1 and the possible uncertainty of the SNOWPACK modeling (Wever et al. 2015), the produced results demonstrate the effectiveness of using the SAR for characterizing the snow melt process.

In some cases, the proposed rules could not be applied and the melting or ripening onset could not be identified from the S1 data. This is mainly due to the short melting or ripening periods that occurred during some years in the selected test sites. However, it was always possible to identify the runoff onset. In these cases, the 6 days repetitions provided by S1 is not adequate to sample this situation and it happens that the moistening phase is captured by the morning acquisition before than the afternoon acquisition (i.e., Zugspitze season 2016/2017 and 2017/2018, Clozner Loch season 2016/2017 second moistening phase and 2017/2018) or the first signal drop is reached at the same time of the local minima (i.e., Clozner Loch season 2017/2018). One can also notice that, for the first runoff identified in the season 2016/2017 for Malga Fadner, the proposed rules failed since for T168 no local minimum was clearly identified (Fig. 2.4g).

	S1	Ref	Δ [days]	
Moistening	-	11/03	-	
Ripening	23/03	21/03	+2	■
Runoff	20/05	20/05	0	

(a) Zugspitze, season 2016/2017

	S1	Ref	Δ [days]	
Moistening	-	04/04	-	
Ripening	05/04	08/04	-3	■
Runoff	18/04	18/04	0	

(b) Zugspitze, season 2017/2018

	S1	Ref	Δ [days]	
Moistening	19/03	14/03	+5	■
Ripening	23/03	20/03	+3	■
Runoff	24/03	08/04	-14	■
	01/05	13/05	-13	■

(c) Alpe del Tumulo, season 2016/2017

	S1	Ref	Δ [days]	
Moistening	07/04	02/04	+5	■
Ripening	11/04	07/04	+4	■
Runoff	14/04	20/04	-6	■

(d) Alpe del Tumulo, season 2017/2018

	S1	Ref	Δ [days]	
Moistening	23/02	14/02	+9	■
	-	29/04	-	
Ripening	12/03	16/03	-4	■
	28/04	05/05	-7	■
Runoff	22/03	25/03	-3	■
	08/05	13/05	-5	■

(e) Clozner Loch, season 2016/2017

	S1	Ref	Δ [days]	
Moistening	-	25/03	-	
Ripening	-	06/04	-	
Runoff	12/04	18/04	-6	■

(f) Clozner Loch, season 2017/2018

	S1	Ref	Δ [days]	
Moistening	19/03	14/03	+5	■
Ripening	23/03	20/03	+3	■
Runoff	10/04	30/03	+11	■
	07/05	09/05	-2	■

(g) Malga Fadner, season 2016/2017

	S1	Ref	Δ [days]	
Moistening	07/04	05/04	+2	■
Ripening	11/04	07/04	+4	■
Runoff	21/04	19/04	+2	■

(h) Malga Fadner, season 2017/2018

	S1	Ref	Δ [days]	
Moistening	25/03	19/03	+6	■
Ripening	04/04	09/04	-5	■
Runoff	14/05	16/05	-2	■

(i) Weissfluhjoch, season 2016/2017

	S1	Ref	Δ [days]	
Moistening	06/04	02/04	+4	■
Ripening	10/04	17/04	-7	■
Runoff	08/05	19/04	+19	■

(j) Weissfluhjoch, season 2017/2018

Table 2.5: Onset times for the melt phases identified in the five test sites using the LWC and SWE (reference - Ref) and Sentinel-1 (S1) with the method proposed in the previous section.

2.5.2 Extension to a 2D analysis of the runoff onset: the Zugspitzplatt catchment

In this section we evaluate how the identification of the runoff onset is performed at a catchment scale. In particular, we considered the multi-temporal behavior of each pixel acquired by S1 over the Zugspitzplatt during the hydrological year 2017/2018. The plateau (1500-2700 m a.s.l.) on the southern slope of Mt. Zugspitze summit (2962 m a.s.l.) is well suited for this application scenario, since it is proven that all surface and ground water is drained to the Reintal valley in the east by the Partnach River (Rappl et al. 2010). With regard to a potential transport of contaminants that are stored in the snowpack and released with the first snowmelt (Hürkamp et al. 2017), the knowledge of the runoff onset can provide important information for the scope of action concerning the management of countermeasures or planning actions to mitigate potential soil and water contamination.

As illustrated in the previous section, the runoff onset was identified by locating the minimum of the backscattering time series. In order to increase the robustness of the detection, we considered the mean of backscattering of close pixel presenting the same characteristics in terms of altitude, exposition and slopes. In detail, belts of 100 m were considered for the altitude. Slope was divided in three classes between 0-20, 20-40 and 40-60 degrees. Four aspect classes were considered, i.e. North, East, South and West. Finally, a local incidence angle ranging from 25 to 65 degrees was divided in 8 classes with 5 degrees span, avoiding layover and shadow effects. All the homogeneous classes generated by the different combinations were aggregated. The forested areas were masked using the Copernicus tree cover density map (<https://land.copernicus.eu/pan-european/high-resolution-layers/forests/tree-cover-density/status-maps/2015>). Moreover, since in this illustrative example we are interested in the main runoff contribution, the proposed algorithm is looking for local minima of the backscattering time series only after January 2018. This to exclude isolated wet snowfalls or complete early melting events typical of the beginning of the seasons.

Fig. 2.6 shows the runoff onset identified by the proposed method. As one can notice, the regions at lower altitude started the runoff phase before the areas at higher altitude. The same consideration can be done for the pixels north exposed versus the south exposed ones. Interestingly, the last areas that start the runoff phase in the catchment are the glacierized areas (Northern and Southern Schneeferner glacier) and north faced slope areas. A selection of the backscattering time series is reported at the bottom of the Fig. 2.6 for six points selected at different altitudes. As one can notice the characteristic behavior described in Sec. 2.4.2 is always visible in the real data even though they were not analyzed before.

2.6 Discussion

Snow monitoring and/or prediction systems are typically based on real-time snow ground observations (e.g., WSL Swiss monitoring system <https://www.slf.ch/en/avalanche-bulletin-and-snow-situation/snow-maps.html>), snow hydrological models (e.g., Mysnowmap for the European Alps <https://www.mysnowmaps.com>

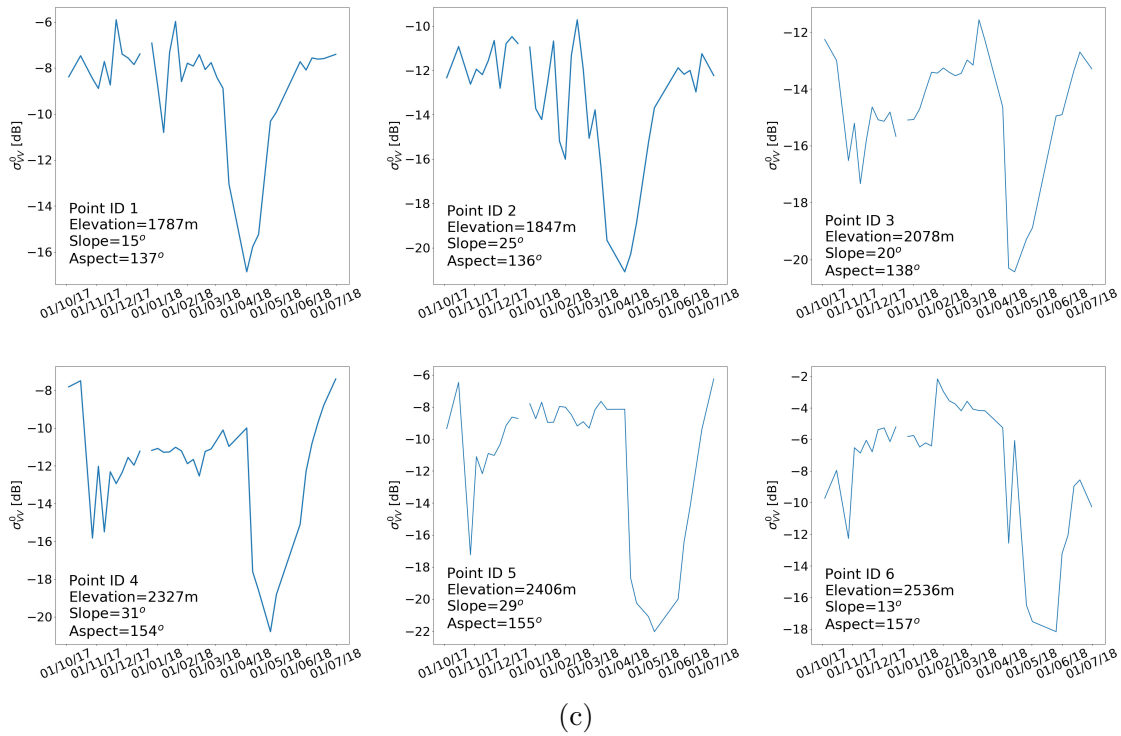
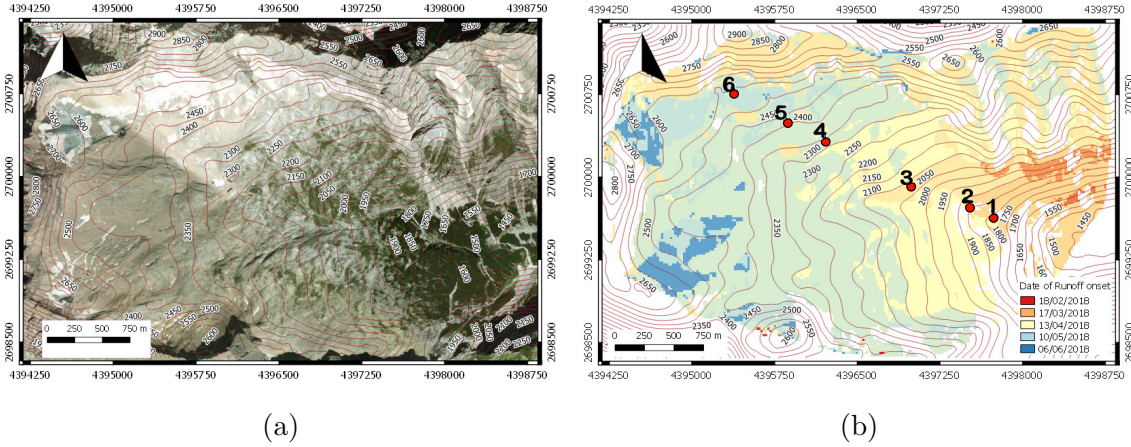


Figure 2.6: Runoff onset for the Zugspitzplatt catchment. (a) Test site presentation (©2019 Microsoft Corporation ©2019 Digital Globe ©CNES(2019) Distribution Airbus DS) (b) Map of the runoff onset (contains modified Copernicus Sentinel data, 2018, processed by Eurac Research). The runoff started at lower altitude and at the south exposed slopes. The last areas to have the runoff in the catchment are the high-altitude area, the north exposed and glacierized areas. (c) The multi-temporal backscattering time series for the selected points along the transect identified in (b) with red dots. All the time series present the characteristic “U-shaped” pattern.

/), optical and passive microwave remote sensing observations (e.g., ESA Climate Change snow Initiative snow-CCI <http://cci.esa.int/snow>), or the combination of different sources (e.g., the US National 515 Operational Hydrologic Remote Sensing Center (NOHRSC) <https://www.nohrsc.noaa.gov/>). The accuracy of such systems varies, but in general is limited by the poor information on snow precipitation, especially in mountain areas. This could lead to errors of several days, even weeks, in the estimation of the snow disappearance time (Engel et al. 2017). The approach described in this chapter allowed the identification of the melting phases for the five considered test sites with an rmse of 6 days for the moistening phase, 4 days for the ripening and 7 days for the runoff phase. Therefore, it could be potentially useful to improve the performances of snow monitoring.

It is important to underline that, in order to predict runoff, further hydrological modeling is needed beside the information provided by the proposed approach. While the runoff production below the snowpack starts quickly, being snow permeable to water, then the streamflow production can be delayed of several days, even weeks, depending on catchment size and hydrological behavior (Rinaldo et al. 2011). Therefore, even if we do not propose a real-time implementation, we think that, combining the information on the snow melting phases based on the principles presented in Sec. 2.4.2 and easily available real-time and historical auxiliary data such as temperature or historical streamflow, it is possible to develop an algorithm to extract valuable information for the anticipation of the peak stream runoff phase.

Knowing the snow melting phases within just a few days delay can have very important applications for water resources management (e.g., hydropower production or irrigation administration). In detail, the information provided by the proposed approach can be ingested in operational hydrological modeling systems. In detail, the ingestion of remote sensing information for improving snow modeling and monitoring has been extensively applied in the past (e.g., Molotch & Margulis 2008). So far, the most common variable assimilated is snow cover fraction from optical sensors since this is the most available information acquired using remote sensing. In our case, we would need to assimilate either information on presence/absence of snow liquid water content or on the snow depletion curve, which can be computed for the first time from the real beginning of the melting (i.e., runoff onset) from high resolution remote sensing data. From a theoretical point of view, this is feasible. However, if the assimilated variable is snow liquid water content, only snow models which explicitly simulate snow liquid water content can be used. Usually physically based, energy-based snow models such as GEOtop (Endrizzi et al. 2014), AMUNDSEN (Strasser et al. 2011), CROCUS (Brun et al. 1992) or SNOWPACK/ALPINE3D (Bartelt & Lehning 2002, Lehning et al. 2006) are suitable for this purpose.

The possibility to use state of the art Radiative Transfer (RT) models to simulate the multi-temporal behavior of the backscattering presented in Sec. 2.4.2 has also been investigated. Although wet snow is of great importance for many applications, the most widely used models have been tested and applied mainly in dry snow conditions (Picard et al. 2018, Proksch et al. 2015). In detail, during the melting process the increase of superficial roughness, LWC and density and the coarsening of the snow grains play an important role on the backscattering mechanisms. In-

deed, when the LWC increases, the absorption coefficient increases, the penetration depth decreases, and the total backscattering is influenced more and more by the superficial roughness of the snow. As discussed in the background Sec. 2.2.2, at the best of our knowledge, only few works have specifically addressed the wet snow modeling at C-band i.e., (Shi & Dozier 1995, Nagler & Rott 2000, Magagi & Bernier 2003). Differently from more advanced models such as SMRT (Picard et al. 2018) or MEMLS3&a (Proksch et al. 2015), these models assume independent scattering. Even though Shi & Dozier (1995) and Magagi & Bernier (2003) indicate a positive correlation between largely wet snowpack and the superficial roughness, Kendra et al. (1998) on the basis of ground experimental analysis, expressed some doubts on the realistic behavior of such models. Therefore, wetsnow RT modeling requires dedicated efforts and validation campaigns, which has never been systematically conducted for characterizing the multi-temporal snow roughness, which are out of the scope of this chapter and will be left as future work.

It is finally worth noting that the availability of multi-temporal data, acquired regularly over the entire globe and freely accessible, opens new opportunities to monitor dynamic phenomena. In particular, monitor snow depth and snow water equivalent in a systematic and spatially distributed manner would be crucial for a proactive management of the water resources. The recent paper by Lievens et al. (2019) proposes an empirical algorithm for snow depth retrieval from S1 at 1 km resolution. The authors suggest a C-band sensitivity to snow height generated by the cross-polarized information. This was never fully recognized before in the literature. Even though the focus of our research is only on the snowmelt, by considering the 20 m multi-temporal S1 data acquired over the five test sites studied in the presented work, we provide some remarks that may be useful for future works in this context. It is worth noting that all the backscattering time series in the two polarization showed in the paper by Lievens et al. (2019) exhibit the characteristic shape identified and analyzed in the presented study. Notwithstanding, when considering our five test sites, the ratio σ_{VH}/σ_{VV} seems not providing clear evidences that the cross polarization is sensible to the increase (or decrease) of snow depth (or SWE) during both the accumulation and melting period (see Fig. 2.4). Nevertheless, our five test sites represent a restricted and very specific dataset w.r.t. the global one considered by Lievens et al. (2019). However, this does not exclude that different manipulation of the S1 data (e.g., spatial and temporal averaging) and the empirical incidence angle normalization proposed in Lievens et al. (2019), which were not taken into account in our experiments, may contribute to increase the sensitivity of the backscattering to the snow height, by possibly removing the source of noise. In conclusion, despite the lack of a generally accepted physical explanation, this work shows how the rich amount of SAR data made available with a high repetition interval can allow the monitoring of the complex processes related to the snow evolution in a manner that was never addressed before. We believe this will be one of the most interesting research topics in the future.

2.7 Conclusions

In this chapter, we analyzed the correlation between the multi-temporal SAR backscattering and the snow melt dynamics. We compared Sentinel-1 backscattering with LWC and SWE measurements derived from in situ observations and process-based snow modeling simulations for five alpine test sites in Italy, Germany and Switzerland considering two hydrological years. We found that the multi-temporal SAR measurements allow the identification of the three melting phases that characterize the melting process i.e., moistening, ripening and runoff with a good agreement considering the revisit time of Sentinel-1. In detail, we found that in the considered sites the SAR backscattering decreases as soon as the snow starts containing water, and that the backscattering increases as soon as SWE starts decreasing, which corresponds to the release of meltwater from the snowpack. We discuss the possible reasons of this increase, which are not directly correlated to the SWE decrease, but most probably to the different snow conditions, which change the backscattering mechanisms. From this study we define a set of simple rules that can be applied to the multi-temporal SAR backscattering in order to identify the melting phases. We showed that by applying these rules, the identification of the melting phases was possible for the five considered test sites with an rmse of 6 days for the moistening phase, 4 days for the ripening and 7 days for the runoff phase. Moreover, the same rules were applied for the identification of the runoff onset for the entire Zugspitzplatt catchment with reasonable results even if further hydrological analyses have to be performed. The presented investigation could have relevant application for monitoring and predicting the snowmelt progress over large regions. A better understanding of the spatial and temporal evolution of melting dynamics in mountain regions and the knowledge on the onset of melt water runoff can help to predict floods and define the scope of action to mitigate potential contaminant distributions in soils and surface water.

As future developments we plan to develop and test an automatic method to identify the three melting phases of a snowpack using larger validation dataset (e.g., SNOTEL) and allow to properly discuss the spatial and temporal evolution of snow water content and runoff in mountainous region. Moreover, we investigate the reasons of the increase of the backscattering in correspondence of the decrease of SWE through in situ experiments that take into account the hypothesis expressed in this chapter. This will help the development of the RT models in wet snow conditions.

Acknowledgements

We thank the Bavarian Avalanche Warning Service (Lawinenwarnzentrale Bayern) and the Environmental Research Station Schneesfernerhaus (UFS) for providing the measurement data for the German test site Zugspitze, the Hydrographic office of the Autonomous province of Bolzano for providing the data for the Italian test sites of Alpe Tumulo, Clozner Loch and Fadner Alm and the WSL institute for snow and avalanche research SLF for providing the data for the Switzerland test site Weissfluhjoch. The work of the MC and GB were financed through the CRYOMON-SciPro project, founded by the Euregio Science Fund 1st call, project number IPN

10. Parts of the measurements and snow sensor installations at the Zugspitze station were funded by the Bavarian Ministry of the Environment and Consumer Protection (BayStMUV) in the framework of the Virtual Alpine Observatory (VAO) project.

Chapter 3

A Novel Approach Based on a Hierarchical Multi-Resolution Analysis of Optical Time Series to Reconstruct the Daily High-Resolution Snow Cover Area

High-resolution (HR) snow cover maps derived by remotely sensed images are an asset for data assimilation in hydrological models. However, the current satellite missions do not provide daily HR multi-spectral observations suitable for an accurate snow monitoring in alpine environments. On the contrary, low-resolution (LR) sensors acquire daily information of snow cover fraction (SCF) but at an inappropriate spatial scale. This chapter¹ proposes a novel approach that combines multi-source and multi-scale acquisitions to infer the daily HR snow cover area (SCA) for mountainous basins. The approach builds on the assumption that inter-annual snow patterns are both affected by the local geomorphometry and meteorology. We derive these patterns through a hierarchical multi-step approach based on historical statistical analyses on a long and sparse HR time-series. At each step, we obtain binary HR snow cover maps with higher number of reconstructed pixels but decreasing level of confidence. Historical data are used to estimate the probability that a HR pixel is covered by snow according to two possible multi-scale strategies: i) HR gap-filling, or ii) LR downscaling. These analyses lead to the identification of the patterns that regularly appear given certain conditions. When no systematic patterns are observed, we reinforce the inference of the pixel class by a generalized additive model (GAM) that exploits not only the historical data but also explicit geomorphometric, global snow and multi-temporal properties. The proposed approach has been validated on a catchment in the Sierra Nevada, USA, for three hydrological years (2017-2019)

¹This chapter has been published in:

Premier, V., Marin, C., Steger, S., Notarnicola, C. Bruzzone, L. (2021), ‘A novel approach based on a hierarchical multi-resolution analysis of optical time series to reconstruct the daily high-resolution snow cover area’, *IEEE Journal of Selected Topics in Applied Earth Observations and Remote Sensing* **14**, 9223–9240.

showing an average overall accuracy of 92%.

3.1 Introduction

Snow cover monitoring is of crucial importance to accurately control and manage the water resource availability (Immerzeel et al. 2020). The presence of snow has relevant effects at different scales. At a regional scale, snow strongly affects the mountain watershed hydrology, being one of the main contributor to streamflow runoff and groundwater recharge (Dyer 2008, Earman et al. 2006). Moreover, the seasonal snow accumulation and melt have a large impact also on the ecosystem functioning, the human activities and the economic growth of the considered area. Just to cite some examples, snow is a main source of freshwater provision, hydropower plant reservoirs, and ski tourism (Jones 2001, Beniston et al. 2018, DeWalle & Rango 2008*b*, Winther & Hall 1999). At a global scale, due to its radiative and thermal properties, snow affects the climate system by influencing the atmosphere and ground exchanges (Zhang 2005, Ge & Gong 2010). At its maximum annual expansion, snow can cover more than half the Northern Hemisphere land area (Groisman 2001). Hence, global snow cover variations need to be monitored, especially in the context of a changing climate (e.g., Notarnicola 2020).

Remote sensing (RS) is a valuable tool for snow monitoring, since it provides spatially distributed information over large areas also when they are difficult to access (Nolin 2010, Rees 2005). A key property that can be retrieved by optical sensors mounted on board of satellites is the snow cover area (SCA). Time-series (TS) of SCA provide a measurement of the snow cover depletion rate, which can be either exploited for snow water equivalent (SWE) reconstruction, (e.g., Martinec & Rango 1981) or assimilated in hydrological models (e.g., Thirel et al. 2013, Rodell & Houser 2004). Furthermore, SCA is a proxy for many variables, e.g., related to assess the impact of climate changes (Notarnicola 2020) or to predict the availability of water discharge (Callegari et al. 2015).

The SCA is derived from optical multi-spectral sensors by exploiting the spectral signature of snow. In general, the identification of snow-covered pixels is possible through the normalized difference snow index (NDSI), which is calculated as the normalized difference between the visible and short-wave infrared (SWIR) components of the electromagnetic spectrum (e.g., Dietz et al. 2012). The output of the most known state-of-the-art methods (e.g., Dozier & Painter 2004, Klein et al. 1998) is a binary thematic map with snow and snow-free labels. More advanced methods deal with the partially snow-covered pixels and retrieve the snow cover fraction (SCF) at pixel level, i.e., the percentage of snow within the pixel. This can be achieved by assuming a linear relationship between NDSI and SCF (e.g., Salomonson & Appel 2006, Gascoin et al. 2020). Other authors also make use of unmixing techniques (e.g., Painter et al. 2009). Beside these methods, machine learning (ML) methods have also been explored both for binary classification (Niroumand-Jadidi et al. 2020) and for SCF (Czyzowska-Wisniewski et al. 2015).

The trade-off between spatial and temporal resolution of the current satellite missions negatively affects the proper exploitation of SCA maps to understand processes related to snow and atmospheric energy exchanges, the hydrology, or the ecosystem functioning of a given area (Oaida et al. 2019, Liston 2004, Vionnet et al. 2020). From one side, daily low-resolution (LR) SCF maps are available but with a spatial resolution of hundreds of meters that is not appropriate especially when dealing with complex topography and inhomogeneous snowfalls. In fact, local snow spatial patterns due to wind redistribution, snow-canopy interaction or orographic influences are not accurately detected. This together with systematic errors introduced in the SCF retrieval, due for example to the variable illumination and viewing angle, different types of land cover, and atmospheric effects (Dozier & Painter 2004, Klein et al. 1998, Dozier et al. 2008) invalidate the possibility to properly appreciate the spatial and temporal heterogeneity of SCA. On the other hand, high-resolution (HR) satellite images introduce large benefits to the alpine snow monitoring allowing for instance the proper observation of the release of localized SWE storages, which are important for predicting the river runoff especially in the late melting season (DeBeer & Pomeroy 2017) or for ecology studies (Mark et al. 2015). However, they are available with a low temporal resolution. This does not permit to monitor quick SCA changes thus precluding the correct identification of the snow onset and snow end date (Aalstad et al. 2020, Selkowitz et al. 2014, Durand et al. 2008). In the past, HR images were provided mainly by the Landsat missions, which acquired one image every 16 days, thus resulting inadequate for temporally characterizing the SCA. Nowadays, thanks to the recent introduction of the Copernicus Sentinel-2 (S2) mission, we can benefit free-of-charge of new images nominally acquired every 5 days (due to polar orbits the revisit time is increasing gradually from the equator to the poles). This is opening the possibility to systematically produce HR SCA TS increasing the spatial and temporal sampling of the snow related processes. However, there is still the need to fuse multi-temporal and multi-source information to obtain HR TS with a daily temporal resolution, which is more adequate for snow monitoring (Malnes et al. 2015).

The high temporal correlation of snow cover has been largely exploited in several state-of-the-art methods that deal with cloud obstruction by propagating the last/next available information (Gafurov & Bárdossy 2009, Da Ronco & De Michele 2014, Lindsay et al. 2015). Other methods are based on either interpolating SCA (Dozier et al. 2008) or considering NDSI changes over time of similar cloud-free pixels (Chen, Wang, Guo, Xie & Sirelkhatim 2020). However, these methods are strongly influenced by the duration of the cloud presence and may not detect rapid phenomena typical of snow accumulation and/or melting. Spatio-temporal correlation of snow distribution has also been investigated (Li et al. 2017, Parajka & Blöschl n.d., Hou et al. 2019, Tran et al. 2019) exploiting mainly the elevation (Gafurov & Bárdossy 2009, Da Ronco & De Michele 2014, Parajka et al. 2010) but also other digital elevation model (DEM) derived features (López-Burgos et al. 2013, Poggio & Gimona 2015). The historical information provided by long TS has also been exploited to fill the cloud gaps by considering the conditional probability (CP) of having a class transition (snow/snow free) during the cloud covered period. This

probability has been calculated during the same historical decade in which the clouds affected the study areas (Niroumand-Jadidi et al. 2020). These methods were all developed for low-resolution (LR) images (Li, Jing, Shen & Zhang 2019) but they represent a possible starting point for HR gap-filling (e.g., Liu et al. 2020). However, the application of these techniques to HR TS would suffer both by i) the presence of larger gaps due to the sparser acquisitions that characterize HR time series; and ii) the high spatial variability of SCA in complex terrains that is neglected in the state of the art methods. Moreover, the reconstruction is not based on a direct observation but it is inferred by exploiting the spatio-temporal correlation under the assumption that no sudden SCA change can happen between the observations. In this context, multi-source techniques can improve the sampling time. Fusion techniques that merge LR and HR data have been proposed and provide daily snow cover maps with a resolution of 30 m (Mityók et al. 2018, Berman et al. 2018). These methods are based on long NDSI TS which are smoothed through interpolation techniques (e.g., cubic splines), which provide good performances if the accumulation and melting are not subjected to abrupt changes. Moreover, HR and LR NDSI values are assumed to follow similar trends without considering the intrinsic variability due to the different spatial resolution. Multi-source methods for fusing optical and microwave observations have also been proposed (Deng et al. 2015). Other techniques fuse information extracted from in-situ snow measurements by computing the CP to observe a pixel as snow given the presence of snow in a set of meteorological stations or other pixels (Gafurov et al. 2015, Dong & Menzel 2016, Chen, Wang, Guo, Xie, Wang & Hao 2020). The implicit limitation of such methods is that the results are strongly affected by the number of weather stations available for the study area. Moreover they have not been explored using HR data.

In this work, we propose a novel multi-source approach to infer the daily SCA in mountainous basins at a high spatial resolution starting from sparsely acquired TS of high- and low-resolution snow cover maps. The inference process exploits the high temporal and spatial correlation of the snow cover based on the physical processes that lead to the snow accumulation and redistribution by considering the historical information in a novel way. In particular, we observe the recurrent distribution of snow in time which takes place following predominant regular inter-annual patterns. These patterns are influenced by the geomorphometric features of the considered pixels. Similar characteristics in terms of elevation, slope, and aspect lead to similar response during and after a meteorological event (snow accumulation, distribution, and melting) (Mendoza et al. 2020). For this reason, the proposed approach is designed for hydrological catchments or areas driven by the same precipitation events. Moreover, the spatial resolution of HR sensors is particularly suitable to identify the snow cover patterns in complex terrain such as alpine catchments. To this purpose we exploit all available multi-source observations with the main advantage to detect quick phenomena, as for example quick snowfall events, which are generally missed by the state-of-the-art methods.

The method is made up of five different steps grouped in two main blocks. First, we extract the snow patterns by means of historical statistical analyses on a long HR

TS without directly considering other features. In this phase, the geomorphometric information is intrinsically embedded in the history. The patterns are extracted by deriving the conditional probability (CP) to observe a pixel as snow given an observation that is representative of the date to be reconstructed. Differently from Gafurov et al. (2015), Dong & Menzel (2016), Chen, Wang, Guo, Xie, Wang & Hao (2020), we propose to estimate the CP in a novel way that exploits the available cloud-free multi-source HR or LR information. In detail, we calculate the probability to observe a pixel as snow given: i) the SCA computed for the cloud-free portion of the catchment, when HR acquisitions are partially cloud obscured; and ii) the LR SCF observed for the corresponding HR pixel, when HR is not acquired. In the first case, the computed CPs allow to perform a HR gap-filling and in the second one, a downscaling. We initially infer the snow presence/absence only for those pixels which show a highly persistent behaviour, i.e., CPs equal to 0 or 1. Depending on the available source of information, gap-filling and downscaling are hierarchically and iteratively applied in a framework driven by the hypothesis that HR maps are more accurate than LR maps (Salomonson & Appel 2006, Dozier & Painter 2004). Indeed, HR is used to correct possible errors in the SCF retrieval differently from other state-of-the-art methods that preserve LR SCF (e.g., Cristea et al. 2017). In this way, we generate partially reconstructed HR snow maps characterized by a high confidence. Remaining gaps in the LR SCF TS are reconstructed by means of a linear interpolation (Dozier et al. 2008). It follows that we estimate the CP for all the HR pixels and in the case they do not determine the snow presence, we reinforce the label inference through a supervised machine learning (ML) technique. In detail, we exploit a generalized additive model (GAM) trained on the CPs inferred through LR SCF, the digital terrain model (DTM) derivatives (elevation, aspect, and slope) (Schneider et al. 2021, Walters et al. 2014, Li et al. 2015, Cristea et al. 2017), the global catchment snow condition (i.e., the estimated SCA), and multi-temporal features (i.e., the observed NDSI values).

We tested the proposed approach on three hydrological seasons from October 2017 to August 2020 over a watershed in the Sierra Nevada by using HR snow maps derived by S2 and Landsat-8 (L8), and LR SCF maps derived by MODIS. The final daily HR maps have been evaluated against an independent multi-temporal dataset. It is worth noting that the approach is general and can be applied to any HR and LR sensors over any watershed.

The chapter is structured into five sections. Section 3.2 presents the procedure to infer the daily high-resolution snow cover area in mountainous regions starting from sparse multi-source optical observations. Section 3.3 illustrates the considered dataset. The obtained results are illustrated and discussed in Section 3.4. Section 3.6 draws the conclusions of the work and gives indications for further exploitation of the proposed approach.

3.2 Proposed Method

In the considered problem, we can define three spatial levels and the relative observed variables (see Fig. 3.1): i) the catchment scale and the relative SCA, ii) the LR scale and the associated SCF, and iii) the HR scale and the binary information of snow presence or absence, denoted with ω_s and ω_{sf} , respectively. The class labels can be converted to numerical values, i.e., $\omega_s = 1$ and $\omega_{sf} = 0$. The HR grid is resampled and spatially aligned within the LR grid. Both the HR and LR snow maps are screened for all the undetermined pixels (e.g., clouds, shadows, missing data), identified hereafter as ω_{nd} . As shown in Fig. 3.1, we denote with x_i the HR pixel, with $i = 0, 1, 2, \dots, N_{HR}$ and X_j the LR pixel, with $j = 0, 1, 2, \dots, N_{LR}$, where N_{HR} and N_{LR} are the total numbers of HR and LR pixels, respectively. Let M be the number of HR pixels contained in a LR cell, i.e., N_{HR}/N_{LR} . It follows that the SCF can be retrieved either i) from the LR spectral information sensor using for example the method proposed by Salomonson & Appel (2006), hereafter denoted as $SCF_{LR,j}$, or ii) by counting the pixels classified as ω_s within the LR pixel, hereafter denoted as $SCF_{HR,j}$:

$$SCF_{HR,j} = \frac{\sum_i^M x_i}{M}, \quad x_i \in X_j \text{ with } i = jM, \dots, (j+1)M - 1 \quad (3.1)$$

Note that to keep reliability, Eq. 3.1 is calculated only if the number of valid HR pixels is statistically significant (i.e., ω_{nd} pixels are less than 5% of M). Similarly, also the SCA can be computed starting either from the HR images (SCA_{HR}) or from the LR data (SCA_{LR}). When HR is partially covered by clouds and the SCA refers to the cloud-free area only, we denote it as \widetilde{SCA} .

The inputs to the method are a sparsely acquired long TS of HR snow cover maps and a quasi-daily LR TS of SCF maps relative to the period to be reconstructed, i.e., any time interval of interest up to last available acquisitions. We denote as t_η , with $\eta = 0, 1, 2, \dots, T_\eta$ a date belonging to the HR TS. The HR TS spans over a longer period than the one considered for the daily reconstruction. As output we obtain daily HR snow cover maps and daily LR SCF maps for each t_ξ , with $\xi = 0, 1, 2, \dots, T_\xi$. Note that the daily SCF retrieval is not the main objective of the work, but it is part of the reconstruction process.

As shown in Fig. 4.1, the workflow can be divided in two main blocks. The first block, namely the historical block is based on historical analyses built on observations that exploit the rich information contained in the regular repetition of the snow patterns. This allows the snow inference with very high accuracy, but returning a spatially and temporally incomplete dataset. On purpose, this first output is kept separated since its accuracy is comparable to the one of the HR multi-spectral observations, as we will see later in the result section. The historical block is repeated a second time after the temporal interpolation of SCF_{LR} . The interpolation exploits the temporal correlation of the snow cover permitting a daily reconstruction LR TS. This allows the use of the HR historical information a second time but possibly with a lower accuracy depending on the time gap (e.g., Parajka & Blöschl n.d.). Finally, the GAM block is used to spatially complete the daily TS by exploiting proxy

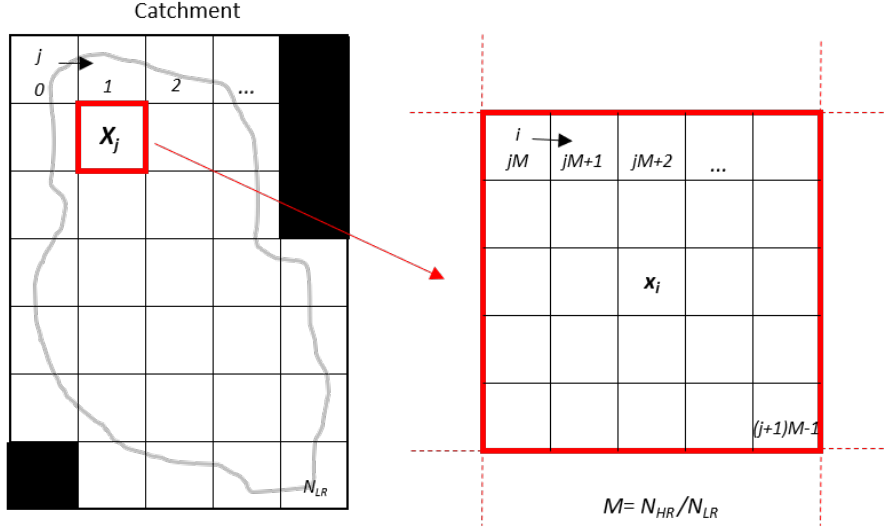


Figure 3.1: Problem definition. We consider three spatial levels: i) the catchment scale, defined by the HR and LR pixel included in the geographical area of the catchment (grey line, black pixel are masked out), for which we can calculate the SCA, i.e., the fraction of the catchment covered by snow; ii) the low-resolution scale and the associated SCF calculated for each LR pixel X_j , i.e., the fraction of a LR pixel covered by snow; and iii) the high-resolution scale, in which each HR pixel x_i is binary classified either as ω_s or ω_{sf} . Note that HR pixels are spatially resampled and aligned to fit within the LR pixel.

variables related to the accumulation and melting processes. We obtain as output two complete and coherent TS. It is worth noting that the conceptual separation of the blocks allows the final user to distinguish pixels with different confidence level depending on the final application of the snow TS (e.g., data assimilation).

As preliminary step - for sake of conciseness not included in Fig. 4.1 - we deal with the daily multiple acquisitions. In case of two HR scenes acquired on the same date, we combine them by i) filling the ω_{nd} of one acquisitions with the label from the other acquisition if not ω_{nd} ; or ii) setting to ω_{nd} pixels if the labels are conflicting. In case of two or more LR acquisitions, the $SCF_{LR,j}$ derived from the acquisition with the lowest viewing angle is considered (Riggs et al. 2015).

The method starts by considering a date t_ξ belonging to the daily TS that needs to be reconstructed. For sake of conciseness we illustrate the most complete case, when both HR and LR are acquired. If a HR map is acquired, we check if it is possible to reconstruct any pixel x_i by means of the first historical statistical analysis, i.e., the computation of the CP given \widetilde{SCA} . If yes - CPs equal to 0 or 1 - we apply the gap-filling driven by the historical HR snow pattern persistence (Gap-filling - see Section 3.2.1). The next step is the spatial correction of SCF (Correction - see Section 3.2.3) to update the $SCF_{LR,j}$ by exploiting the original or the newly introduced labels. These two steps are repeated until it is possible to reconstruct new labels. If this is not possible - CPs different from 0 or 1 - we check if a LR acquisition exists for t_ξ and we try to infer new labels by applying the downscaling driven by the LR historical snow pattern persistence (Downscaling - see Section 3.2.2). Again,

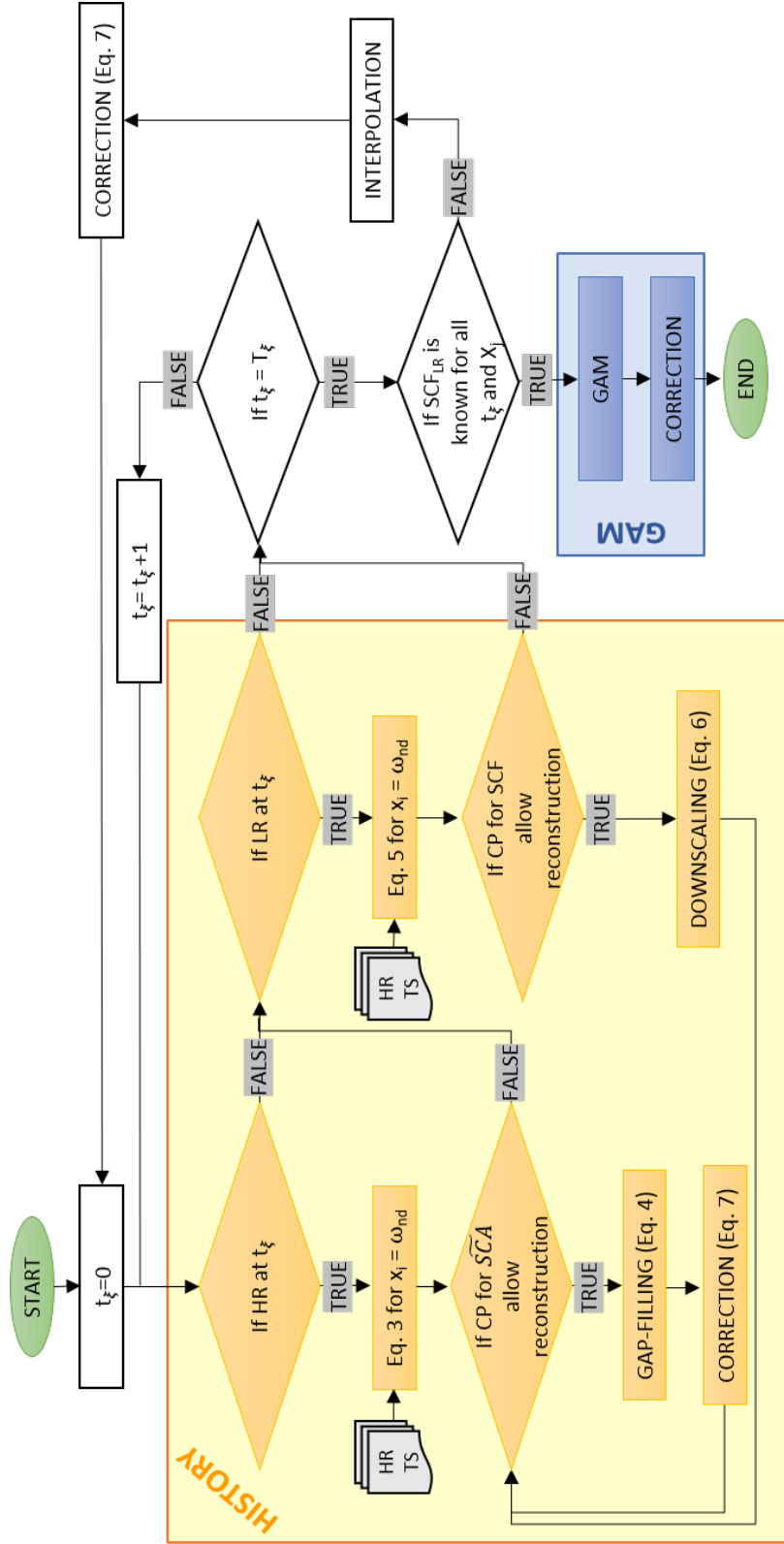


Figure 3.2: Workflow of the proposed method. It is composed by two main blocks, i.e., the historical block (gap-filling, correction and downscaling) and the GAM block (GAM and final correction). The two blocks are joined by an intermediate step composed of the interpolation and correction.

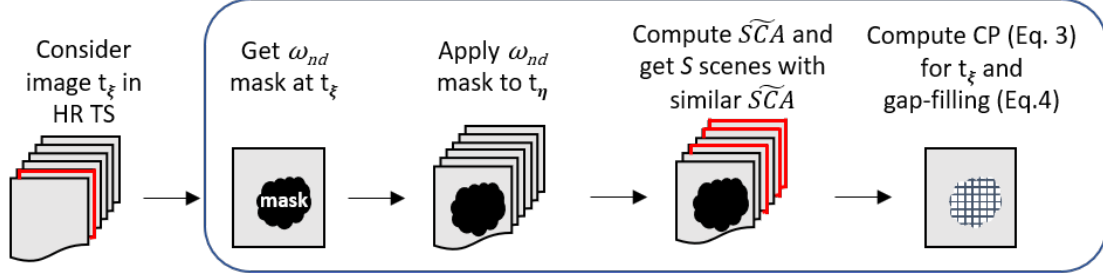


Figure 3.3: Gap-filling: historical statistical analysis to infer the snow presence conditioned by the partial SCA. First, the cloud mask of the date to be reconstructed is applied to the entire HR TS. The dates with similar \widetilde{SCA} are then used to compute the CP (Eq. 3.3) and infer the HR label (Eq. 3.4).

the newly inferred HR pixels can add information for repeating the cycle Gap-filling and Correction. This is done for all the dates in the TS. When we have completed the historical block for all the dates, we apply the temporal interpolation of SCF (Interpolation - see Section 3.2.4) to fill the gaps in the LR TS and we Correct again SCF_{LR} to ensure coherence with the valid HR pixels within any interpolated X_j . The interpolated values are used as input of a new cycle of the historical block (Downscaling, Gap-filling and Correction) for all the dates t_ξ of the TS. When no more labels can be inferred from the Downscaling, the remaining pixels are classified with the GAM based reconstruction (GAM - see Section 3.2.5), which reinforces with explicit geomorphometric, global snow cover, and multi-temporal properties the CP previously obtained by applying the Downscaling. Note that in the last step we consider the CPs included but not equal to 0 and 1. Finally, a last Correction is applied to ensure consistency between the HR and LR final outputs.

3.2.1 Gap-filling driven by the historical HR snow pattern persistence

The first step of our reconstruction method is applied when a cloud contaminated HR snow map at a given time t_ξ is available. As shown in Fig. 3.3, a long HR TS is used for computing the historical CP to observe a pixel as snow given the available partial information on snow cover at t_ξ , i.e., \widetilde{SCA}_ξ . In detail, the pixels classified as ω_{nd} at time t_ξ are used to mask each t_η belonging to the HR TS. The scenes that present \widetilde{SCA}_η similar to \widetilde{SCA}_ξ both in absolute values and spatial distribution are selected for the computation of the CP. By masking remaining cloudy pixels, a simple similarity criterion is set up for the two dates t_ξ and t_η :

$$\delta^{\xi,\eta} = \frac{\sum_{i=0}^{N_{\text{unmasked}}} |x_i^\xi - x_i^\eta|}{N_{\text{unmasked}}}, \quad i \notin \text{mask} \quad (3.2)$$

where $N_{\text{unmasked}} = f(t_\xi)$ is the number of pixels belonging to the unmasked area. The scenes are defined to be similar if $\delta^{\xi,\eta}$ is less than a threshold T_δ . Hence, by considering the resulting S similar scenes, we can infer the CP $P_i(\omega_s | \widetilde{SCA})$ to

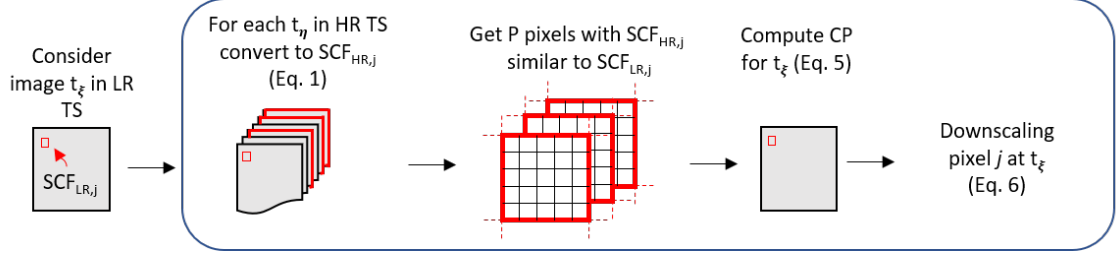


Figure 3.4: Downscaling: historical statistical analysis to infer the snow presence given the LR SCF. Given a LR acquisition on the date to be downsampled, we consider SCF_{LR} for each LR pixel X_j . We aggregate the HR TS (Eq. 3.1) and we select the P pixels which show a similar SCF for X_j . Hence we compute the CP (Eq. 3.5) and we perform the downscaling (Eq. 3.6).

observe as snow the pixel x_i belonging to the masked area for the considered date t_ξ (hereafter the index ξ is omitted for brevity):

$$P_i(\omega_s | \widetilde{SCA}) = \frac{\sum_{s=0}^S x_i^s}{S}, \quad i \in \text{mask} \quad (3.3)$$

To ensure statistical reliability, S should be greater than a certain threshold T_S . Hence, we apply the following rule:

$$\begin{aligned} x_i &= \omega_s, \text{ if } P_i(\omega_s | \widetilde{SCA}) = 1 \\ x_i &= \omega_{sf}, \text{ if } P_i(\omega_s | \widetilde{SCA}) = 0 \end{aligned} \quad (3.4)$$

3.2.2 Downscaling driven by the LR historical snow pattern persistence

This step of the method is used when the HR acquisition at time t_ξ is missing or not reconstructed from the previous step, but we know the $SCF_{LR,j}$. The estimation of the HR snow distribution is done by downscaling $SCF_{LR,j}$ to the pixels x_i included in X_j following the method firstly proposed by Premier, Marin, Notarnicola & Bruzzone (2021).

As shown in Fig. 3.4, given a LR scene acquired at the time t_ξ to be downsampled, we consider the observed SCF_{LR} for a generic pixel X_j . Hence, given an associated HR TS we compute the CP conditioned to SCF_{HR} :

$$P_i(\omega_s | SCF_{HR,j}) = \frac{\sum_{p=0}^P x_i^p}{P}, \quad x_i \in X_j \quad (3.5)$$

where P is the number of LR pixels with same SCF_{HR} . P should be greater than a certain threshold T_P to ensure statistical reliability. As for the gap-filling, we define a similarity criterion between the $SCF_{HR,j}$ values to increase the number of comparable pixels. For this reason, we quantize SCF_{HR} in k steps with a fixed size $\Delta_{SCF,HR}$. The downscaling is performed when $SCF_{HR,j}$ is not available. $SCF_{LR,j}$ is also quantized in k $\Delta_{SCF,LR}$. The use of $\Delta_{SCF,LR}$ reduces possible errors in the SCF retrieval (e.g., due to off-nadir viewing angle (Margulis et al. 2019)), since SCF_{LR}

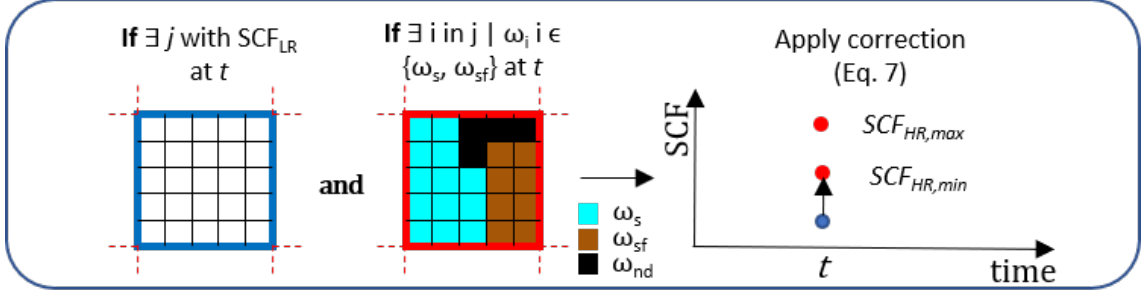


Figure 3.5: Example of spatial correction of SCF. It is applied to a $SCF_{LR,j}$ (observed or interpolated) when classified HR pixels within the considered pixel X_j are available.

differences within the considered step do not affect the downscaling. However, when SCF_{LR} assumes values close to the lower and upper limits of the belonging interval $\Delta_{SCF,LR}$, inaccuracies can still be introduced. For this reason, we introduce an additional margin ε , such that $\Delta_{SCF,HR} = \Delta_{SCF,LR} \pm \varepsilon$. For example, a $\Delta_{SCF,LR} = 10\%$ and $\varepsilon = 10\%$ implies that a SCF_{LR} which falls in the range 20-30% exploits a CP computed for an interval between 10-40%.

Finally, we infer the presence or absence of snow for the pixel x_i as follows:

$$\begin{aligned}
 x_i = \omega_s, \text{ if } & \begin{cases} P_i(\omega_s | SCF_{LR,j}) = 1 \\ SCF_{LR,j} = 1 \end{cases}, x_i \in X_j \\
 x_i = \omega_{sf}, \text{ if } & \begin{cases} P_i(\omega_s | SCF_{LR,j}) = 0 \\ SCF_{LR,j} = 0 \end{cases}, x_i \in X_j
 \end{aligned} \tag{3.6}$$

3.2.3 Spatial correction of SCF

This step aims at correcting errors in SCF_{LR} by exploiting the HR information. In particular, in the case when a part of the HR pixels included within the LR pixel are labelled as ω_s or ω_{sf} , we can derive the minimum and maximum possible values of SCF_{HR} , namely SCF_{HR}^{min} and SCF_{HR}^{max} (see Fig. 3.5). These values are calculated by assuming that the HR pixels classified as ω_{nd} would all be labelled as ω_{sf} or ω_s , respectively. Hence, for a LR pixel X_j the $SCF_{LR,j}$ should be between the minimum and maximum of $SCF_{HR,j}$, otherwise:

$$SCF_{LR,j} = \begin{cases} SCF_{HR,j}^{min} & \text{if } SCF_{LR,j} < SCF_{HR,j}^{min} \\ SCF_{HR,j}^{max} & \text{if } SCF_{LR,j} > SCF_{HR,j}^{max} \\ SCF_{HR,j} & \text{if } SCF_{HR,j}^{min} = SCF_{HR,j}^{max} = SCF_{HR,j} \end{cases} \tag{3.7}$$

Assuming that HR maps, even reconstructed, are more accurate than LR maps, Eq. 3.7 is applied to all the $SCF_{LR,j}$, no matter whether observed or temporally interpolated, and every time new HR pixels are reconstructed by the proposed method itself. This ensures consistent HR- and LR-TS outputs.

3.2.4 Temporal interpolation of SCF

This step aims at reconstructing the daily SCF_{LR} . This information is used by the proposed method to recalculate the CP and perform a new reconstruction cycle (historical block) exploiting the previous downscaling, gap-filling and correction steps. Moreover, to reconstruct all the HR pixels even for the uncertain situations without stable snow pattern persistence, the CP calculated given the SCF_{LR} (eq. 3.5) and the estimation of the SCA_{LR} for the basin are used as input to the GAM. To obtain a daily SCF_{LR} , we propose to use a temporal interpolation. Several interpolation methods to perform gap-filling have been introduced in the snow literature (e.g., López-Burgos et al. 2013, Dozier et al. 2008). For sake of simplicity, we make the assumption that the SCF variation follows a linear trend, which is reasonable especially in case of a smooth melting phase, but more complex interpolations can be used. The effectiveness of this step depends on the time gap between the observations to interpolate. For this reason, a maximum gap is generally set in the state-of-the-art snow interpolation methods (e.g., Parajka & Blöschl n.d.). In this work, we do not specify a gap limit since we want to end up with a daily TS. In order to cope with the possible errors that can be introduced by this operation, we adopted the quantization strategy described in Section 3.2.2. In this way, the downscaling is more robust when the variations of SCF are within $\Delta_{SCF,LR}$.

3.2.5 GAM based reconstruction

This step is applied to the partially reconstructed TS as final part of the proposed method. The pixels labelled as ω_{nd} in input to this step are uncertain as i) the historical analyses highlighted an instability of the snow patterns given the observed conditions; and ii) the SCF_{LR} related to the snow situation at the considered time and the relative CP may come from the temporal interpolation step described in the previous section. For this reason, we propose to reinforce the computed CP from the downscaling (Eq. 3.5) by including further proxy variables, representative of the geomorphometry, the global snow cover conditions as well as the proximal spectral properties of the considered pixels.

In detail, the components relevant to our analysis are:

- Digital Terrain Model (DTM) features that are related to geomorphometric properties of the considered pixel. In detail:
 - *Elevation*, which is strongly related to air temperature. Indeed, the elevation of the zero-degree isotherm controls the height at which the snowfall occurs, but also the melting ratio differs based on the air temperature. Accordingly, we expect a deeper and longer lasting snowpack with increasing elevation.
 - *Slope*, which is inversely correlated with the probability to have snow. Flat terrain promotes the deposition of snow meanwhile steep terrains are subjected to gravitational transport (Kerr et al. 2013). Since it is

common to have higher slope at higher elevations, slope may invert the trend of the probability to have snow above certain elevation values.

- *Aspect*, which is related to the solar radiation and hence to the energy that is potentially available for the snowmelt. Snow disappearance patterns are a consequence of spatial variation of longwave radiation (Schneider et al. 2019)
- Multi-temporal features, i.e., the closest previous and next NDSI values, which are linked to the spectral changes of a pixel related to the snow presence/absence;
- The SCA_{LR} that represents the estimated global snow cover situation over the catchment. It is available after the interpolation step;
- The CP estimated through Eq. 3.5 as feature representative of the historical information, which also includes the daily information (since they are linked to the SCF observations).

It is worth noting that other features could be added to the ones listed above, e.g., land cover type and forest density. A complex interrelationship between the topography, the land cover and the snow patterns exists. Whether the presence of forested areas strongly influences the snow deposition and melting processes, the snow patterns controlled by the topography influence in turn the spatial vegetation patterns (Tappeiner et al. 2001). However, the detection of snow under canopy is not the scope of this chapter and requires deeper investigations.

To predict the snow distribution, we train a generalized additive model (GAM). GAMs are also entitled interpretable machine learners and allow the user to directly inspect modelled relationships in detail by interpreting partial dependence plots, i.e., the trends of the smoothing functions. The interpretability of a GAM is due to its additive nature. GAMs, which generalize a logistic regression, are semi-parametric models that can be used to fit a smooth curve through observed data (Hastie & Tibshirani 1987). The probability to observe a pixel as snow can be derived as follows:

$$g(P(\omega_s)) = \alpha + f_1(x_1) + f_2(x_2) + \dots + f_Q(x_Q) \quad (3.8)$$

where x_i are Q independent features, $g()$ is the link function that relates the predictor variables to the estimated probability, α represents the intercept, and f_i , $i = 1, \dots, Q$ are non-parametric smoothing functions. The smoothing function f_i is a combination of K spline functions $b_k(x)$ weighted by coefficients β_k :

$$f_i(x) = \sum_{k=0}^K b_k(x)\beta_k \quad (3.9)$$

In a logistic GAM, the function *logit* is used as link function g . An important parameter that controls the "wiggleness" of the smoothing functions can be expressed as:

$$\text{wiggleness} = \lambda_i \int [f_i''(x)]^2 dx \quad (3.10)$$

where λ_i is the smoothing parameter relative to the feature x_i . This parameter controls the second derivative of the functions f_i , i.e., the amount of smoothness we want to impose on the model. Changing this parameter results in a change of the degrees of freedom of the GAM.

The training of the model is performed by considering multi-temporal samples collected over all the HR TS. Thus, a single GAM is used for predicting the class of the missing HR pixels for each date. This choice, compared to perform a training of the GAM for each date, has the main advantage of decreasing the computation time and allows a more direct model interpretation. However, in the complex mountain environment, an appropriate level of generalization and spatially transferable predictions have to be ensured. For this research, model parameterization and validation are based on a spatially explicit partitioning of the original dataset into five disjoint training and test regions. The implementation of such a spatial cross validation (SCV) procedure ensures the spatial transferability of the model, as well as higher independence between the training and the test dataset (Schratz et al. 2019). For this study, a grid-search over the smoothing penalties λ_i is performed for each of the five subregions (i.e., folds). Within each subregion, this parameter is tuned by means of an internal non-spatial generalized cross-validation (GCV) to select the parameters of the model for each predictor (Wood 2017). After the parameter tuning is done for a single subregion, the model is tested on the remaining ones. The best model is chosen by evaluating:

- the overall accuracy $OA = \frac{TP+TN}{TP+FP+TN+FN}$ where TP are the true positive, TN the true negative, FP the false positive and FN the false negative;
- the Brier score $BS = \frac{1}{H} \sum_{i=0}^H (p_i - o_i)^2$ where p_i is the probability of the prediction, o_i is the binary outcome that we want to predict and H is the number of training samples.

3.3 Dataset Description

To evaluate the performance of the proposed method, we applied it to the South Fork watershed in California in the Sierra Nevada. The basin has an area of about 974 km². The mean elevation of the catchment is 3067 m, ranging from a minimum elevation of 1926 m up to a maximum elevation of 4146 m. This represents a high-elevation Alpine catchment.

The inputs to the method are a long HR TS and a quasi-daily LR TS of the period to be reconstructed. We used a HR TS of 352 scenes spanning over a period of about 7 years from April 2013 to August 2020 (151 L8 and 201 S2 scenes). The raw scenes were downloaded from <https://earthexplorer.usgs.gov>. Regarding the LR scenes, we used MODIS daily data spanning three hydrological seasons from October 2017 to August 2020, i.e., in detail the MOD02HKM product downloaded from <https://ladsweb.modaps.eosdis.nasa.gov>.

The completely cloud covered images were removed after a visual inspection. Thus, all the optical data were pre-processed to obtain calibrated Top of the Atmosphere

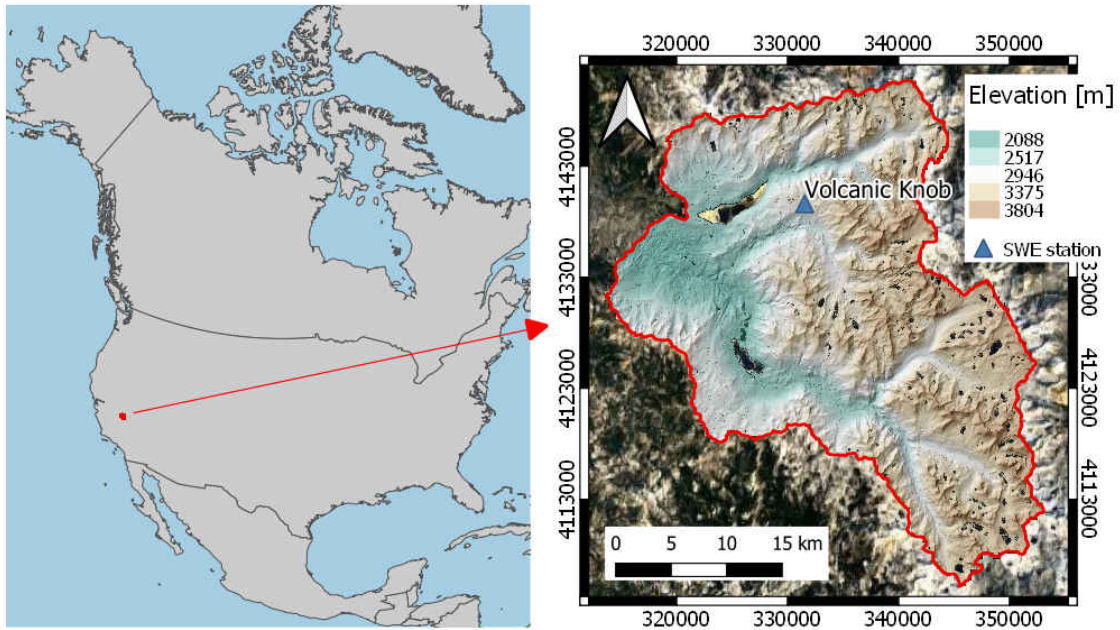


Figure 3.6: Overview of the study area: a catchment located in the Sierra Nevada, California. The DTM is represented on the right.

(ToA) reflectance values. All the bands were then re-projected, resampled and co-registered to a consistent grid at a resolution of 25 m for HR and 500 m for LR. The cloud mask is obtained for both HR and LR scenes by using an active learning procedure based on a support vector machine (SVM) classifier (Tuia et al. 2016). This allows to faster converge to the definition of the training set and to obtain accurate classification results. We set up an interactive procedure by asking the user either if the result is satisfactory or if the classification needs to be improved. The classification of the HR scenes was done considering all the spectral bands acquired by the sensors excluded the bands at 60 m for S2 (bands 1, 9 and 10) and the panchromatic, cirrus and one of the thermal bands (bands 8, 9 and 11) for L8. Regarding LR, we excluded band 5, which is corrupted due to a detection failure. In all cases we added the normalized vegetation index (NDVI), NDSI, and the difference between the infrared and the SWIR bands, which have shown to introduce benefits in the classification. Snow classification was done by using the algorithm proposed by Dozier & Painter (2004) for HR, resulting in a binary map, and the method proposed by Salomonson & Appel (2006) for LR, which results in a map with SCF values ranging from 0 to 100%.

Regarding the GAM approach, we used the python package *pyGAM* for the implementation of the model (Servén & Brummitt 2018). Particular attention was devoted to the multi-temporal training of the GAM. We selected around 1000 random samples from a set of around 150 HR scenes, whose cloud coverage was less than 2%. Remaining cloudy pixels were excluded from the training set. We obtain a total training set of around 150000 samples.

Two independent datasets have been used for the validation. We considered nine cloud-free HR data - three for each hydrological season - each made up of around 1.5 million pixels to be used for comparison with the obtained results. Moreover, we used an independent dataset made of five 3 m resolution snow depth maps, measured by the Airborne Snow Observatory (ASO), a coupled imaging spectrometer and scanning lidar system developed at NASA/JPL (Painter 2018). To convert these data to binary data with 25 m resolution, we resampled them by computing the weighted averaging of all contributing pixels and we applied a threshold to the snow depth classifying as ω_s those pixels whose snow depth is at least 0.08 m and as ω_{sf} the remaining pixels. The threshold is selected according to the literature (Notarnicola 2020, Zhang et al. 2019) and the sensitivity of the ASO Painter et al. (2016). Furthermore, the performance of the two blocks, but the interpolation step, several experiments were carried out. By considering the most cloud-free scenes in our result evaluation, we did not investigate in detail the interpolation, since interpolation techniques and temporal filters have been largely investigated in literature.

3.4 Experimental Results

In this Section we present and discuss the results. In detail, we assess the performance achieved by the historical block of the proposed method (gap-filling and downscaling). Thus, we assess the performance of the GAM block that provides complete output maps.

We summarize the parameters used in the historical block of the workflow as shown in Table 3.1. The choice arises from the experimental sensitivity analyses carried out in the next sections to understand the best trade-off between accuracy and the amount of reconstruction. Note that these parameters are easily interpretable and adaptable to other datasets as required by the user.

3.4.1 Results of the Gap-filling

An example of application of the gap-filling is shown in Fig. 3.7. The reference presents a snow coverage of 100%. We apply an artificial cloud mask to elevations between 2800 e 3300 m (see Fig. 3.7b). The observed partial snow cover is highly informative and allows to infer the 79% of the cloud covered pixels. In the remaining cloudy pixels, the historical analysis highlights variability of the snow patterns that does not allow to determine the correct class. As it is possible to observe in the CP map (see Fig. 3.7c), most of the pixels present a CP equal or close to 1. This may indicate the presence of classification errors in the historical analysis. Hence, the use of a less restrictive criterion on the CP thresholding could be applied in this case.

To assess quantitatively the performance of this step, we set up a general test by considering 30 representative scenes with a cloud coverage less than 0.05% and SCA spanning from 0 to 100%. We applied to each of the 30 cloud free scenes nine different cloud masks with cloud percentage of 20, 30, 40, 50, 60, 70, 80, and 90%. The cloud masks are randomly selected by the TS, to represent real situations. We

Table 3.1: Values of the parameters used in the historical block selected through the experimental sensitivity analysis.

Step	Parameter	Value	Description
Gap-filling	T_δ	15%	Threshold on the similarity $\delta^{\xi,\eta}$ for HR maps (see Eq. 3.2).
	T_S	10	Threshold on the minimum number of HR scenes S considered for the CP computation (see Eq. 3.3).
Downscaling	T_P	10	Threshold on the minimum number of LR pixels P considered for the CP computation (see Eq. 3.5).
	$\Delta_{SCF_{LR}}$	10%	SCF quantization step for LR.
	ε	10%	Margin such that $\Delta_{SCF_{HR}} = \Delta_{SCF_{LR}} \pm \varepsilon$.

computed the CP (Eq. 3.3) for four different T_δ thresholds, i.e., 5-10-15-20%. T_S is fixed to 10 after the sensitivity analysis. For brevity and for similarity with the results obtained for T_P (see Sec. 3.4.2), the analysis is not reported in the chapter.

Fig. 3.8 shows the obtained OA versus different cloud cover percentages. The results are accurate and stable for the different thresholds T_δ , with an OA higher than 99.8%. This confirms that this step should be applied as first in our workflow. What varies is the percentage of the reconstructed pixels, which increases by increasing T_δ from 5 to 15% and decreases for 20%. Choosing a small value of T_δ implies a more selective criterion. Thus, it is possible that the minimum number T_S of required scenes with similar \widehat{SCA} is not satisfied. This explains the increasing number of reconstructed pixels by increasing the similarity threshold T_δ . Moreover, when the threshold becomes too big, the inverse trend is explained by the increasing variability encountered, i.e., a larger number of analyzed scenes and thus less pixels with CP equal to 0 and 1. In our experiment, $T_\delta = 15\%$ returns the best result being a good trade-off between statistical reliability and \widehat{SCA} variability.

However, it is worth stressing the fact that the results depend on the cloud position and the partial observed snow cover. Let us consider the artificial example of Fig. 3.9, where a cloud mask is applied to elevations lower than 2800 m. In

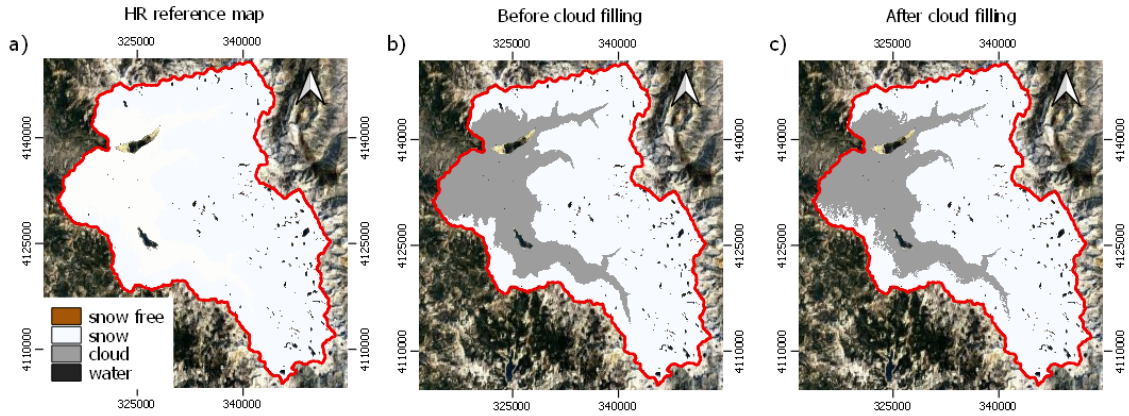


Figure 3.7: Example of the application of the gap-filling step to infer the snow presence conditioned by the partial cloud-free SCA: (a) reference image, (b) artificial cloud mask before the cloud filling procedure applied to elevations between 2800 e 3300 m, (c) conditional probability map, and (d) results after the gap-filling procedure.

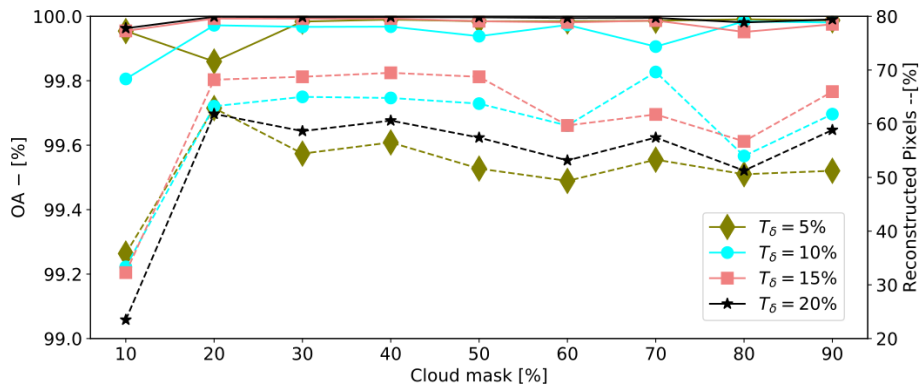


Figure 3.8: Performances achieved by the gap-filling step. The plot shows the overall accuracy (OA) (solid lines -) and the reconstructed pixels (dashed lines - -) for variable cloud masks and variable T_δ thresholds. The percentage of the reconstructed pixels is calculated w.r.t. the cloud covered area. $T_\delta = 10$ is used.

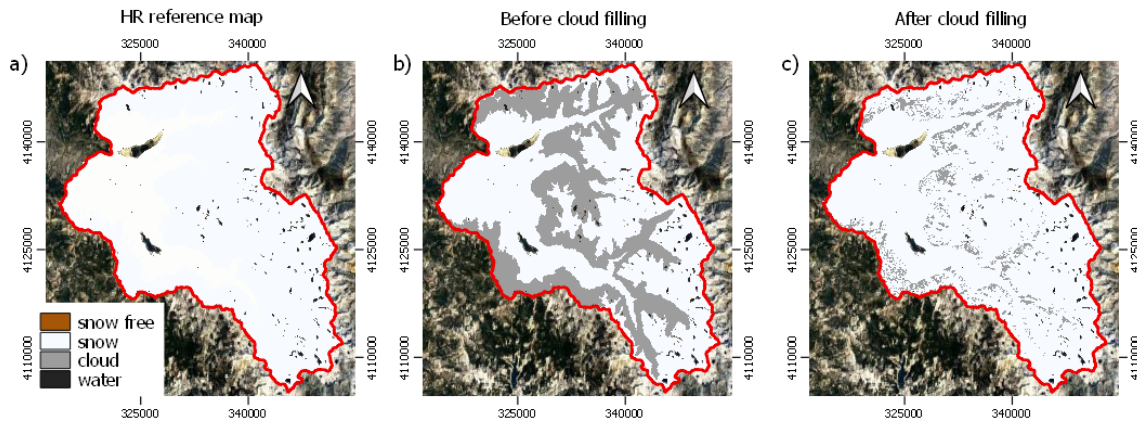


Figure 3.9: Example of the application of the gap-filling step to infer the snow presence conditioned by the partial cloud-free SCA: (a) reference image, (b) artificial cloud mask before the cloud filling procedure applied to elevations lower than 2800 m, (c) conditional probability map, and (d) results after the gap-filling procedure.

this case, the gap-filling allows the reconstruction of only 4% of the total cloud area (see Fig. 3.9a). Indeed, the analysis of the historical time series does not lead to a reconstruction as shown in Fig. 3.9c. The high variability in the CP values means that the considered \widetilde{SCA} can be observed both for completely snow covered catchment as well as for a partial coverage. However, a method based on the snow line altitude (e.g., Gafurov & Bárdossy 2009, Da Ronco & De Michele 2014, Parajka et al. 2010) would have failed to reconstruct even those pixels.

3.4.2 Results of the Downscaling

In Fig. 3.10 we present an example to illustrate how the downscaling approach works. In details, on the left the SCF_{LR} map that is used as input to the downscaling is shown. The computed CPs are shown in the center. Only the pixels with CP equal to 0 or 1 are directly replaced with the class ω_{sf} or ω_s , respectively. The resulting map is shown on the right. We downscale the 62% of the image. It is interesting to note that the remaining unlabelled pixels are located mostly on melting areas as for example intermediate elevations. It is possible to recognize similarities between the snow patterns and the geomorphometry (see Fig. 3.7c). Also in this case a less restrictive criterion on the CP thresholding could be applied to increase the number of reconstructed pixels.

To better assess the performance of the downscaling, we analyze a LR TS composed of 956 scenes acquired from October 2017 to August 2020. We split the TS in four groups, depending on the scan angle θ (considered here as a mean value over the scene, given the small variations inside the area of the catchment), to test how much the off-nadir view affects the SCF detection (Dozier et al. 2008). In fact, for whiskbroom scanning spectrometers with large swath, such as MODIS, pixels near the edge of the swath present severe distortions i.e., the so-called “bow-tie effect” (Sayer et al. 2015). To test the performance, we consider those LR scenes acquired

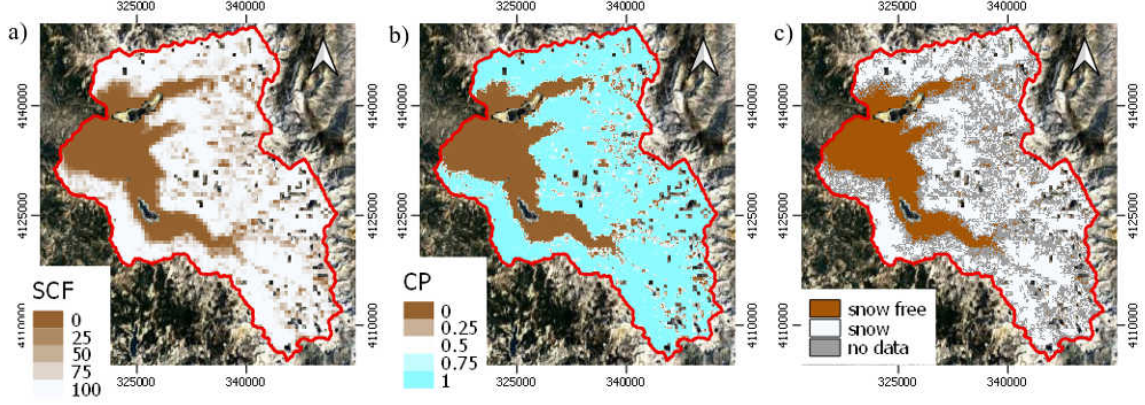


Figure 3.10: Example of the application of the proposed reconstruction step to downscale the SCF: (a) SCF map to be downscaled, (b) conditional probability map, and (c) map downscaled with the proposed method.

at the same time of a HR scene that is need as reference (see Table 3.2).

Table 3.2: Overview of the scenes considered for the evaluation of the downscaling step considering the different acquisition scanning angles.

Scan Angle	Total LR scenes	HR Reference
$\theta \leq 20$	171	30
$20 < \theta \leq 40$	248	44
$40 < \theta \leq 50$	206	34
$\theta > 50$	331	97

Hence, we compute the OA of the partially reconstructed scenes w.r.t. the original HR scenes and the percentage of reconstructed pixels for different scan angles. We select the best parameters among several possible combinations. However, for illustration purposes we present only the results by fixing two of the thresholds and varying the other one. In details, the results are reported in Figure 3.11 versus: a) different $\Delta_{SCF,HR}$ considering regular steps equal to 5-10-20-33.3-50-100%, with $T_P = 10$ and $\varepsilon = 0\%$, b) different T_P (0-5-10-15-20) with fixed $\Delta_{SCF,HR} = 10\%$ and $\varepsilon = 0\%$ (i.e., $\Delta_{SCF,HR} = \Delta_{SCF,LR}$), and c) different ε 0-2-5-10-15-20% with $\Delta_{SCF,HR} = 10\%$ and $T_P = 10$. Note that the percentage of reconstructed pixels is calculate w.r.t. the pixels which can be potentially reconstructed, i.e., the total pixels do not consider those having cloudy LR (no SCF to perform the reconstruction) and HR clouds (no reference pixel to compute the accuracy).

In general, we can notice a decreasing OA with increasing scan angle. Nonetheless, the performances of the proposed downscaling approach justify the use of MODIS scenes even for large scanning angles since we can benefit of an observation as guide for the reconstruction.

In detail, Fig. 3.11a shows that OA initially decreases with an increasing $\Delta_{SCF,HR}$ for all the scan angles, except for $\Delta_{SCF,HR} = 100\%$. This value represents a special

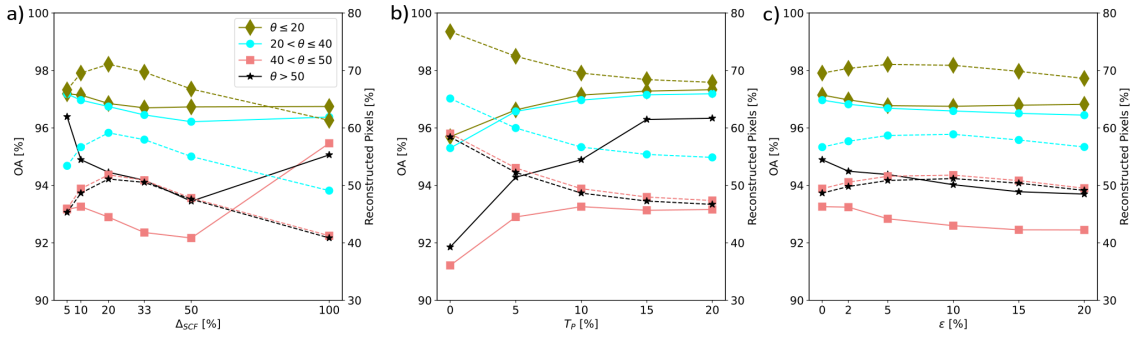


Figure 3.11: Sensitivity analysis for the downscaling step. OA (solid line –) and the percentage of reconstructed pixels (dashed line - -) for: (a) different discretization steps $\Delta_{SCF,HR}$, (b) different threshold values T_P for the number of considered pixels, and (c) different buffer size ε for the CP computation (see Eq. 3.5). The trends are shown for different scan angles θ .

case, i.e., pixels reconstructed by directly replacing SCF_{LR} equal to 0 or 100% (see Eq. 3.6). Indeed, CPs are never 0 or 1 for $\Delta_{SCF,HR} = 100\%$ (i.e., no pixels are always classified as ω_s or ω_{sf}). The results show that the accuracy obtained for these specific pixels is comparable with the proper downscaling.

By analyzing the first part of the plot, we can deduce that slight variations of OA versus $\Delta_{SCF,HR}$ are due to the trade-off between representativeness and variability. A lower $\Delta_{SCF,HR}$ implies a smaller number of pixels with that specific SCF. Due to the threshold T_P to ensure statistical reliability, for very small $\Delta_{SCF,HR}$ we are reconstructing only few pixels but with a good precision, if the observed SCF is correct. On the other hand, the variability encountered decreases and we can fill in more gaps. The higher $\Delta_{SCF,HR}$, the higher the variability, and this is the reason why we are reconstructing less pixels even though T_P is increasing. Thus we have decreasing OA by increasing $\Delta_{SCF,HR}$. The choice of the best $\Delta_{SC,HRF}$ results from a trade-off between OA and reconstructed pixels. Setting $\Delta_{SCF,HR} = 10\%$ results as a good trade-off maximizing the reconstructed pixels without significant losses of OA.

Fig. 3.11b, which shows the results for different thresholds T_P , points out that 10 is a good trade-off between OA and the number of reconstructed pixels.

As last parameter we tested ε , which also plays a role on the representativeness and variability, as shown in Fig. 3.11c. The greater ε , the greater the number of occurrences, the greater the variability and hence the number of pixels with CP between 0 and 1. We use $\varepsilon = 10\%$, since the performances are very similar to $\varepsilon = 5\%$ but we increase the statistical reliability of the method.

However, we can notice that a slightly different choice of these parameters does not strongly affect the final results, since we can see in the figures that they are quite stable and the method always returns high accuracies.

To understand the main source of errors of the downscaling step, Fig. 3.12 shows the trend of OA over time for the LR dataset with $\theta \leq 20$ together with the root

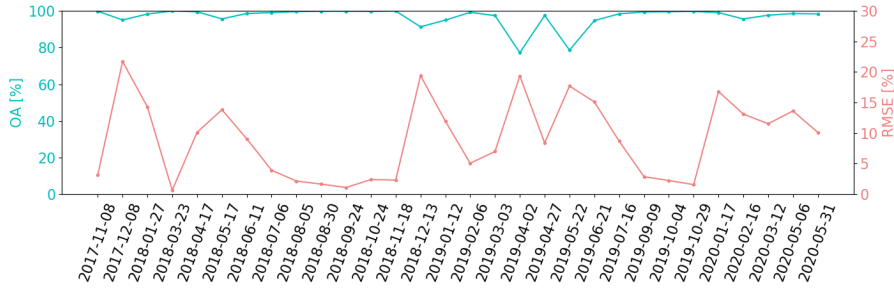


Figure 3.12: Overall accuracy (OA) of the proposed downscaling and SCF_{LR} RMSE trends for the LR dataset with $\theta \leq 20$. RMSE is calculated between SCF_{LR} and SCF_{HR} . $\Delta_{SCF,HR} = 10\%$, $T_P = 10$ and $\varepsilon = 10\%$ are chosen.

means square error (RMSE) of the retrieved SCF_{LR} and SCF_{HR} . As one can notice, high RMSE is associated with low OA of the downscaling, confirming that errors present in the SCF_{LR} are propagated by the method. These errors are introduced in the SCF due to the application of a global retrieval method that does not count for variations in grain size, solar zenith angle, viewing angle, and atmospheric effects (Salomonson & Appel 2006). For these reasons, the use of $\Delta_{SCF,LR}$ introduces the benefit that retrieval errors of SCF_{LR} do not affect the downscaling when these are within $\Delta_{SCF,LR}$. Moreover, this explains the need to progressively correct the SCF values with HR observed or reconstructed pixels.

3.4.3 Results of the GAM

We present in this section the results not only in terms of performance of the step, but also in terms of variable behaviour. In fact, the relationship between the features list in Section 3.2.5 and the target variable can be analyzed by plotting the partial dependence functions. We expect a linear increasing trend of the probability to observe ω_s both with SCA_{LR} and the CP. For this reason and to ensure model generalization, we forced these features to be represented by a linear term instead of a combination of spline functions. The importance of the CP is very high and it can be understood by looking at the effect that the feature has on the predicted outcome (see Fig. 3.13). Regarding the other features there is an increasing probability to have snow by increasing elevation. With slope we observe instead an inverse correlation, since steep terrains are more subjected to gravitational transport. For the aspect variable, we split its contribute in two features: the "northness", i.e., the cosine of the aspect, and the "eastness", i.e., the sine of the aspect. We observe a stable trend, meaning that the aspect is irrelevant for the prediction. This can happen when other variables already explain part of the associated data variability of a feature. As expected, the geomorphometric features are embedded in the CP and they loose relevance when this feature is added to the model. The NDSI trends appear plausible, showing higher probability in case of higher indices.

Table 3.3 reports the smoothing parameters used in the implementation. These

parameters are chosen after computing the SCV by evaluating different metrics and result in an OA of 97.83% and a BS of 0.0034.

Table 3.3: Smoothing parameters used for the GAM reconstruction.

Parameter	Value	Feature	Term
λ_1	5659.72	f_1 =SCA	Linear
λ_2	8514.25	f_2 =elevation	Spline (20 splines, order=3)
λ_3	3650.07	f_3 =slope	Spline (20 splines, order=3)
λ_4	5464.47	f_4 =northness	Spline (20 splines, order=3)
λ_5	2325.85	f_5 =eastness	Spline (20 splines, order=3)
λ_6	3627.94	f_5 =NDSI $_{t-1}$	Spline (20 splines, order=3)
λ_7	5170.45	f_7 =NDSI $_{t+1}$	Spline (20 splines, order=3)
λ_8	1.04	f_8 =CP	Linear

Let us now analyze the performances of three slightly different reconstruction approaches for 20 dates almost cloud-free with variable SCA. The three reconstructions applied here are: i) standalone history, i.e., reconstruction with the historical block (gap-filling - downscaling - correction) and application of a threshold (0.5) to the CP resulting from the downscaling step to decide whether the label of a pixel should be ω_s or ω_{sf} ; ii) standalone GAM, i.e., reconstruction fully completed by the GAM trained on the CP resulting from the historical block, but the labels of those pixels with CP=0 or CP=1 are not directly replaced; iii) the proposed method, i.e., the pixels with CP=0 or CP=1 are replaced with the corresponding labels, while the remaining pixels are reconstructed by the GAM. We have for these dates both HR and LR acquisitions. Remaining unlabelled pixels are not considered in the validation scheme. These 20 dates are also excluded by the training set for the GAM,

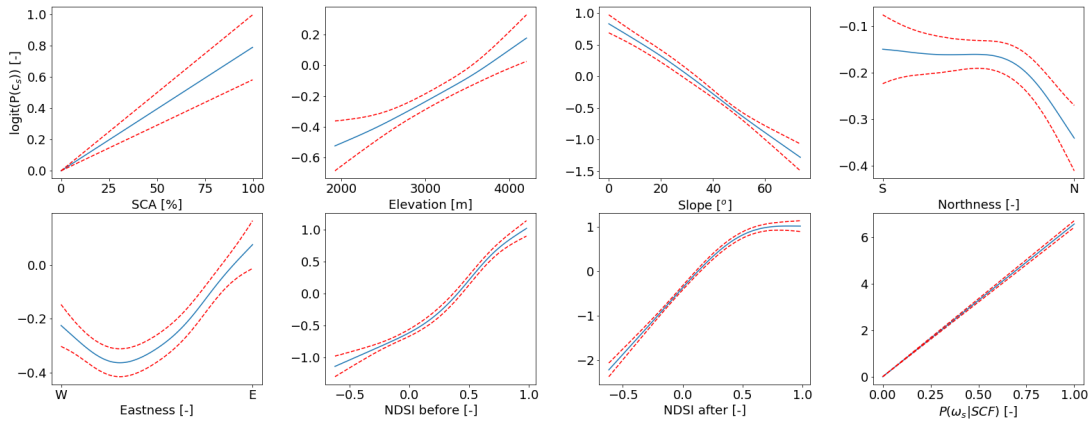


Figure 3.13: Partial dependence plots for the features used for the GAM model, i.e., elevation, slope and aspect. The blue continuous lines represent the smoothing functions and the red dashed lines represent the 95% confidence intervals. The y-axes have been fixed to the scale of the CP ($P(\omega_s|SCF)$) which is the feature that shows the largest predicted outcome.

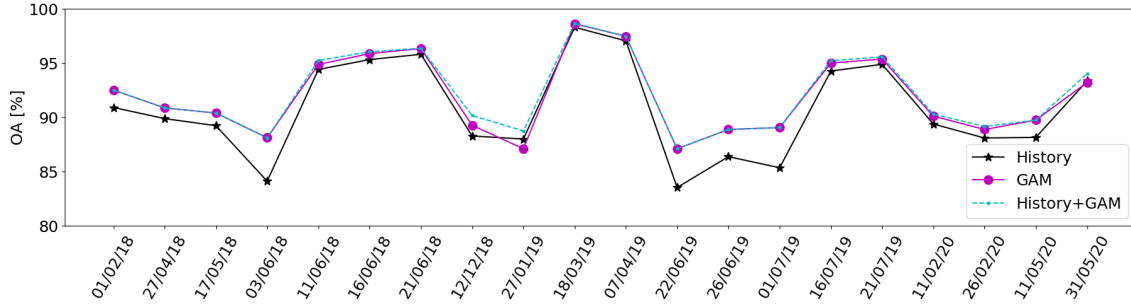


Figure 3.14: Performances achieved by three considered reconstruction approaches: i) standalone history, i.e., reconstruction with the historical block and application of a threshold (0.5) to the CP; ii) standalone GAM, i.e., GAM trained on all the CPs resulting from the historical block (also when equal to 0 or 1) without direct reconstruction in the historical block; iii) the proposed method, i.e., reconstruction with the historical block and, later, with GAM.

to ensure an independent validation set. This test also serves as evaluation of the GAM performances. The results are presented in Fig. 3.14. We achieve for the three tested methods a mean OA of 90.74, 91.94 and 92.19%, respectively.

What is clear from the plot is that the history is highly informative. Indeed, the accuracy achieved by the standalone history is getting in the worst case an OA of 84%. The proposed method, that exploits also explicit auxiliary features in addition to the history, is improving the results of about 1.5%. Interestingly, the application of the standalone GAM is producing results with comparable accuracy. This result also confirm that the GAM is driven by the CP being the historical patterns the most important information, no matter if it is kept separated or it is embedded in a ML method. However, when using the standalone GAM, it is not possible to explicitly separate the two-level outputs that present different reliability, as we will see in detail in the next section. Indeed, keeping these two blocks separated allows the user to easily identify which pixels are subjected to the highest uncertainty and therefore, to select the most suitable output depending on the final application.

3.4.4 Results of the Full Proposed Method

We present here the results by applying the proposed daily HR reconstruction framework to three complete hydrological seasons spanning from the 1st of October 2017 to the 31st of August 2020. We selected among the most cloud-free scenes, nine HR images acquired at three different days. These dates are used to evaluate the final results and are not used as input to the proposed method. Furthermore we tested five dates against an independent validation dataset (see Table 3.4 and Fig. 3.15). The validation against the HR images resulted in an average OA of 96.97% after applying the historical block (note that SCF_{LR} is observed and not interpolated for these specific dates) with a mean reconstruction percentage of 75.52%. After the completion of the workflow, i.e., after the GAM, the method shows an OA of 92.26% with all the pixels reconstructed. Similarly, we get an OA of 94.90% when

evaluating against the ASO dataset for the historical block, with 85.36% of pixels reconstructed and a final OA of 92.27%.

Table 3.4: Results in terms of OA [%], confusion matrix (CM) and reconstructed pixels obtained by the different blocks of the proposed method on nine dates (three for each hydrological season) evaluated against selected HR scene and five dates evaluated against the ASO dataset. The CM reports the TP, FP, TN and FN (clockwise from the upper left), normalized by row.

		Historical Block				GAM Block		
		Date	OA [%]	CM [%]	REC [%]	OA [%]	CM [%]	
HR reference	12.01.18	91.90	90.29 1.36	9.71 98.64	79.62	89.23	88.95 9.83	11.05 90.17
	17.05.18	95.47	91.11 0.63	8.89 99.37	75.90	90.26	84.29 3.65	15.71 96.35
	11.06.18	98.62	93.51 1.09	6.49 98.91	82.68	94.90	86.48 3.75	13.52 96.25
	17.04.19	98.83	99.55 9.19	0.45 90.81	85.21	95.14	99.08 31.91	0.92 68.09
	11.06.19	95.09	94.17 3.38	5.83 96.62	74.98	90.17	92.07 12.95	7.93 87.05
	11.07.19	98.27	94.62 1.34	5.38 98.66	79.97	93.98	87.27 4.50	12.73 95.50
	01.02.20	98.57	99.25 10.39	0.75 89.61	63.94	91.83	96.41 32.01	3.59 67.99
	23.05.20	97.26	93.01 0.64	6.99 99.36	56.79	90.54	85.15 5.18	14.85 94.82
	08.06.20	98.77	89.12 1.00	10.88 99.00	80.57	94.27	79.75 3.83	20.25 96.17
ASO reference	23.04.18	95.14	97.29 10.52	2.71 89.48	81.56	89.49	96.38 26.38	3.62 73.62
	01.06.18	91.47	96.69 10.81	3.31 89.19	100.00	91.47	96.69 10.81	3.31 89.19
	17.03.19	98.05	98.13 22.93	1.87 77.07	68.96	94.47	95.20 36.45	4.80 63.55
	02.05.19	94.97	98.72 19.67	1.28 80.33	100.00	94.97	98.72 19.67	1.28 80.33
	14.07.19	94.85	96.68 5.24	3.32 94.76	76.27	90.96	94.61 9.67	5.39 90.33

It has to be taken into account that two dates of the ASO acquisition, i.e., the 1st of June 2018 and 2nd of May 2019, are acquired in correspondence of a HR acquisition. We keep on purpose the HR scenes in the workflow, so the reconstruction is not performed for those scenes. What we can see is that the performances of the method are similar to the OA computed for the HR scenes, showing that i) HR images are accurate but they can still be affected by small errors, and ii) the assumption made in the workflow that the output of the historical block can be considered reliable is fulfilled.

Fig. 3.15 presents the false-color composition (R:SWIR,G:NIR,B:RED), and the

results in terms of true positive (TP), true negative (TN), false positive (FP) and false negative (FN) before the GAM (partially reconstructed HR scene) and after the GAM. The OA is higher than 97% for the reconstruction performed before the GAM. It decreases after the application of the GAM, but it is still around 92% in the worst case. The errors introduced after the GAM are mainly located on the ridges of the mountains, which are erroneously classified as ω_s . Other errors are located in the transition zones, where the melting occurs (see for example 11/07/2019, orange spots highlighting FN). These are errors due to the lack of information about the local snow situation (both in time and space). In other words, as expected, the historical, the time-proximal and the geomorphometric information are not enough to describe snow distribution processes that are mainly related to specific meteorological conditions.

It is interesting to observe that in average we start with around 17% of labelled HR pixels. After the historical block the average number is around 61%, meaning that the presence of LR data together with the gap-filling procedure allows the reconstruction of more than half of the TS but there are still consistent gaps. After the interpolation, the second repetition of the historical block results in the 83% of reconstructed pixels and consequently, a relative small percentage is assigned to the GAM. Finally, of course, after the GAM 100% of the pixels are labelled.

Fig. 3.16 compares the reconstructed daily SCA trends derived by the proposed framework and the ones derived using only the observations from the HR and LR TS. We represent the partial SCA as well as the amount of clouds. Furthermore, we present the snow water equivalent (SWE) measured at the station Volcanic Knob (see Fig. 3.6). The SWE observations (see Fig. 3.16c-f-i) are useful to understand when the main snowfalls occurred, even though a perfect temporal correspondence cannot be found since the station is located at a lower quote than the average altitude of the basin. As we can see in the plots a-d-g of the Fig. 3.16, the temporal resolution of the HR TS is not suited for a proper monitoring of the SCA. The presence of large gaps would not lead to a complete SCA reconstruction even by applying the state-of-the-art methods as a multi-temporal filter. On the other hand, the LR TS (see Fig. 3.16b-e-h) better captures the SCA variations but still suffers from cloud obstruction that strongly limits its usability. If the sampling time is not appropriate for catching quick events of snow-falling and melting, the interpolation could lead to wrong results. Nonetheless, the reconstructed TS introduces the big advantage of a higher spatial detail.

The technique was run on a 2.6 GHz CPU without parallelization with 30 GB RAM. The analyzed catchment in Sierra Nevada made up of 1860x1580 pixels, with a total number of 1516262 pixels that are not masked (e.g., lakes are masked). The total running time was about 4.5 hours for each analyzed hydrological season. The approach can be scaled on bigger catchments by applying it in parallel to all the sub-catchments.

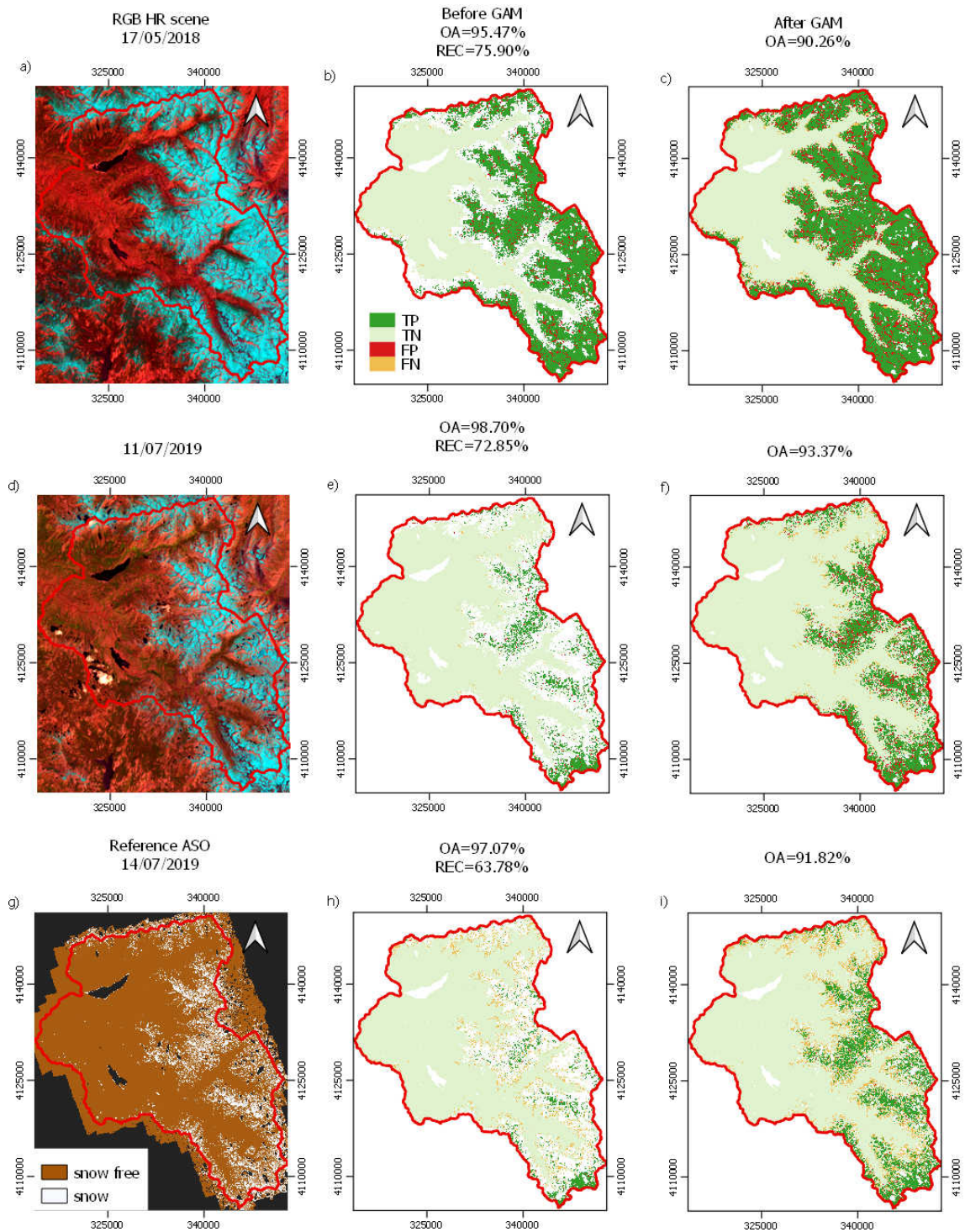


Figure 3.15: False color composition (R:SWIR,G:NIR,B:RED) (a-d) and reference map (g) for three reconstructed dates. Results before (b-e-h) and after applying the GAM (c-f-i) in terms of overall accuracy (OA) and reconstructed pixels (REC). True positive (TP) in dark green, true negative (TN) in light green, false positive (FP) in red, false negative (FN) in orange, and no data in white.

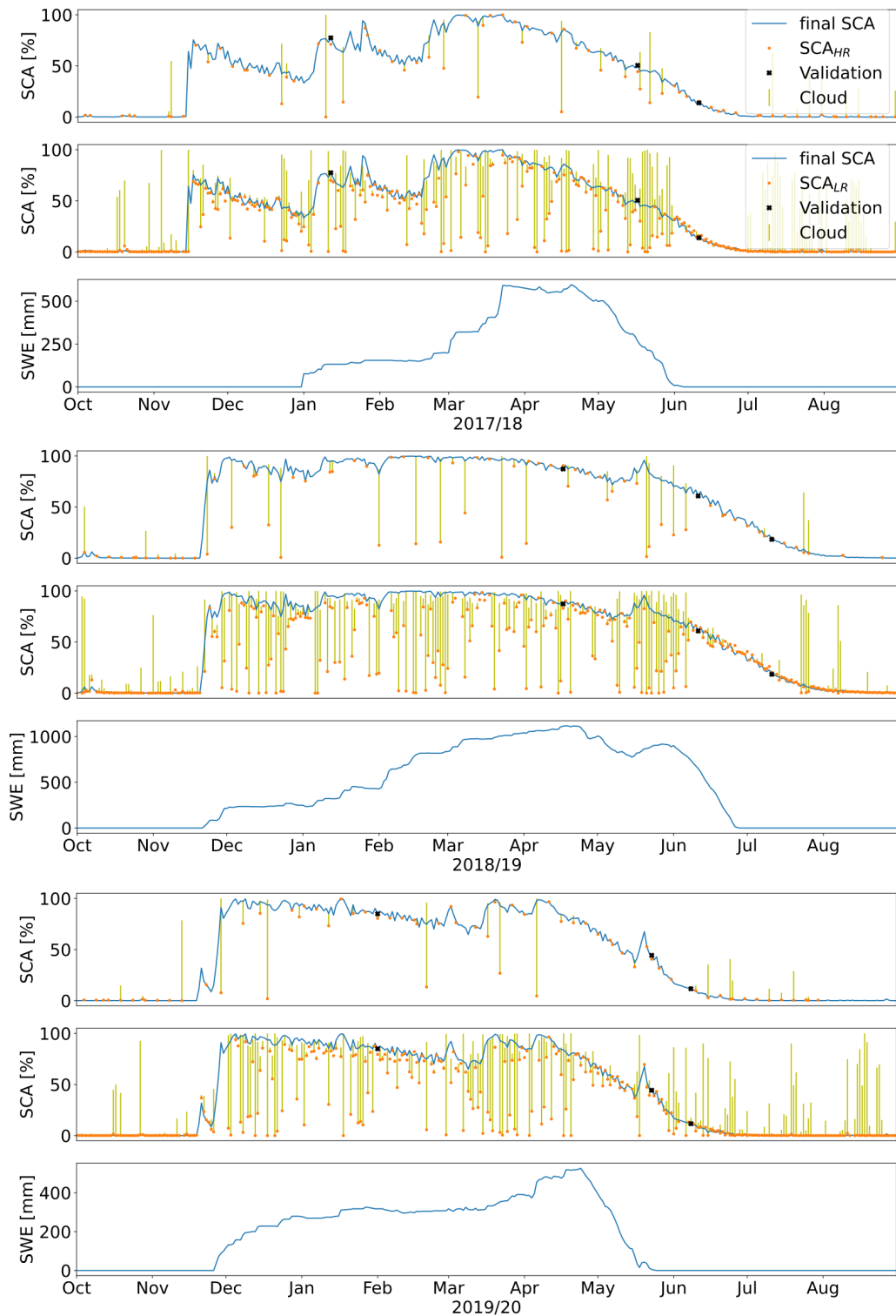


Figure 3.16: SCA trends and measured SWE at the Volcanic Knob station for the hydrological seasons 2017-18 (a-b-c), 2018-19 (d-e-f) and 2019-20 (g-h-i). The reconstructed SCA is compared with the SCA observations from the HR (a-d-g) and LR acquisitions (b-e-h), with relative SCA (orange dots) and cloud percentage (vertical olive line). The validation dates are also indicated with a black x.

3.5 Discussion

In this section we discuss the main outcomes of the presented method.

A main point of interest of the proposed method is its division in two main blocks. The first block, namely the historical block (gap-filling, downscaling and correction) aims at extracting the snow patterns by deriving the CP to observe a pixel as snow given an observation that is representative of the date to be reconstructed. As we have shown in the results, it allows to obtain high accuracy but the reconstructed TS still contains gaps. For this reason, the reconstruction performed through the historical block is particularly suited for users that need very accurate results but not necessarily at a daily base, e.g., for data assimilation. This historical block is repeated a second time after the SCF is temporally interpolated. By exploiting the temporal correlation of the snow cover, this step allows to obtain a daily SCF TS with an accuracy that depends at the first instance on the duration of the gap. Finally, we obtain a daily HR TS by applying the second block, namely the GAM block, that makes use of proxy variables related to the accumulation and melting processes to infer the snow condition. The complete output is designed for users who need a daily reconstruction, or for catchments that are affected by cloud obstruction only for limited periods. The daily TS has shown to be still an accurate product.

Interestingly, we have seen that the exploitation of the history directly in the GAM block returns similar results. This is due to the high importance of the CP used as feature in input to the classifier. However, differently from the proposed method the use of the standalone GAM requires dedicated strategy to allow the separation of the results in terms of uncertainty.

A specific sensitivity analysis has been carried out for the parameters used in the historical block. We have seen that a different choice of these parameters does not strongly affect the final results. Moreover, they can intuitively be modified accordingly to the user needs.

We discussed the sources of errors, finding that the erroneous SCF values retrieved from the LR data is the most critical one. Another important limiting factor is represented by the cloud duration that could negatively affect the results of the interpolation step. The proposed method tries to cope with this sources of error by considering quantized SCF steps rather than the exact value. Furthermore, our approach relies more on the HR information trying to correct possible errors introduced by the SCF retrieval.

The resulted SCA of the basin represented a very informative and accurate information with higher temporal and spatial coverage than the original HR dataset. We have presented the final SCA trends for three hydrological seasons, highlighting that the raw input TS would have not been appropriate for hydrological purposes, data assimilation in physically-based models or model evaluation. The produced daily HR TS has shown to be able to capture snowfalls and melting periods when

qualitatively compared with the observations of a weather station. Hence, the output of this method represents an important asset for further applications.

The CPs have been used to define the pixels that show similar response under certain conditions, i.e., with CP equal to 0 or 1, and the pixels subjected to variable conditions, i.e., with CP included between 0 and 1. The first could be further exploited for other applications. For example, the design of the hydrological response units (HRU) could benefit of these information. The latter suffers of weak information to determine the reconstruction, as in transition zones where changes are happening as accumulation or melting. Interestingly, they also represent the most important points to monitor and the knowledge of the areas that show the highest variability can be relevant for planning a strategic network of meteorological stations. In case auxiliary meteorological observations cannot be collected, a data assimilation scheme should be exploited: from one side, the high-quality observations provided by the proposed method can improve the model, and from the other side, the model could provide important information in the most uncertain areas. Therefore, we believe that this work can be a starting point for further integrations between meteorological/hydrological models and RS.

3.6 Conclusion

In this work we have presented a method to infer the daily snow cover at high spatial resolution at a catchment scale. It exploits the physically based concept that we can observe some systematic patterns in the snow cover distribution, which are regularly repeating as they are related to the geomorphometry and the meteorology of the considered area. The proposed approach is based on a hierarchical structure that exploits all available daily sources of information, starting from the HR snow cover if available. It takes as input classified snow cover maps (binary classification for HR and SCF for LR) and processed data in five different steps: i) gap-filling, based on a historical statistical analysis conditioned by the historical HR snow pattern persistence, ii) downscaling, based on a historical statistical analysis conditioned by the LR historical snow pattern persistence, iii) spatial correction of SCF, iv) temporal interpolation of SCF, and v) GAM based snow reconstruction.

We tested the proposed approach on three hydrological seasons from October 2017 to August 2020 over a watershed in the Sierra Nevada by using HR snow maps derived by S2 and L8, as well as LR SCF maps derived by MODIS. The final daily HR maps have been evaluated against an independent multi-temporal dataset, showing an OA around 97% for the historical block with a percentage of reconstructed pixels around 76% and an OA around 92% after the GAM block. Hence, the partial outputs after the historical block present accuracy similar to the maps classified by means of the multi-spectral information.

Acknowledgements

This work was supported by the European Space Agency (ESA) under the Alpine Regional Initiative AlpSnow EXPRO+ Contract No. 4000132770/20/I-NB.

We also would like to thank the NASA Airborne Snow Observatory (ASO) for providing free-of-charge data.

Chapter 4

Exploring the Use of Multi-source High-Resolution Satellite Data for Snow Water Equivalent Reconstruction over Mountainous Catchments

Seasonal snow accumulation and release are so crucial for the hydrological cycle to the point that mountains have been claimed as the "water towers" of the world. A key variable in this sense is the snow water equivalent (SWE). However, the complex accumulation and snow redistribution processes render its quantification and prediction very challenging. In this chapter¹, we explore the use of multi-source data to reconstruct SWE at a high spatial resolution (HR) of 25 m by proposing a novel approach designed for mountainous catchments. To this purpose, we exploit i) daily HR time-series of snow cover area (SCA) derived by high- and low-resolution optical images to define the days of snow presence, ii) a degree-day model driven by in-situ temperature to determine the potential melting, and iii) in-situ snow depth and Synthetic Aperture Radar (SAR) images to determine the state of the catchment (i.e., accumulation or ablation) that is needed to add or remove SWE to the reconstruction. Given the typical high spatial heterogeneity of snow in mountainous areas, HR data sample more adequately its distribution thus resulting in a highly detailed spatialized information that represents an important novelty. The proposed SWE reconstruction approach also foresees a novel SCA time-series regularization from impossible transitions, i.e. the change of the pixel class from snow to snow-free when it is supposed to be subjected to an accumulation event or, the other way round, the change from snow-free to snow during a melting event. Moreover it reconstructs SWE for all the hydrological season without the need of spatialized precipitation information as input, that is usually affected by uncertainty. Despite the

¹This chapter has been submitted in:

Premier, V., Marin, C., Bertoldi, G., Barella, R., Notarnicola, C. Bruzzone, L. (2022), 'Exploring the Use of Multi-source High-Resolution Satellite Data for Snow Water Equivalent Reconstruction over Mountainous Catchments', *The Cryosphere*

simple approach based on a set of empirical assumptions, it shows good performances when tested in two different catchments: the South Fork catchment, California, and the Schnals catchment, Italy, showing a good agreement with an average bias of -40 mm when evaluated against a HR spatialized reference product and of 38 mm when evaluated against manual measurements. The main sources of error introduced by each step of the method have been finally discussed to provide insights about the applicability and future improvements of the method that may be of great interest for several hydrological and ecological applications.

4.1 Introduction

Seasonal snow accumulation and melting are of crucial importance for the hydrological cycle and the total water supply. Especially in mountainous areas, the snow has such a large impact on the local hydrology that mountains have been claimed to be “the water towers of the world” (Immerzeel et al. 2020). For example, in the Alps the snowmelt contribution to the streamflow ranges from at least 50% of the total flow to sometimes over 95% (Viviroli et al. 2003). Hence, it is essential to estimate the amount of water stored during the winter not only for river discharge forecasting but also for a correct planning of human activities such as agriculture irrigation, drinking water supply and hydropower production (Beniston et al. 2018, DeWalle & Rango 2008b). However, especially in mountain regions, snow distribution is highly variable in space due to redistribution processes (Balk & Elder 2000) and precipitation observations are often affected by large errors due to orographic effects (Prein & Gobiet 2017). This also limits the spatial accuracy of snow accumulation and melt models (Engel et al. 2017, Günther et al. 2019). In this context, given the difficulty to dispose of spatialized and continuous observations especially in remote areas (Rees 2005), remote sensing (RS) has shown to be a valuable tool for snow hydrology, .

A spatial characterization of the snow properties requires both information about the extent of the snow cover, i.e., the snow cover area (SCA), and appropriate snowpack information. A key variable is the snow water equivalent (SWE), i.e., the total amount of water stored in the snowpack that would be released upon complete melting. While a long list of methods for SCA detection that exploit multi-spectral optical satellites is available in the literature (see Dietz et al. (2012) for a review), we do not have operational methods to directly map SWE with high spatial resolution (HR). Direct SWE observations are limited to point measurements through manual sampling, snow scales or snow pillows (Archer & Stewart 1995, Meløysund et al. 2007), or with a limited spatial footprint (~ 500 m) as cosmic-ray neutron probes (Schattan et al. 2019). Spatialized snow depth (HS) information can be provided by differential lidar altimetry (Painter et al. 2016) or stereo photogrammetry (Deschamps-Berger et al. 2020). Currently, these methods can be applied only to limited areas and with a low temporal sampling. Moreover, to derive SWE from HS additional a priori information is needed to infer the snow density (Helfricht et al. 2018). Physically-based snow models represent a valid alternative (e.g., Lehning et al. 2006, Vionnet et al. 2012, Endrizzi et al. 2014) that can provide HR SWE

information on large areas. However, their accuracy is strongly limited by the availability of meteorological observations and by the gravitational and wind-induced snow redistribution processes (Jost et al. 2007, Mott et al. 2018).

Active and passive microwave sensors can potentially provide information about the snowpack. In particular, passive microwave sensors have been used to retrieve long time-series of SWE by exploiting the correlation between the brightness temperature and the SWE (Pulliainen et al. 2020). However, the observations are limited by a poor spatial resolution (i.e., 25 km) and mountain areas are excluded. The use of active microwave sensors such as Synthetic Aperture Radars (SAR) has also been investigated for the HR retrieval of SWE (Shi et al. 1994, Baghdadi et al. 1997, Ulaby et al. 1981, Rott et al. 2010) and differential SWE (Guneriussen et al. 2001, Leinss et al. 2015). Despite the better spatial resolution also active microwave sensors suffer for the complexity of non-linear effects introduced on the total backscattering, such as snow layering, surface roughness, snow density, grain type and size which in turn are all affected by the complex snow metamorphism and change in time. Moreover, all these techniques work only in dry conditions while the scarce penetration of the electromagnetic signal in wet conditions is invalidating their applicability in monitoring the SWE evolution during the melting season. Several review articles are available for more details about SWE retrieval using SAR acquisitions (e.g., Tsang et al. 2021).

Even though SAR is still far from providing unambiguous information on SWE for all situations, it represents a promising tool to monitor the melting phases of the snowpack, i.e., the moistening, ripening and runoff phases or in other words, the presence of liquid water inside the snowpack and its evolution (Marin et al. 2020). If combined with optical data, the runoff onset, i.e., the time when SWE reaches its maximum, does add value to the well known concept of the snow depletion curves (SDC). SDC are functions that describe the relationship between SCA and HS or SWE (Cline et al. 1998). Thus, time-series of SCA maps can be used to provide an indirect measurement of SWE (Yang et al. 2022). Indeed, SWE is a function of the duration of the snow cover, which intrinsically considers the energy exchanges responsible of the melting process (Durand et al. 2008). For example, a shallow snowpack and high melt rates are associated with a SDC with high derivative while a deep snowpack and low melt rates are characterized by a longer curve. Consequently, spatial accumulation and melt variability, which are linked to the geomorphology of the study area (Anderton et al. 2002), result in different snowpack persistence (Luce et al. 1998). Therefore, by knowing the SDC and the maximum of SWE at the end of the accumulation for an area or an entire catchment, it is possible to derive the evolution of SWE during the melting. This intuitive idea opens the possibility to assimilate SCA and SDC into physically based snow models to correct the SWE evolution and improve the simulations (Arsenault & Houser 2018).

In fact, another way to exploit the SDC for SWE estimation is the combination with distributed snowmelt models to reconstruct SWE time-series in re-analysis (Martinec & Rango 1981, Molotch & Margulis 2008, Rittger et al. 2016). Differently from the methods that require to know the precipitations and the meteorological forces that redistribute the snowpack during the accumulation, SWE reconstruc-

tion builds the SWE time-series backward from the last day of snow presence up to the peak of accumulation by exploiting the estimation of the potential melt energy and the knowledge about the presence of snow cover, simplifying in this way the problem. SWE reconstruction approaches show good performances over large basin and even mountain ranges, outperforming the accuracy provided by snow models or spatial interpolation approaches of in-situ SWE measurements (Bair et al. 2016). Nevertheless, the accuracy of the results depends on a robust estimation of both the SCA and the melt energy. For this purpose, several methods have been proposed for the computation of the potential melt energy that range from a simple yet robust degree day (DD) model (Martinec & Rango 1981) to a complete radiation energy computation that takes into account also the snow albedo (Bair et al. 2016). These models generally consider a calibration factor that balances out the possible inaccuracies providing accurate results. Furthermore, the derivation of the HR SCA is hampered by the cloud presence (e.g., Premier, Marin, Steger, Notarnicola & Bruzzone 2021). In this regards the works presented in the literature exploited only low-resolution (LR) images since the large swath allows a high repetition time, i.e., with daily or sub-daily acquisitions, mitigating in this way cloud obstruction. However, the LR images are not providing the spatial details, in the Shannon sense, that allow a proper sampling of the snow cover evolution in the mountains, which is in the order of few dozen of meters. Moreover, the use of LR sensors results in a non-linear combination of the different contributions of the elements within the pixel and this should be properly taken into account by the snow classification approaches to avoid large errors especially in complex terrains. On the other hand, the use of HR snow maps introduces important benefits both in SWE determination as well as in streamflow forecasting (Li, Lettenmaier, Margulis & Andreadis 2019). With the introduction of the Copernicus Sentinel-2 (S2) mission, the HR images are made available free of charge with a temporal resolution at the equator of 5 days. This opens new opportunities to monitor the heterogeneous snow conditions in the mountains. However, due to the cloud coverage, the useful acquisitions are reduced by 50% in the Alps (Parajka & Blöschl 2006). Thus, even if the Landsat images are exploited together with the S2 images, only few acquisitions are available per month. In this sense, data assimilation of remote sensing products in models may represents an added value (e.g., Margulis et al. 2016). Recently we proposed an approach to the reconstruction of daily HR snow cover maps. The approach performs a gap-filling and a downscaling of snow cover fraction (SCF) maps derived at LR based on the idea that melting and accumulation patterns are repeating inter-annually (Premier, Marin, Steger, Notarnicola & Bruzzone 2021, Revuelto et al. 2021). Therefore, by observing partial HR or LR acquisitions it is possible to reconstruct a daily HR snow cover.

In this chapter we explore multi-source satellite data to reconstruct HR SWE for a given catchment. The approach exploits: i) daily HR snow cover time-series derived by fusion of high- and low-resolution optical sensors to determine the dates of snow appearance and disappearance, ii) potential melting derived by in-situ temperature observations with a degree day (DD) model, iii) in-situ SD/SWE observations to determine the *accumulation* state, and iv) SAR information to determine the *ab-*

lation state. In detail, the method starts with the determination of the catchment state, i.e. *accumulation* (SWE increase) or *ablation* (SWE decrease). According to the state, that is assumed to be homogeneous for all the pixels of the catchment, we regularize the HR SCA time-series from impossible transitions to correctly estimate the dates of snow appearance and disappearance for each pixel. This simplification assumption is a consequence of technological limitations in spatializing this information. The state information is needed together with the potential melting to reconstruct the daily HR SWE maps with a resolution of 25 m by adding or removing SWE according to the catchment state. Note that the reconstruction also includes the accumulation phase without the need of spatialized precipitation data as input, which are often unreliable over complex terrains. The main novelties of the proposed approach are: i) the generation of daily HR SWE maps, ii) the regularization of the daily HR SCA time-series from impossible transitions, and iii) the precipitation independent SWE reconstruction. The approach has been validated in two catchments: i) the South Fork catchment, located in the Sierra Nevada - California (USA), and ii) the Schnals catchment, located in the Alps - South Tyrol, Italy.

The chapter is structured into five sections. Sec. 4.2 presents the different steps of the proposed approach to reconstruct daily HR SWE. The two test sites and the used dataset are presented in Sec. 4.3. The obtained results are illustrated in Sec. 4.4. A detailed discussion on the approach advantages and limitations and on the results follows in Sec. 4.5. Finally, Sec. 4.6 draws the conclusions of the work and gives indications for further exploitation of the proposed approach.

4.2 Proposed approach to HR SWE reconstruction

In this section, the proposed approach to HR SWE reconstruction will be presented. The approach is made up of three main parts: i) the identification of the catchment state, ii) the characterization of the snow season from the regularized SCA time-series, and iii) the SWE calculation. The details will be illustrated in the three next subsections. As depicted in Fig. 4.1, the method initially determines the state of the catchment (see Sec. 4.2.1). This allows to properly reconstruct SWE in case of solid precipitations after the peak of accumulation and also to redistribute the total amount of SWE calculated for the melting in the accumulation period. Both cases are generally omitted in state-of-the-art SWE reconstruction methods (e.g., Molotch & Margulis 2008, Martinec & Rango 1981). Moreover, the catchment state information is used to regularize the time-series of SCA from impossible transitions and to correctly determine the beginning and end of the season (see Sec. 4.2.2). Finally, from the potential melting and the regularized time-series of SCA the proposed approach reconstructs the daily HR SWE maps (see Sec. 4.2.3).

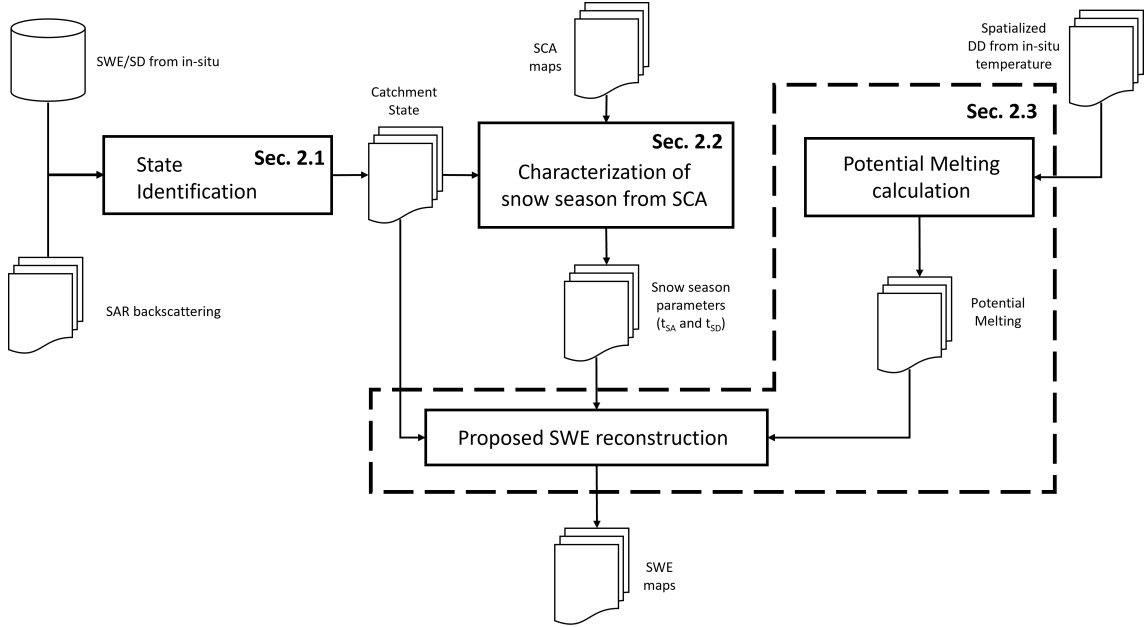


Figure 4.1: Workflow of the proposed approach showing the three main steps: i) state identification, ii) characterization of snow season from SCA, and iii) SWE reconstruction. The inputs are: i) a HR SCA time-series and daily spatialized DD maps derived from AWS, ii) SAR backscattering time-series, and iii) SWE or HS from automatic weather stations (AWS). As output, we obtain the daily HR SWE maps.

4.2.1 Identification of the catchment state

The proposed reconstruction approach is designed for a hydrological catchment that is subjected to similar weather forcings and consequently to similar accumulation and ablation events i.e., the catchment is not too vast. If we take this assumption strictly, we can define three *states* that describe the three possible SWE changes, i.e., ΔSWE between two times $t-1$ and t . These states are *accumulation* ($\Delta\text{SWE} > 0$), *ablation* ($\Delta\text{SWE} < 0$) and *equilibrium* ($\Delta\text{SWE} = 0$), as shown in Fig. 4.2. The identification of the state is necessary in the proposed approach to decide whether SWE is added or removed for the reconstruction (see Sec. 4.2.3). In detail, the catchment state does not only characterize the change in terms of SWE but also in terms of SCA, if observable, as described as follows:

- *Accumulation* when the total $\Delta\text{SWE} > 0$ due to a snowfall. We can either observe i) a positive ΔSCA , if the snow covers the bare ground, or ii) $\Delta\text{SCA} = 0$, if the snowfall happens at higher elevation than the actual snowline. However, ΔSCA is never negative and consequently a single pixel can not turn from *snow* to *snow-free* from $t-1$ to t . So, depending on the extent of the snowfall, the spatial SWE increment can interest the total snow covered area or a part of the catchment. It is usually a rapid event - one to a couple of days (Thorp & Scott 1982).
- *Ablation* when the total $\Delta\text{SWE} < 0$ due to any kind of energy exchanges (as increasing temperature, solar radiation, or rain-on-snow). We can either

observe a negative ΔSCA , if the snowpack is completely melted out and shows the bare ground, or $\Delta SCA = 0$, if the melting is only affecting the snow depth. However, ΔSCA is never positive and a pixel can not turn from *snow-free* to *snow* from $t - 1$ to t . So, depending on the amount of energy and on the depth of the snowpack, the spatial SWE decrement can interest the total SCA or a part of the catchment. It can be a long period, especially in the last phase of the season.

- *Equilibrium* when $\Delta SWE = 0$. This is the case of a steady state, i.e., no changes within the catchment, or redistribution due to wind or gravitational transport, e.g., avalanches. This last condition does not affect the overall SWE balance that remains constant, even though we can have local deposition and erosion looking at a pixel scale. In terms of ΔSCA , these changes are mainly increments of *snow-free* pixels, hence a pixel can not turn from *snow-free* to *snow* from $t - 1$ to t . In fact, we expect that snow moves from exposed areas - that can become *snow-free* - to sheltered areas - that were already covered by snow, due to the terrain properties that facilitate snow deposition.

To determine the catchment state according to the aforementioned definitions, it is clear that ΔSCA is ambiguous and consequently we need to estimate if SWE is increasing, decreasing or is constant. This information can be retrieved by a network of automatic weather station (AWS) that provide continuous information about the occurrence and elevation of snowfall events, e.g., direct SWE measurements or indirect precipitation/HS measurements. While continuous SWE measurements are hardly available, by mean of pluviometers and temperature observations it is possible to split precipitation between liquid and solid (Mair et al. 2013) and identify the catchment state accordingly, but with the limitation that they are rarely installed at high elevations. HS sensors are more suitable for our purpose but their observations are often affected by wind and gravitational transport leading to deposition/removal that may be falsely interpreted as *accumulation/ablation*. Hence, even if the AWS are generally situated in locations undisturbed from the wind action, it is more convenient to dispose of a large number of AWS that need to be screened to exclude possible sensor errors or wind/gravitational redistribution. For these reasons, the SWE/HS increment should be greater than a certain threshold that is fixed at 2 cm for HS according to values found in literature (Engel et al. 2017), resulting in a value of 2 mm for SWE when considering the typical density of fresh snow (100 kg/m³).

Nevertheless, the general scarce availability of distributed measurements inside a given catchment render the localization of the accumulation and ablation events very challenging and therefore the definition of the catchment state prone to error. Multi-temporal SAR observations have shown to be of great potentiality and to be able to detect the presence of a melted snowpack as explained by Marin et al. (2020). In this work the relationship between the SAR backscattering and the three melting phases have been investigated. It has been shown that when the backscattering is interested by a decrease of at least 2 dB, the snowpack is assumed to get moisted (Nagler & Rott 2000). The minimum of the backscattering corresponds instead with the maximum of SWE. After that moment, the snowpack starts to release water and













Event description at catchment level	t-1	t	ΔSWE	State
<i>Snow on bare ground</i> Wide snowfall that involves lower elevation belts			>0	Accumulation
	$\Delta SCA > 0$			
<i>Snow on snow</i> Confined snowfall that involves high elevation belts			>0	Accumulation
	$\Delta SCA = 0$			
<i>Snowpack melting</i> Energy exchange that leads to the heating of the snowpack and to a reduction of the snow height			<0	Ablation
	$\Delta SCA = 0$			
<i>Aereal ablation</i> Snowpack melting that leads to the complete disappearance of snow			<0	Ablation
	$\Delta SCA < 0$			
<i>Steady state</i> No changes within the catchment			=0	Equilibrium
	$\Delta SCA = 0$			
<i>Redistribution</i> Wind or gravitational transport			=0	Equilibrium
	$\Delta SCA < 0$			

Figure 4.2: Definition of the three possible catchment states: *accumulation*, *ablation* and *equilibrium*. The description of the possible events that characterize the catchment between two consecutive dates is reported together with the difference in terms of SWE and SCA. As one can notice only ΔSWE can be used to unambiguously identify the three states. The illustrations represent the SCA in an idealized catchment where white and brown areas are the *snow* and *snow-free* areas, respectively and the dashed lines represent the contour lines.

enters in the so-called runoff phase. This moment represents the most important contribution to the water release and can be provided in a HR spazialized manner, i.e., marking the dates of *ablation* for each pixel.

On the other hand, at the best of our knowledge there are no remotely sensed data that can be exploited to identify the snowfalls in a spatialized HR manner and that can be used to identify the *accumulation* at the level of each single pixel. In the majority of the situations, only one AWS located at a given high point of the catchment (which is a common configuration for snow monitoring) would be informative enough to identify all the accumulation events, but this may introduce errors in particular cases of mixed conditions. For example, it is possible to observe snowfalls at high elevations, rain-on-snow at low elevations that cause snowmelt and even steady state conditions for mid altitude belts. A correct characterization of such a situation requires to consider different areas with different states separately, which for the moment is out of the scope of the chapter. We will discuss the limitations and possible future steps to improve this aspect in Sec. 4.5.1.

In summary we propose a hybrid approach to identify the state by satisfying the following necessary conditions in order of priority: i) *accumulation* when the AWS show an increment greater than a defined threshold, ii) *ablation* when the SAR backscattering presents a relevant drop (and not *accumulation*), and iii) *equilibrium* otherwise. In this way, even though the *accumulation* does not allow to correctly spatialize the snowfalls, a spatialized information on the *ablation* allows to distinguish among pixels that are really subjected to melting and pixels that do not experience any change. In other words, a coexistent *ablation* and *equilibrium* is possible. Finally, it is worth to mention that mixed situations within the same day and for the same area are also possible given diurnal fluctuations in the meteorological forces. However in this work, we do not consider sub-daily variations but only changes that are sampled in the temporal resolution of the exploited HR SCA time-series, i.e., one day.

4.2.2 Characterization of the snow season from regularized SCA time-series

A HR SCA is an input needed for the proposed SWE retrieval, as it is used to estimate the date of snow appearance t_{SA} and disappearance t_{SD} . As mentioned in the Introduction, such a product is not available directly from remotely sensed images due to limitations in the revisit time and cloud contamination. Therefore, there is the need to reconstruct a daily HR SCA. Among the several methods present in literature, we used the approach proposed by Premier, Marin, Steger, Notarnicola & Bruzzone (2021), which merges the information coming from a sparse long HR time-series and a continuous daily LR time-series acquired in the period of interest. Gap-filling and downscaling steps are performed by applying a set of hierarchical rules based on historical analyses and geomorphometrical features. The main idea behind the approach is that snow patterns are persistent over time and follow a regular distribution that is strongly dependent on the geomorphology and meteorology of the area of interest (Mendoza et al. 2020). We refer the reader to Premier, Marin,

Steger, Notarnicola & Bruzzone (2021) for the details.

Despite the generally accurate results of the above-mentioned approach, the output HR SCA is still affected by possible inconsistencies. Errors may arise either from the classification algorithm applied to the multi-spectral input images or from the reconstruction approach. By applying the approach presented in Premier, Marin, Steger, Notarnicola & Bruzzone (2021), we can highlight the presence of two main sources of errors: i) an underestimation of snow presence in forested areas when the snow falls below the canopy and is not visible anymore from the satellite point of view, i.e., snow on ground, and ii) the missed identification of snow-patches at the end of the season. The first error source is due to the fact that the classification methods used for snow retrieval for both HR and LR data rely only on the spectral information measured inside the resolution cell of the sensor without a dedicated module for inferring the presence of snow if hidden by the canopy. This affects the detection of snow on ground particularly for HR images since the small resolution cell is likely to contain a majority fraction of canopy especially over very dense forests. This problem is instead mitigated for LR pixels that are likely to contain not only forested areas but also open fields where the snow is visible, increasing in this way the possibility to detect the snow presence. Hence, in the daily time-series of SCA, a discontinuity that happens mainly when HR images are acquired, can be identified as a local decrease of SCA. The second error involves mostly LR images whose spatial detail is not enough to detect mixed pixels with low SCF. It is an error that persists over time since LR acquisitions are more frequent than HR acquisitions. In other words, in both cases *snow-free* pixels may be falsely detected, i.e., false negative (FN) errors. *Snow* pixels can also be falsely detected i.e., a false positive (FP) errors due mainly to possible residual misclassified clouds that are identified as *snow* - this is usually an error isolated in time. All these errors are detectable by looking at the class transitions in the time-series of each pixel: the snow presence is not smooth in time. This results in an erroneous SWE determination that is strongly related to the persistence of the snow, requiring a regularized time-series.

A helpful information to regularize the SCA is the state of the catchment that is daily identified by following the rules described in the previous subsection. If the snow cover maps are coherent with the state, it follows that: i) if *accumulation*, all the pixels can only turn from *snow-free* to *snow* or maintain their label, and ii) if *ablation* or *equilibrium*, all the pixels can only turn from *snow* to *snow-free* or maintain their label. Since *ablation* and *equilibrium* imply the same rule as explained also in Sec. 4.2.1, we will refer more generally to *ablation* only. In other words, t_{SA} and t_{SD} may vary for each pixel but for sake of coherence they must coincide with an *accumulation* and an *ablation* date, respectively. Pixels that do not respect these rules are potential mistakes that need to be corrected. When we face with an erroneous class transition, we do not know a priori if the correct label is the one at $t - 1$ or the one at t . To understand what is the correct solution, we consider an appropriate time window and compute the most frequent label for it according to a majority rule. The time window is chosen in a different way in the

case that we are facing with a recent or an old date of snow appearance t_{SA} . In detail, for a given pixel, we consider:

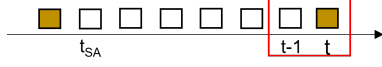
- a *recent date of snow appearance* when $t - t_{SA} < 10$ days. We observe in this period FN mostly due to missed detection of snow under canopy especially by HR sensors. In this condition, we do not expect fast changes since temperatures are low and thus the potential melting is low (see Eq. 4.1). Accordingly, we propose to consider a daily time window of ± 5 days from t to check what is the most persistent label of the considered pixel (Parajka & Blöschl 2006);
- an *old date of snow appearance* when $t - t_{SA} > 10$ days. If the final melting has already started, changes may be quick and the most common situation is the missed detection of mixed pixels as snow patches. We observe that in this period HR sensors detect snow patches that are completely omitted by LR sensors. In this case: i) the dates after t are not informative since the snow patches are disappearing quickly, and ii) daily SCA may not be informative when it is derived by LR. For this reason, we consider only the last up-to-5 dates when a HR was originally acquired in a time window between t_{SA} and t .

Once we have determined the state and whether if we are handling with a recent or an old t_{SA} , we can compute the most frequent label in the considered time window and apply the following correction (see Algorithm 1).

The correction is performed by advancing forward in time, i.e. we assume that previous labels are always coherent with previous states. The correction itself cannot introduce inconsistencies. In case we are in *accumulation*, a transition from *snow* to *snow-free* is not allowed. If the pixel is labelled as *snow* at $t - 1$, it means that for sake of coherence it turned to *snow* at t_{SA} . We also know the date of the last ablation after t_{SA} , i.e., t_{lastAB} with $t_{SA} \leq t_{lastAB} \leq t - 1$. Hence, we compute the most frequent label accordingly with the majority rules described in the previous paragraph which vary depending if the snowfall is old or recent. If it results that i) t is a false negative (FN), we can simply set it as *snow*; ii) $t - 1$ is a false positive (FP), we need to replace all times starting from the day of the last ablation state (or t_{SA} , in case the last ablation precedes t_{SA}) until $t - 1$ with *snow-free*, since the transition *snow* to *snow-free* can happen during ablation only.

Analogously, the transition from *snow-free* to *snow* is not allowed in *ablation*. If the pixel is labelled as *snow-free* at $t - 1$, it means that for sake of coherence it turned to *snow-free* at t_{SD} . We also know the date of the last accumulation after t_{SD} , i.e., t_{lastAC} with $t_{SD} \leq t_{lastAC} \leq t - 1$. Hence, we compute the most frequent label accordingly with the majority rules and if it results that i) t is a false positive (FP), we simply set it as *snow-free*; ii) $t - 1$ is a false negative (FN), we need to replace all times starting from the day of the last accumulation state (or t_{SD} , in case the last accumulation precedes t_{SD}) until $t - 1$ with *snow-free* since the transition *snow-free* to *snow* can happen during *ablation* only.

Algorithm 1 Regularization of the snow cover maps with the catchment state.

if *Accumulation* **then**
Transition *snow* to *snow-free* is not allowed!

The pixel is *snow* from $t_{SA} \leq t - 1$.

Between t_{SA} and $t - 1$ all states are possible.

We indicate with t_{lastAB} a day $t_{SA} \leq t_{lastAB} \leq t - 1$
representing the date of the last ablation after t_{SA}
if $t - t_{SA} < 10$ *days* **then**

| **Recent** t_{SA} : check $t \pm 5$ days and compute the most frequent label

else

| **Old** t_{SA} : check last up to 5 HR from t_{SA} to t
| and compute the most frequent label

end
if *most frequent label is snow* **then**

| t is a FN (e.g., missed snow under canopy): set t as *snow*

else

| $t - 1$ is a FP (e.g., cloud detected as snow): set $[t_{lastAB}; t - 1]$ as *snow-free*

end
else
Transition *snow-free* to *snow* is not allowed!

The pixel is *snow-free* from $t_{SD} \leq t - 1$.

Between t_{SD} and $t - 1$ all states are possible.

We indicate with t_{lastAC} a day $t_{SD} \leq t_{lastAC} \leq t - 1$
representing the date of the last accumulation after t_{SD}
if $t - t_{SA} < 10$ *days* **then**

| **Recent** t_{SA} : check $t \pm 5$ days and compute the most frequent label

else

| **Old** t_{SA} : check last up to 5 HR from t_{SA} to t
| and compute the most frequent label

end
if *most frequent label is snow* **then**

| $t - 1$ is a FN (e.g., missed snow patches): set $[t_{lastAC}; t - 1]$ as *snow*

else

| t is a FP (e.g., cloud detected as snow): set t as *snow-free*

end
end

4.2.3 HR SWE reconstruction

Once the catchment state has been defined for each day as described in 4.2.1, and the daily HR SCA time-series has been regularized with the catchment state as described in section 4.2.2, the proposed approach to the HR SWE reconstruction can be initiated. This operation requires to calculate the total amount of melting and redistribute it during the snow season according to the preservation of the mass and the catchment state. For this purpose we estimate the daily potential melting with the degree day (DD) model. For a generic time interval $[t-1; t]$, the potential melting $M_{t-1,t}$ is estimated through the following equation:

$$M_{t-1,t} [mm] = a [mm^{\circ}C^{-1}d^{-1}] \cdot DD_{t-1,t} [^{\circ}Cd] \quad (4.1)$$

where a is the so called DD factor and varies depending on the considered area as well on the considered snow period. We used a value of $a = 4.5 \text{ m}^{\circ} \text{ C}^{-1}\text{d}^{-1}$ for the South Fork catchment and $a = 5.2 \text{ mm}^{\circ}\text{C}^{-1}\text{d}^{-1}$ for the Schnals catchment. The coefficient is calibrated by considering measured SWE and temperature at the AWSs (if available) and taking into account also the range of values derived in previous literature works (Hock 2003). The limitations of this approach will be discussed in Section 4.5.3. $DD_{t-1,t}$ is the DD given by the cumulative sum of the hourly temperatures exceeding a certain threshold:

$$DD_{t-1,t} = \sum_{h=t-1}^t T_h \text{ if } T_h > \hat{T} \quad (4.2)$$

The threshold temperature \hat{T} is set to 0°C .

The DD is first calculated for each station and then spatially interpolated using a three-dimensional universal kriging routine with linear variogram and external drift (Murphy et al. 2020). The choice arises from the results of a leave one out (LOO) cross validation (see Appendix A.2). The variogram parameters are automatically calculated at each time step using a "soft" L1 norm minimization scheme. The number of averaging bins is set as 6 (default value). The kriging is performed on the daily DD values instead of on the raw hourly temperature values to reduce computational times.

We can determine the total amount of melting M_{tot} by summing up all the daily $M_{t-1,t}$ for all those days in *ablation* within the time range $[t_{SA}; t_{SD}]$. It is worth noting that a single pixel may have more than one single snow period, hence we can have more than a couple of t_{SA} - t_{SD} . M_{tot} , which has to be equal the total accumulation A_{tot} , is then calculated as follows:

$$A_{tot} = M_{tot} = \sum_{t=t_{SA}}^{t_{SD}} M_{t-1,t} \text{ if } \textit{ablation} \text{ for } t \quad (4.3)$$

Consequently, it is possible to reallocate the total accumulation on those days which are in *accumulation*:

$$A_{t-1,t} = k_{t-1,t} A_{tot} \text{ if } \textit{accumulation} \text{ for } t \quad (4.4)$$

where $k_{t-1,t}$ is a coefficient that represents the quantity of the snowfall. In case we have a network made by S AWS with measured SWE (or similarly, HS), k is set proportional to the observed snowfalls:

$$k_{t-1,t} = \frac{\sum_{s=1}^S (SWE_t^s - SWE_{t-1}^s)}{\sum_t \sum_{s=1}^S S(SWE_t^s - SWE_{t-1}^s)} \quad \text{if } \textit{accumulation} \text{ for } t \quad (4.5)$$

Note that the number of days in *accumulation* varies for each pixel and consequently the coefficient is function of time and space. In case an informative AWS network is not available, we suggest to consider $k = 1/\sum_t$ for t in accumulation, resulting in a coefficient that is constant over time but still varies over space. Thus, it is possible to determine the final output, i.e., a daily HR SWE time-series, by applying pixel-wise the following rules:

$$SWE(t) = \begin{cases} 0 & \text{if } \textit{snow-free} \\ SWE(t-1) & \text{if } \textit{equilibrium} \\ SWE(t-1) - M_{t-1,t} & \text{if } \textit{ablation} \\ SWE(t-1) + A_{t-1,t} & \text{if } \textit{accumulation} \end{cases} \quad (4.6)$$

It may happen that during *ablation* temperatures are low and the term $M_{t-1,t}$ is equal to 0, thus coinciding with the *equilibrium* state. Note that M may also be greater than 0 but if the state is different from *ablation*, that melting is not encountered. It is in fact possible that temperatures present some inaccuracies or increase without causing a real melting. We also neglect in a simplified manner possible melting occurring during snowfall events. In other words, we assume that *ablation* is only possible when we have simultaneously: i) absence of snowfalls, ii) a decrease of SAR backscattering, and iii) high temperature. The term $A_{t-1,t}$ is instead always positive. It is worth stressing the fact that even though possible redistribution caused by wind and gravitational transport is not explicitly taken into account in Eq. 4.6, its consequences are implicitly appreciated by observing a longer persistence of snow on the ground. Indeed, the potential melting is distributed over space and time by considering the snow cover duration. This implicitly takes into account the difference in the energy inputs due to both the topographic and the redistribution effects providing a good estimation of the total SWE. Moreover, by providing an approximation of the accumulation events we also consider late snowfalls that may occur during the main melting season and that are a large source of error in the state-of-the-art methods (Slater et al. 2013).

4.3 Study Areas and Dataset Description

To assess the performance of the proposed method, we consider two different test areas. The first one is the South Fork catchment located in California, USA, in the Sierra Nevada. For this test site, we considered three hydrological seasons spanning from the 1st of October 2018 to 30th of September 2021. The considered basin has an area around 970 km² and a mean elevation of 3070 m, ranging from a minimum elevation of 1930 m up to a maximum elevation of 4150 m. For this catchment, a spatialized SWE product with a resolution of 50 m is available acquired by the Airborne

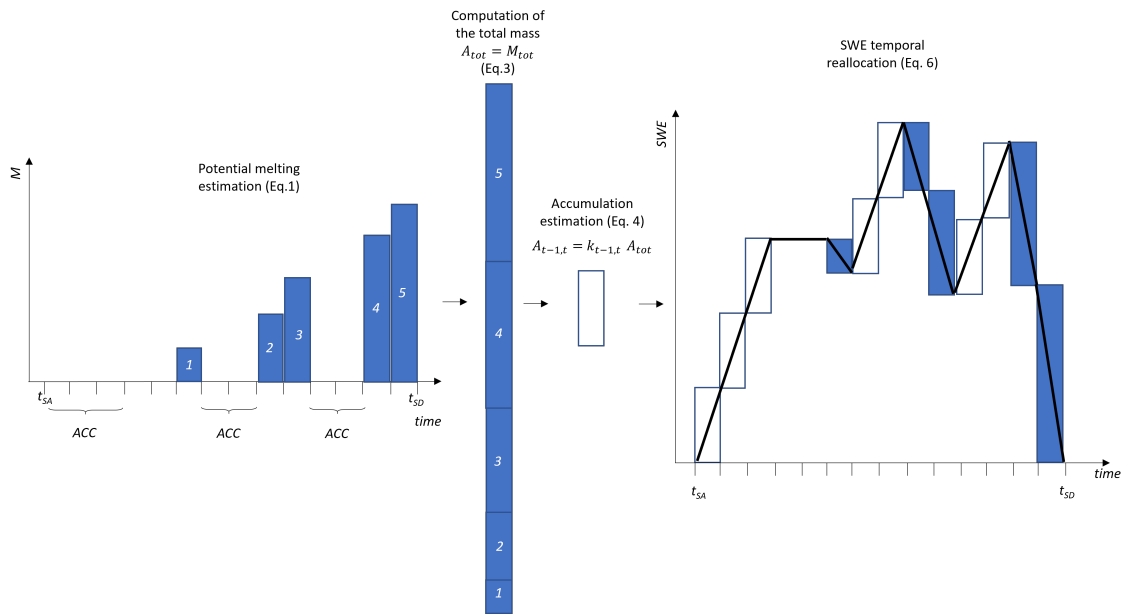


Figure 4.3: Illustration of the reconstruction and temporal reallocation of the SWE for a given pixel. Starting from the left side of the figure, the catchment state is identified for each day of the snow season (delimited by t_{SA} and t_{SD}) and the potential melting is estimated according to Eq.4.1. The sum of all the potential melting at the different days represent the total amount of SWE for that pixel. This is redistributed during the *accumulation* day using Eq.4.4. For this illustrative example, a constant k is considered. As one can notice the reconstructed SWE can represent *accumulation* (even as late spring snowfall), *ablation* and *equilibrium* conditions.

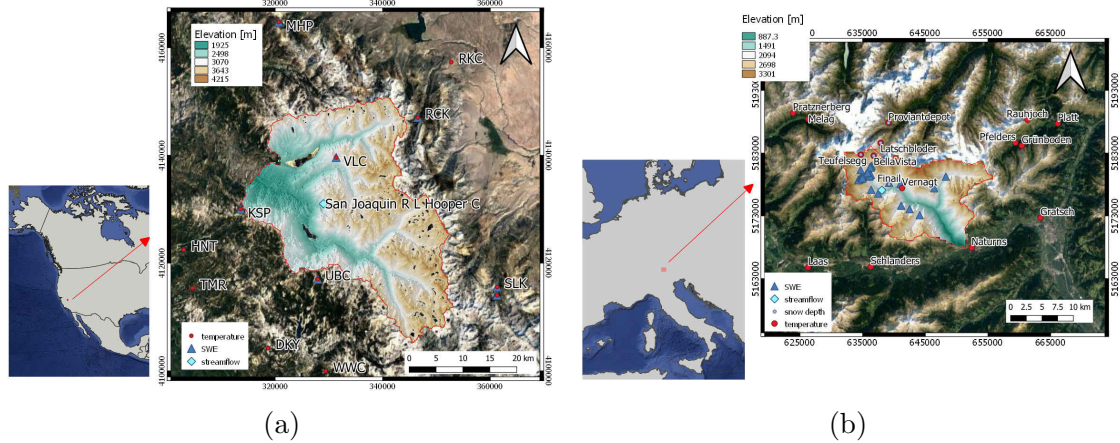


Figure 4.4: Overview of the two test sites: a) South Fork catchment, California, USA, and b) Schnals catchment, South Tyrol, Italy (©2022 Google Maps).

Snow Observatory (ASO). ASO couples imaging spectrometer, laser scanner and a physical model that provides an estimate of the snow density to derive accurate SWE maps (Painter et al. 2016). One snow pillow for continuous SWE measurements and one AWS providing air temperature are available inside the catchment. Moreover, we considered 6 snow pillows and 10 stations with continuous temperature measurements within a radius of around 15 km from the catchment (see 4.4a). These data were downloaded from the United States Department of Agriculture (USDA) Natural Resources Conservation Service (NRCS) Snowpack Telemetry (SNOTEL) network (see <https://www.wcc.nrcs.usda.gov/snow/>) and from the California Data Exchange Center (CDEC) (see <https://cdec.water.ca.gov/>).

The second catchment is the Schnals (Senales in Italian - for brevity we will report the German name only) located in the Vinschgau (Venosta) Valley in South Tyrol, Italy, in the Alps. For this catchment we analyzed two hydrological seasons spanning from the 1st of October 2019 to the 30th of September 2021. The considered area has an extent of about 220 km² and a mean elevation of 2370 m, ranging from a minimum elevation of 590 m up to a maximum elevation of 3550 m. For this test site, manual SWE measurements are available (collected by Avalanche Centre of the Bolzano Province - Lawinenwarndienst - see <https://lawinen.report/weather/snow-profiles> - and by Eurac Research, Institute for Earth Observation). Additionally, we considered the operating temperature and HS sensors of the Province of Bozen (see <https://data.civis.bz.it/it/dataset/misure-meteo-e-idrografiche>). An overview of the Schnals catchment and the location of available measurements is provided in Fig. 4.4b.

The HR daily SCA time-series is derived through the method proposed by Premier, Marin, Steger, Notarnicola & Bruzzone (2021). The input data used for the reconstruction are S2, Landsat-8 and MODIS data. The method requires as input a long time-series of HR images. Hence, we downloaded a total of around 400 scenes for the South Fork catchment and 700 scenes for the Schnals valley from <https://earthexplorer.usgs.gov>. The following steps are applied to opportunely pre-processed the data: i) conversion from digital number to Top of the Atmosphere (ToA) reflectance values, ii) cloud masking through the algorithm s2cloudless avail-

able at <https://github.com/sentinel-hub/sentinel2-cloud-detector> (Zupanc 2017), iii) SCF detection through an unsupervised statistical learning approach (Barella et al. 2022), and iv) binarization of the classification results.

The daily MODIS data are needed for those hydrological seasons in analysis only. The ready-to-use MOD10 version 6.1 are distributed by the National Snow and Ice Data Center (see <https://nsidc.org/data/MOD10A1>) (Hall & Riggs 2021). The NDSI values are converted to SCF by using the algorithm proposed by Salomonson & Appel (2004).

The S1 data are downloaded from <https://search.asf.alaska.edu/> and pre-processed (i.e., precise orbit application, thermal noise removal, border noise removal, beta nought calibration, tile assembly, co-registration, multi-temporal filtering, terrain correction, geo-coding and sigma nought calibration). These steps are performed using SNAP (Sentinel Application Platform) and some custom tools. Three tracks are available for each test site, i.e. track 64, 137 and 144 for the South Fork catchment and track 15, 117 and 168 for the Schnals catchment, with a total number of around 480 and 350 downloaded images respectively. The backscattering is then daily interpolated and a multi-temporal analysis is carried out for the three tracks separately. If at least one track shows a drop of at least 2 dB in the signal (Nagler & Rott 2000) w.r.t. a moving average of the 12 previous days, that day is considered to be in *ablation*.

4.4 Experimental Results

In this section, we present the results obtained for the South Fork and for the Schnals catchment.

4.4.1 South Fork catchment

The proposed SWE maps are aggregated at a resolution of 50 m and compared with the corresponding ASO maps, for a total number of 12 dates.

From a qualitative inspection of the results, a general good agreement between the two SWE maps is visible. For sake of brevity we propose here a detailed analysis of the 9th of June 2019, for which we reported in Fig. 4.5 the SWE map obtained with the proposed approach, the SWE produced by ASO and the bias map calculated as pixel-wise difference between the proposed and the reference ASO map. In general, it is possible to notice that the proposed method is able to reproduce spatial patterns similar to the ones detected by ASO. This result shows that the use of HR input data achieve an unique spatial detail, which represents one of the main advantages of the proposed method. By looking at a zoomed area, it is possible to better appreciate this similarity. Nonetheless, it is possible to notice a tendency of the proposed product to underestimate SWE especially in some North exposed areas. This may be due to either i) an error introduced by the DD model, that only considers temperature without accounting for radiation differences linked to different exposures or ii) an error introduced by the reference HS map used in the ASO for defining the amount of snow at the beginning of the season in permanently snow covered areas.

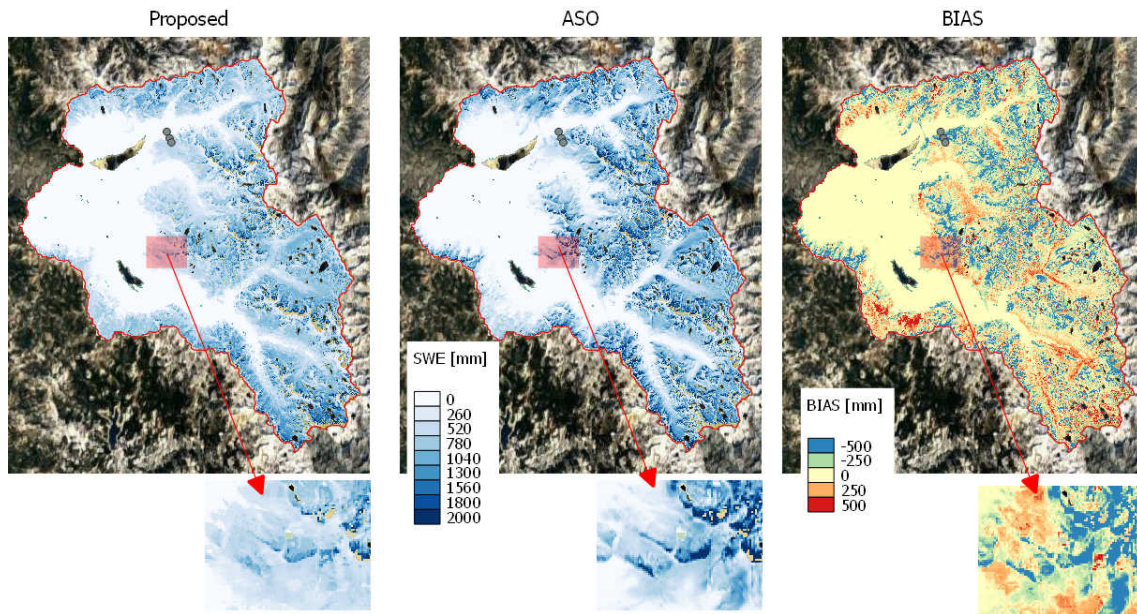


Figure 4.5: Proposed SWE map (on the left), ASO SWE map (in the centre) and bias map calculated as difference between the proposed and ASO SWE (on the right) for the 9th of June 2019. A zoom is shown under the correspondent maps. A transect is shown with three green dots in the North area of the catchment ((©)2022 Google Maps).

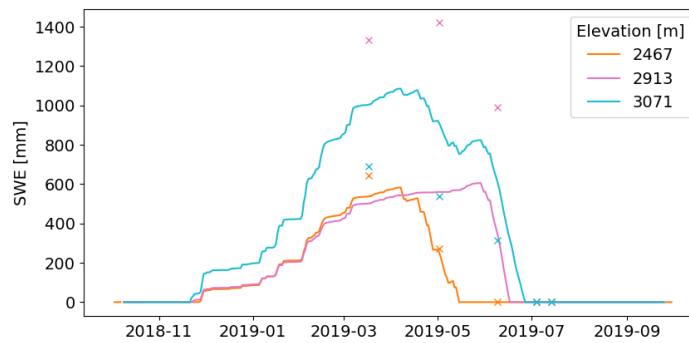


Figure 4.6: SWE temporal trends for: the proposed approach (continuous lines) and ASO (crosses) for the considered transect reported in Fig. 4.5.

In Fig. 4.6 the temporal trend of three points for a selected transect is reported. First of all, it is possible to observe that the proposed product presents an expected behaviour, i.e., longer snow persistence and increasing SWE for higher elevation. On the other hand, ASO shows higher SWE for the mid elevation point. It is worth noting that even though we use ASO as reference product, some inconsistencies may be present due to a possible inaccurate estimation of the snow density by the model.

The Volcanic Knob (VLC) monitoring site, which is located inside the analyzed area, is also used for evaluating the obtained results showing a very good agreement (see Fig. 4.7). However, it is worth to keep in mind that in-situ SWE stations are usually located in flat forest clearings and may be not overly representative of the overall complex topography settings of the study area. Note that the first year 2018/19 is also used to set up the constant a used for the DD model, according also to values found in literature (Hock 2003). The validity of the chosen value is confirmed by a good agreement of the results for the following two seasons. Interestingly, even though the stations are used to identify the *accumulation* state the temporal SWE trend does not necessarily present everywhere the same shape as for the station (see in Fig. 4.6 and 4.7). In fact, this final result is influenced also by the persistence of the snow as well by the potential melting, that varies depending especially by the elevation as it is calculated with a kriging with external drift. Hence, the good agreement with the station trend is also confirming the validity of the proposed method.

The results of a quantitative global analysis are reported in Table 4.1. The evaluation shows a generally good correlation between the two products, i.e., 0.729 on average. The average bias is -40 mm and the average RMSE is 216 mm. The highest bias and RMSE values are generally encountered in the mid-winter acquisitions. This is due to the fact that the snow cover in that period of the year is higher, and consequently the SWE, thus generating a potential larger error. Moreover, it is possible to have an inaccurate detection of the exact location and duration of the snowfalls. This may be due to the fact that the accumulation in the proposed method is driven by punctual measurements and may be not representative of the entire catchment as described in Sec. 4.2.1. For the South Fork area, only one station is inside the catchment and this is not enough to capture the high variability of precipitations as expected.

In Fig. 4.8, the temporal trend of the total SWE for the three considered hydrological seasons is shown. We notice a general good agreement between the total amount of SWE estimated through the two approaches. The plot also gives an idea of the large differences that can be encountered for different seasons and that are well captured by the proposed method. The first hydrological season 2018/2019 shows the highest amount of SWE, while the others are drier. The tendency is of a slight underestimation of SWE for the proposed method w.r.t. ASO results for the first two seasons, while the last is overestimated as also shown in Table 4.1. The possible reasons will be discussed in Sec. 4.5.

A more detailed analysis is presented in Fig. 4.9, where we show the trend of the maximum of SWE versus elevation, slope and aspect. The results show an increasing trend of SWE with altitude that is inverted for highest elevations, since these usually present very steep slopes and consequently a marked tendency of snow

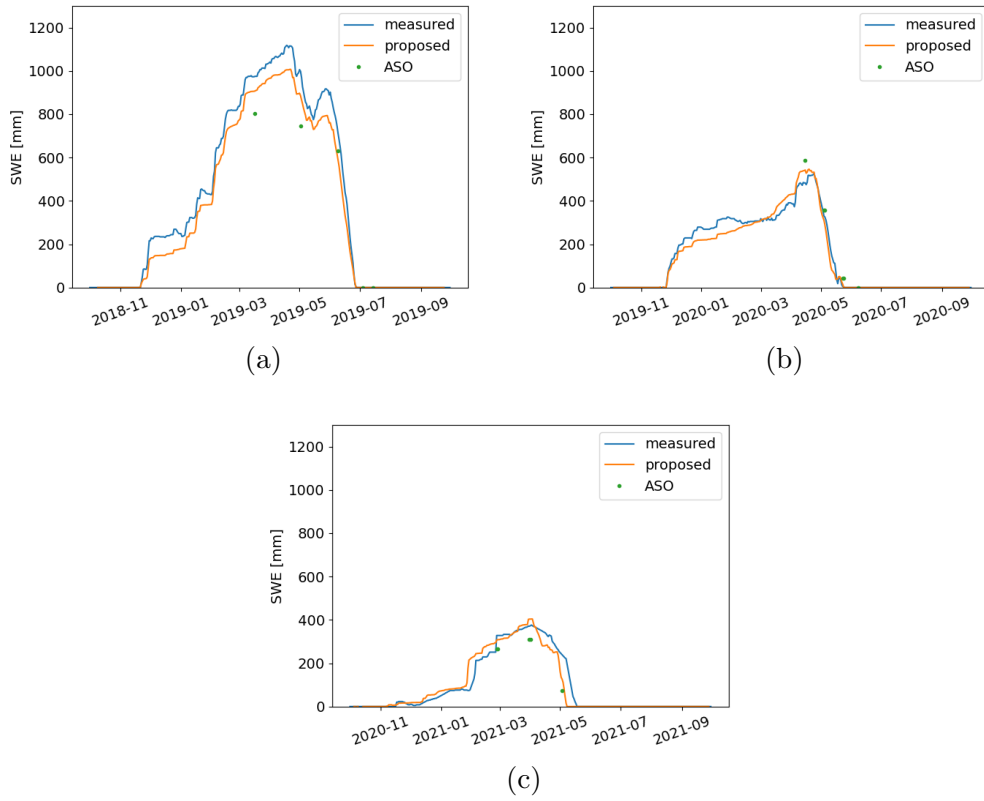


Figure 4.7: SWE obtained by the proposed approach (in orange) against the measured SWE (in blue) at the Volcanic Knob test site for the hydrological seasons a) 2018/19, b) 2019/20 and c) 2020/21.

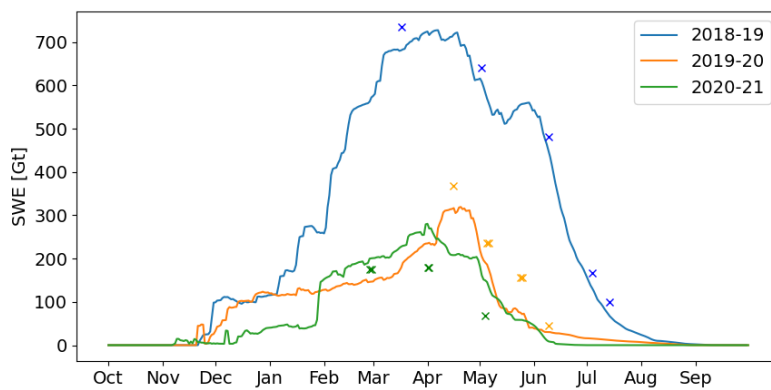


Figure 4.8: Temporal trends of the total SWE for the South Fork catchment over the three analyzed seasons. Crosses represent the ASO reference.

Table 4.1: Results of the comparison between the proposed SWE and ASO products for the South Fork catchment. Bias, RMSE and correlation are calculated pixel-wise. SWE tot is the SWE integrated over space.

Date	BIAS [mm]	RMSE [mm]	Correlation [-]	SWE tot ASO [Gt]	SWE tot proposed [Gt]
17/03/2019	-88	311	0.73	734	653
02/05/2019	-66	308	0.84	640	580
09/06/2019	-71	299	0.86	482	417
04/07/2019	-59	197	0.85	167	113
14/07/2019	-51	166	0.80	100	53
15/04/2020	-70	239	0.64	367	303
05/05/2020	-65	225	0.66	235	165
23/05/2020	-95	234	0.65	156	69
08/06/2020	-20	152	0.66	44	26
26/02/2021	-8	130	0.65	175	167
31/03/2021	59	168	0.70	180	235
03/05/2021	49	166	0.70	67	123

to be subjected to gravitational transport. This is also confirmed by the second graph, where steeper slopes present less SWE. Another coherent result is also the bigger amount of SWE for North exposed areas. These results confirm that the method is suitable to be exploited for hydrological applications.

For more results derived by the comparison between the proposed method and the ASO reference product we refer the reader to the Appendix A.3 (see Fig. A.4). Here we report a detailed analysis on the total SWE for all the available ASO SWE information considering different elevation, aspect and slope belts (see Fig. A.5 and A.6).

4.4.2 Schnals catchment

For the Schnals valley, reference spatialized data of SWE are not available. However, manually collected SWE measurements for the hydrological season 2020/21 were collected also along spatial transects. Differently from the South Fork catchment, these measurements are acquired over complex terrain allowing to test the ability of the method to cope with complex topography. For more details about the measurement location, please refer to the Appendix A.1, Fig. A.1. The results show a bias of 38 mm and a RMSE of 209 mm, indicating a general good agreement. For sake of brevity, we report in Fig. 4.10 only few examples of reconstructed SWE evaluated against the manual measurements. It is possible to notice, in accordance with the results obtained for the South Fork catchment, that the variability from an area to another of the catchment is properly caught by the proposed method. This is due to the different persistence of snow on ground that modulates the spatial variability of the potential melting estimated by the DD model. It is possible to notice in the figure that the SWE tends to increase with the elevation.

In Fig. 4.11 we report the map of the SWE maximum for the two analyzed

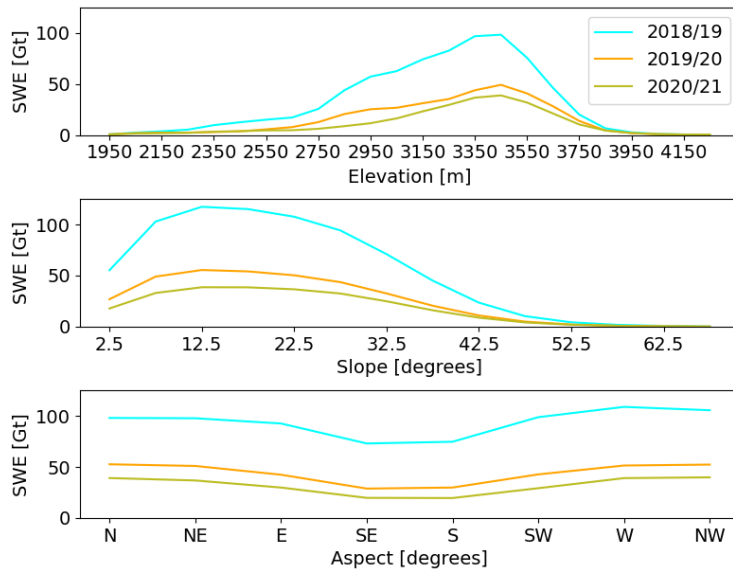


Figure 4.9: Trends of the maximum of SWE for the hydrological seasons 2018-2021 w.r.t. the elevation (up), slope (centre) and aspect (low) for the South Fork catchment.

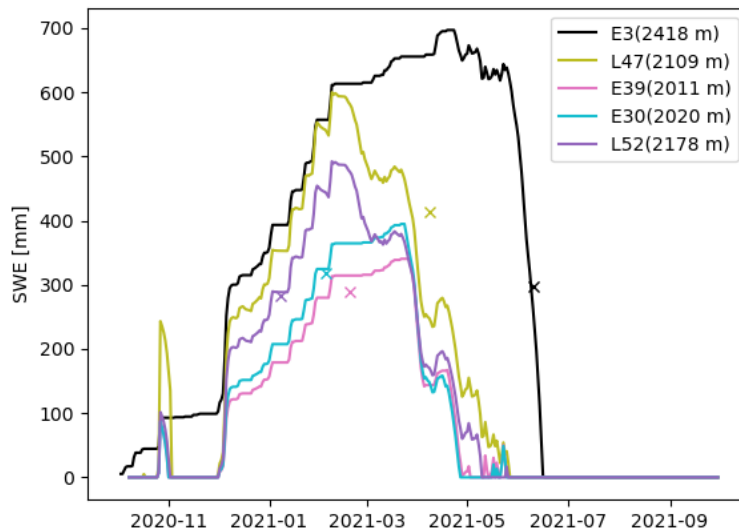


Figure 4.10: SWE proposed (continuous line) against the manual measured SWE (crosses) at some locations in the Schnals catchment (see Fig. A.1).

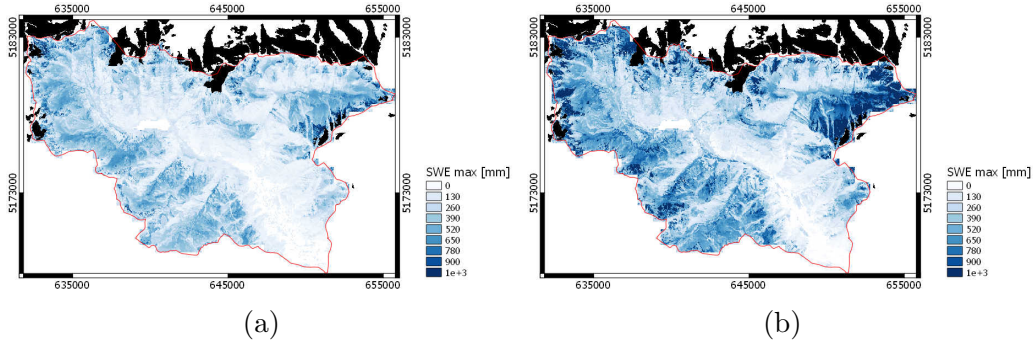


Figure 4.11: Maximum of SWE for the Schnals catchment for the hydrological seasons a) 2019/20 and b) 2020/21.

hydrological seasons. It is possible to see that the season 2020/21 is characterized by a higher amount of SWE. However, the two years show similar patterns that are coherent with the morphology of the study area. In detail, we can notice that interestingly there is a higher amount of SWE especially in the East part of the catchment that corresponds to the glacierized area of the Roteck/Monte Rosso mountain. We found a longer persistence of snow for these North exposed slopes and consequently a larger amount of reconstructed SWE. The consistency of the SWE patterns is also confirmed by Fig. 4.12, from which similar considerations as for the South Fork catchment can be carried out. Another qualitative indicator of the goodness of the results is given in Fig. 4.13. The trend of the SWE maximum over time is represented together with the discharge measured at Schnalserbach - Gerstgras. In the second year, higher SWE amounts correspond to a higher peak in terms of measured discharge as expected. Moreover, it is possible to appreciate for the two seasons an increase of discharge that happens in correspondence of the SWE decrease.

4.5 Discussion

We have presented in the previous section the quantitative and qualitative results for the two study areas. Notwithstanding the good agreement with the observed measures as well as with the reference ASO product, we will draw in this section a critical analysis of the proposed approach. In detail, each main step, i.e., catchment state identification, SCA regularization and SWE reconstruction, is analysed in the following paragraphs, focusing on the main sources of errors.

4.5.1 Error in the determination of the catchment state

In Sec. 4.2.1 we have described how to define the *accumulation* state starting from in-situ SWE, HS or precipitation measurements. We suggested that a network of AWS is needed to cope with the possible heterogeneity of the snowfalls inside the catchment. However, we would like to discuss more in detail the topology of such a network. In Sec. 4.2.1 we assumed that the *accumulation* state refers to all the catchment covered by snow without distinguishing between areas that are interested

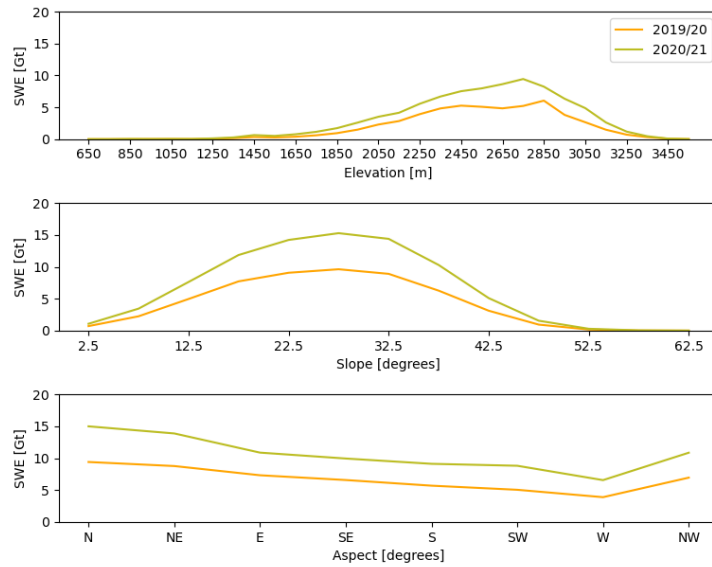


Figure 4.12: Trends of the maximum of SWE for the hydrological seasons 2019-2021 w.r.t. the elevation (up), slope (centre) and aspect (low) for the Schnals catchment.

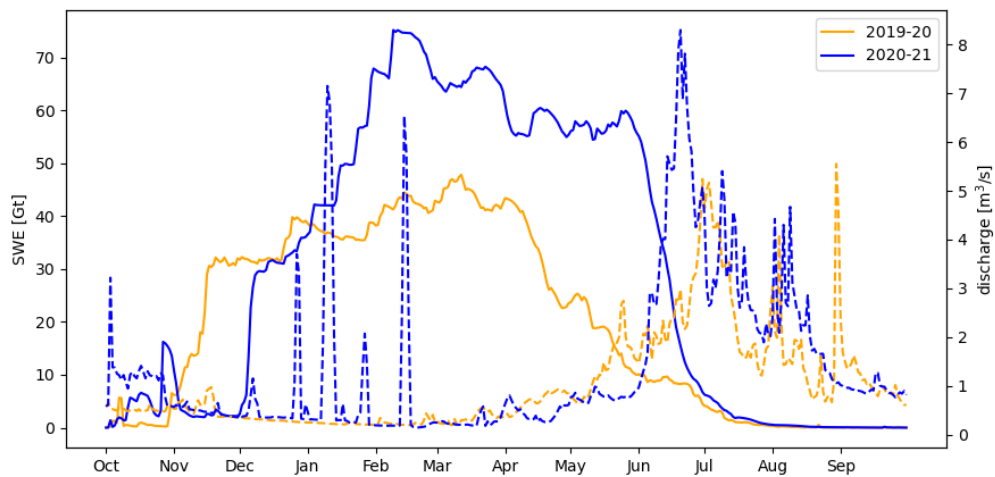


Figure 4.13: SWE for the Schnals catchment for the hydrological seasons 2019-2021. Continuous lines represent SWE, dashed lines represent the discharge measured at Schnalserbach - Gerstgras.

by a snowfall and areas that are in *equilibrium* or *ablation*, e.g., this is the case of simultaneously rain-on-snow and snowfall inside the catchment. We introduced this simplifying hypothesis since it is difficult to precisely determine where the snowfall occurs with a HR detail. By strictly taking this assumption, and therefore exploiting only one in-situ measurement, the results are still affected by wind and gravitational redistribution that influence the AWS observations. This in turn may affect the final SWE results that are biased by wrong state identification. Moreover, in some remote areas automatic measurements can be completely missing. Hence, there is the need to identify the *accumulation* state at HR as done for the *ablation* state using the SAR information. A possible solution is to spatialize the AWS information considering for example elevation bands where the hypothesis of a constant state is more reliable (i.e., a similar concept as the hydrological response unit). Nonetheless, this is a challenging task that requires a well distributed AWS network or to couple our approach with a physically based model able to spatialize correctly the AWS information. Even if the modularity of the proposed approach allows the separation of the different steps that can be easily interchanged with other possible solutions, this is out of the scope of this chapter.

Another possible solution is to exploit once again the information provided by the satellite missions. Indeed, the use of satellite information collected over larger and remote areas represents an interesting enhancement of the proposed method. The prediction of the catchment state could be provided for example by satellite information about SCA variations that are connected to SWE changes. Especially at the beginning of the season, an important snowfall is well represented by a strong increment in terms of SCA. However, there are some ambiguities that need to be solved. For example, when observing constant SCA or when SCA is 100% we cannot determine the state of the catchment. In this sense, the size of the catchment plays an important role that needs to be further investigated. As interesting alternative we also mention the use of SAR data. In this work, we exploited S1 to detect the snowpack melting. However, the signal seems to be also sensitive to the presence of fresh snow, showing an increase of the backscattering in correspondence of a snowfall (e.g., Lievens et al. 2022, Tsang et al. 2021). The poor temporal resolution represents however a strong limitation for a practical application.

4.5.2 Error in the SCA derivation and regularization

It is worth discussing here the SCA regularization more in detail. In Fig. 4.14 and 4.15 we show the SCA before and after the regularization for the South Fork and Schnals catchments, respectively. As explained in Sec. 4.5.2, due to the snow cover detection algorithms employed in the proposed method the raw reconstructed SCA presents: i) strong decreasing peaks in correspondence of the HR acquisitions at the beginning of the season that indicate an underestimation of SCA in forested areas, and ii) small increasing peaks in correspondence of the HR acquisitions in the late melting phase that indicate the presence of snow patches that are missed by LR sensors. The regularized SCA is instead more stable and the spurious oscillations, present especially during the most cold winter period, are corrected. The effectiveness of the correction is also visible by looking at a corrected image. Fig.

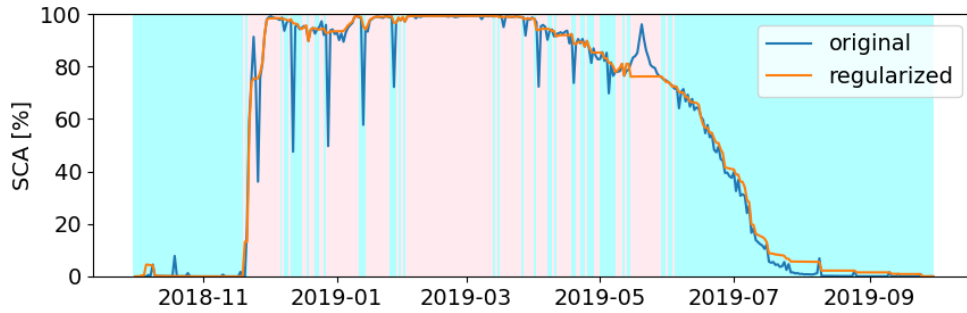
4.16 represents a common situation when foggy and mixed pixels are classified erroneously. The proposed correction improves the snow detection especially in these complicate cases.

An evident case where an overestimation of the SCA is introduced is in the season 2020/21 in May/June for the South Fork catchment (see Fig. 4.14c). This error is due to the fact that the AWS do not indicate an *accumulation* in correspondence of the peaks that happen in the late melting phase. Hence, the label is corrected according to the majority rule in *ablation* in the case of an old snowfall (see Sec. 4.2.2 and Algorithm 1). Many pixels are considered as TP, leading to the propagation of the *snow* pixels backward and the consequent overestimation of SCA. This in turn leads to an overestimation of the SWE as shown in the results (see Sec. 4.4.1). On the other hand, an underestimation of the SCA is introduced for example in May 2019 for the South Fork catchment (see Fig. 4.14a). By an accurate inspection of the conditions that lead to the flattening of the SCA during the late snowfall, it has been showed that the stations indicate a long period as *accumulation*, i.e., from 16th until the 29th of May, while the peak starts decreasing in the original SCA time-series starting from the 21st of May. According to the majority rule for a recent snowfall, the pixels are marked as FP. In fact, the most frequent label is *snow-free* since they are *snow-free* for sure from t onward and this implies the replacement with *snow free* backward until the day of last ablation. It is possible that the AWS present some sensor errors, but this could also be the case of a mixed state inside the catchment. In other words, the AWS reveal a snowfall but this is most likely happening at high elevations, while the SCA is decreasing due to an ongoing melting especially in the lower elevation belts of the catchment (SCA from $\sim 100\%$ to $\sim 80\%$ means that low elevations are getting snow-free). It may be possible that at low elevations it rained while at higher elevations the AWS correctly detect a snowfall. However, we expect that such an ephemeral snowfall is not affecting the total amount of SWE, as we have seen in the Sec. 4.4.1. As future perspective, it is worth noting that the availability of more HR images (e.g., Landsat-9) will help to mitigate the errors in the daily SCA reconstruction.

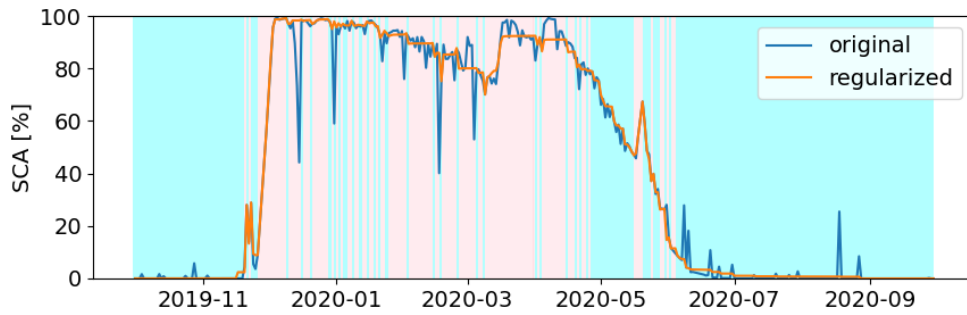
4.5.3 Error in the SWE reconstruction

In Sec. 4.4 we have presented the results of the proposed method. We have shown the differences that arise when comparing the results of our method with a spatialized product (ASO). We would like to discuss here the sources of error and the major weaknesses of the proposed method. The potential source of errors are represented by i) the temperature data, that in turn affects the DD model, and ii) the wrong identification of t_{SA} and t_{SD} , that depends on the accuracy of both the SCA time-series and the catchment state. Since the input data are subjected to several degrees of preprocessing, it is difficult to carry out a specific sensitivity analysis of the problem. The most important factors are discussed in the work of Slater et al. (2013). Instead, we perform here a critical analysis for better defining future developments to improve the proposed method.

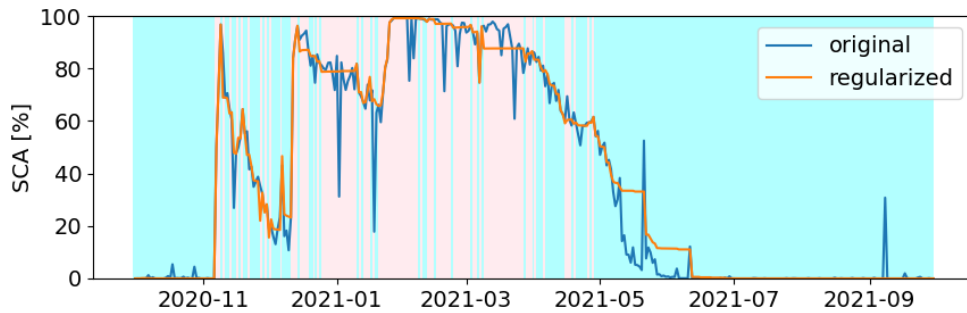
The implications of a wrong detection of t_{SD} are much more important than



(a)

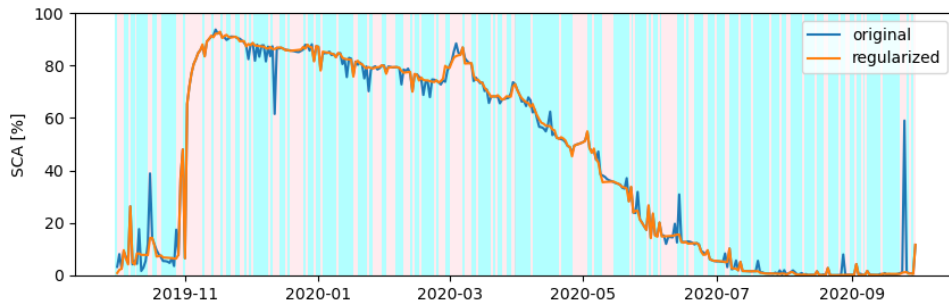


(b)

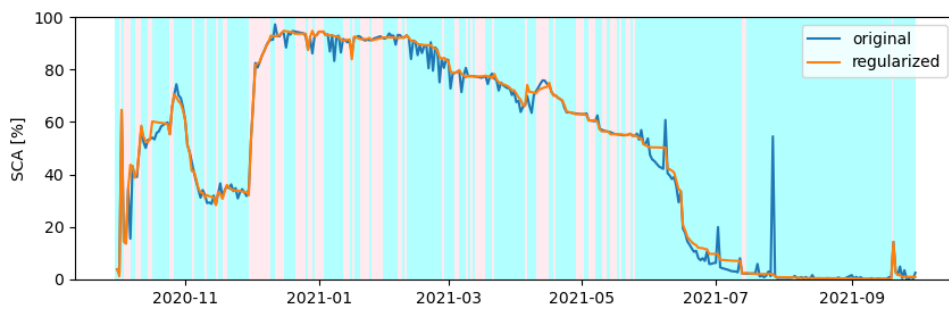


(c)

Figure 4.14: SCA time-series in the South Fork catchment for the hydrological seasons a) 2018/19, b) 2019/20 and c) 2020/21. Original input version (in blue) and corrected version (in orange) after the application of the proposed regularization. The background colors correspond to the ablation state (in cyan) and the accumulation state (in pink).

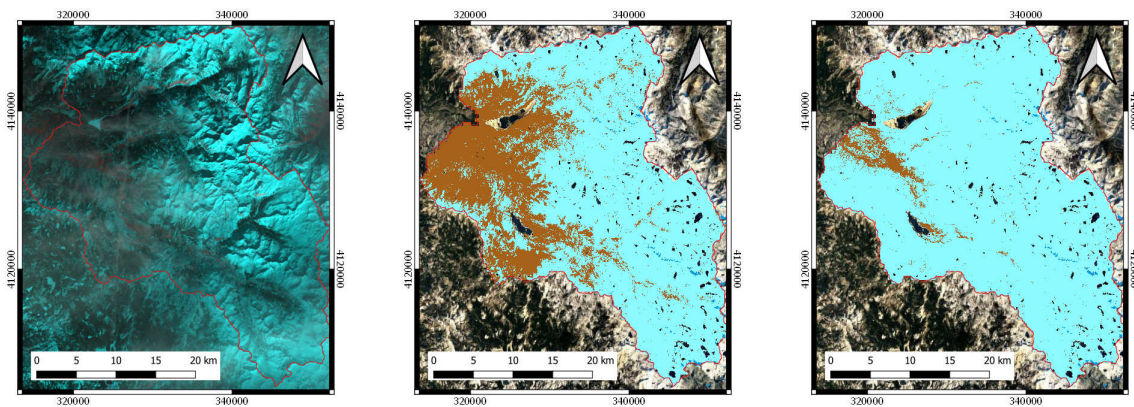


(a)



(b)

Figure 4.15: SCA time-series in the Schnals catchment for the hydrological seasons a) 2019/20 and b) 2020/21. Original input version (in blue) and corrected version (in orange) after the application of the proposed post-filter. The background colors correspond to the ablation state (in cyan) and the accumulation state (in pink).



(a)

(b)

(c)

Figure 4.16: Example of a regularized snow map on the date 12/01/2020 for the South Fork catchment: a) false-color composition (R:SWIR,G:NIR,B:RED), b) input snow cover map, and c) regularized snow cover map.

the wrong identification of t_{SA} . At the end of the ablation period, M is high and therefore the total SWE for a pixel, which is given by the potential melting integrated over time for days in ablation, can be strongly altered by introducing either an overestimation or an underestimation, depending on the case. The error can also be propagated for several days during the melting season. On the contrary, in the period of the year when most consistent snowfalls happen at the beginning of the season, the days in *ablation* are few, temperatures are low, consequently M is negligible (see Eq. 4.1) and does not change so much from one day to the other.

The use of a simple DD model for computing the potential melting is another source of error. This simple model does not take into account different energy inputs due to either geomorphometrical features or different periods of the year, since we used a constant DD factor. This may be the case of the overestimation of SWE happening during the hydrological season 2020/21 as shown in Sec. 4.4.1. In fact, this year presents an anticipated melting. Hence, we expect a lower energy input w.r.t. the season when the DD factor has been calibrated. Even though we are aware of the limitations of such a simple model, we did not consider the use of a more complex model, since this is not the focus of this work. An interesting further development is to test the approach with a more sophisticated potential melting estimation. Since the potential melting is calculated separately, this step can be easily replaced.

As potential correction of the DD model, we proposed the use of S1 for identifying the timing of the melting phase. In fact, it may be that the DD detects high temperatures but the energy is still not sufficient to cause the snowpack melting. Even though we do not expect big differences since temperatures are low in the first phase of the melting and consequently the potential melting is low, the spatialization of temperature may also be affected by possible errors. S1 represents a spatialized way to identify the melting, but it presents as major disadvantage a poor temporal resolution, i.e., few days. As future development, we aim at exploiting S1 and the new HR land surface temperature acquired by the next Sentinel generation as a proxy of the potential melting estimation, thus enlarging the applicability of the proposed method in remote areas.

Finally it is worth mentioning that, the uncertainty introduced in the method are also linked to the high spatial heterogeneity of the SWE. It is possible to encounter a very large variability also within a pixel with size of 25 m as shown by the SWE measurements acquired in Schnalstal by Warscher et al. (2021). This results in an intrinsic difficulty to evaluate the output with an appropriate reference data.

4.6 Conclusions

In this work we presented a novel approach to reconstruct daily HR SWE maps for a mountainous catchment. We started by determining the state of the catchment, i.e. if it is subjected to *accumulation* (increase of SWE), *ablation* (decrease of SWE) or *equilibrium* (constant SWE). The state was identified exploiting both i) in-situ SWE or HS data, which provide information about the snowfall; and ii) multi-temporal SAR information to decide if the pixel is melting. Moreover, a novel daily HR SCA time-series was used to determine the dates of snow appearance

and disappearance, which represents an information with unprecedented spatial and temporal detail. The SCA time-series was opportunely regularized according to the catchment state. Furthermore, the state was also used as necessary information for the SWE reconstruction, i.e. whether SWE is added or removed. The potential melting was estimated by mean of a simple DD model after having spatialized in-situ temperature observations. The SWE was reconstructed for the entire snow season without the need of precipitation data as input. In fact, despite snow depth or SWE increments are considered for detecting snowfalls, the method does not require quantitative spatialized precipitation data that are often affected by uncertainties. The results obtained for two different test sites, i.e., the South Fork catchment and the Schnals catchment demonstrated the effectiveness of the proposed approach to estimate the HR SWE. For the first catchment, the results were evaluated against the ASO SWE product at 50 m, showing an average bias of -40 mm. For the second site, the results were evaluated against manual measurements showing a bias of 38 mm. The obtained results were extensively discussed also considering possible hydrological applications of such a product. In this sense, we have seen that the results are very promising, since they i) are able to well capture the typical spatial variability of a HR product, ii) show spatial patterns that are consistent with the reference product, as well as with the geomorphology of the study area, iii) provide a reliable global balance at a catchment scale, and iv) reproduce the variability of different hydrological seasons.

Finally, we can state that the use of HR SCA for SWE reconstruction is more adequate to sample the variation of SWE due to the complex topography of mountainous catchments. Some technological limitations are present (e.g., necessity of merging LR and HR sensors given the absence of daily optical HR acquisitions, scarce temporal resolution of SAR acquisitions). Even though the proposed approach tries to overcome all these limitations, we expect that further improvements will be introduced also by future satellite missions. This will open opportunities not only to improve the proposed method but also to obtain a near-real time predictor of SWE for large hydrological and ecological applications.

Acknowledgements

This work was supported by the Swiss National Science Foundation (SNF) project "Snowtinel: Sentinel-1 SAR assisted catchment hydrology: toward an improved snow-melt dynamics for alpine regions" Contract No. 200021L205190.

We also would like to thank the NASA Airborne Snow Observatory (ASO) for providing free-of-charge data.

Conclusions

This chapter concludes the thesis by presenting a general discussion of the work described and by providing a summary of the novel contributions illustrated in the document. Finally, possible future developments of the proposed research work are presented

Summary and Discussion

In this thesis we have investigated three different aspects of snow monitoring through remote-sensing based approaches, namely i) the identification of the snowmelt phases by using Sentinel-1 SAR backscattering, ii) the reconstruction of daily high-resolution SCA time-series by fusing high- and low resolution optical data, and iii) the reconstruction of daily high-resolution SWE time-series by combining both remote sensing and in-situ data. The information obtained by applying the first two developed methods has been used as input for the final SWE reconstruction. Indeed, SWE represents a variable of great hydrological interest. S1 has been shown to be a promising tool to detect the snowmelt phases, i.e., the ripening, the moistening and runoff (see Chapter 2). In detail, we found that the SAR backscattering decreases as soon as the snow starts containing water, and that the backscattering increases as soon as SWE starts decreasing, which corresponds to the release of melt water from the snowpack. We discussed the possible reasons of this increase, which are not directly correlated to the SWE decrease, but most probably to the different snow conditions (e.g., surface roughness), which change the backscattering mechanism. The observation of this behavior allowed us to define a set of rules to identify the snowmelt phases. These rules have been tested in five test sites over the Alps by evaluating the obtained results against in-situ observations or against the output of a physically-based model. We obtained an average RMSE of 6 days for the moistening phase, 4 days for the ripening and 7 days for the runoff phase. A possible application of the snowmelt phases identification is represented by the spatialization of the runoff onset for an entire catchment. We obtained reasonable results in this sense for the Zugspitzplatt, showing a good qualitative correspondence with the geomorphological features of the catchment.

The information about the runoff onset is particularly useful when exploited together with detailed SCA time-series that detect the persistence of snow on ground. We have seen that the trade-off between temporal and spatial resolution of current satellite missions does not allow to sample the snow cover variability with the proper detail. In this sense, current lacks in the state-of-the-art methods require

the definition of novel approaches to provide a daily HR SCA time-series by fusing information coming from high- and low-resolution optical satellite sensors (see Chapter 3). To this purpose, we proposed a novel method to infer the daily HR SCA at a catchment scale by exploiting the patterns that repeat inter-annually in the snow cover distribution due to the geomorphometry and the meteorology of the considered area. The approach allowed us to obtain an average OA of 92% when tested in a watershed in the Sierra Nevada, California, by evaluating the results against an independent multi-temporal dataset.

Such a product represents a necessary input to our last proposed work to reconstruct daily HR SWE (see Chapter 4). This final contribution has foreseen the determination of the catchment state, i.e. if it is subjected to *accumulation* (increase of SWE), *ablation* (decrease of SWE) or *equilibrium* (constant SWE). The state was identified exploiting both i) in-situ SWE or HS data, which provide information about the snowfall; and ii) multi-temporal SAR information to decide if the pixel is melting. A novel contribution is represented also by the proposed SCA regularization according to the catchment state. Furthermore, the SWE was reconstructed for the entire snow season without the need of precipitation data as input. The results obtained for the South Fork catchment in the Sierra Nevada, California, were evaluated against the ASO SWE product at 50 m, showing an average bias of -40 mm. The results for a second test site, i.e. the Schnals catchment, Italy, were evaluated against manual measurements showing a bias of 38 mm.

Given the obtained evaluation metrics, the results have shown good performances when evaluated against a reference product. Moreover, they have shown to correctly represent the temporal and spatial variability of the analysed study areas according to their local geomorphology. This result can be appreciated thanks to the improvements in terms of high temporal and spatial resolution w.r.t. the state-of-the-art methods. This achievement was made possible thanks to the large availability of data from the recently launched Copernicus missions that allowed us to fulfill current gaps in literature and develop the proposed novel methods. In particular, it was possible to sample the high spatial and temporal variability of snow accumulation and melting with an unprecedented spatial and temporal detail. We can state that this represents the main contribution of this dissertation. However, we would like to discuss here some challenges that are still present. It is important to highlight that the proposed approaches are strictly inter-connected and single limitations may affect the final SWE time-series reconstruction.

In this thesis, the S1 time-series used for determining the snowmelt phases is kept with its original temporal resolution, i.e., 6 days. This temporal detail is enough to represent important changes in the snowpack properties, as shown in the results, but it represents a relatively scarce temporal resolution to capture quick changes as fluctuations in the temperature especially in the period that precedes the full melting season. These can lead to alternated melting and refreezing cycles that may not be properly represented. Also, the presence of late snowfalls may be completely neglected. Thus, a possible improvement to our work is related to increase the temporal resolution, which would definitely represent an advantage.

Similarly, also the daily reconstructed SCA time-series may present some local

errors despite the good overall results obtained. These arise in particular from the optical data that may be affected by some uncertainties. First, all the processing chain set up for the HR scenes starts from a classification of the multi-spectral images into a binary map, i.e., snow and snow-free. Even though the classification problem goes outside the purposes of this thesis, we would like to remind here that it represents a relevant component that can lead to wrong results in some challenging situation. For example, errors may arise from i) low energy recorded in areas of shadow; ii) atmospheric disturbance, e.g., cirrus and semi-transparent clouds; iii) high reflectance values due to sunglint possibly generated by a thin water layer on the snow surface. Moreover, errors may arise also from missed cloud detection when setting up the cloud mask, as well as missed detection of snow under canopy. Secondly, also the SCF derived from the LR images may be affected by uncertainties, as discussed in Chapter 3. Especially for these reasons, the proposed reconstruction method may fail in some particular situations. Moreover, even though the proposed approach has shown good performances, it is important to keep in mind that in general a good reconstruction cannot replace an observation. Indeed, there are some cases, as for example periods of persistent cloud obstruction, that may require additional external information to be properly represented. We proposed a SCA regularization to overcome some of these errors. Despite it is based on a set of empirical rules that assume a simplified catchment dynamics, it represents a first interesting attempt to consider the catchment as a holistic system.

All these uncertainties affect in turn the final SWE time-series. The proposed SWE reconstruction method implies the use of a potential melting model that also presents some limitations. While it is difficult to understand what is the main source of error in the final product, also a proper evaluation of the results is challenging. In fact, we used for this purpose the ASO spatialized product that is however present only for few dates and only for few catchments. Also, in-situ observations may be not completely representative since they are point measurements that are not able to capture the high intra-pixel variability.

Future Developments

Given the obtained results and the discussion drawn in this thesis, it is possible to point out that future improvements will be naturally introduced by the launch of future satellite missions that will improve the spatial and temporal resolution of the acquired images. This will also open the doors to novel approaches completely independent from in-situ measurements. An improvement in terms of S1 temporal resolution may be introduced also by merging the different available tracks. We are aware that some works have been presented in this sense and need to be considered for further developments ((e.g., Small 2011)). Regarding the problems linked to optical image classification, it represents a largely investigated topic that however still offers room for improvement ((e.g., Barella et al. 2022)). A possible alternative strategy is represented by a change of perspective in terms of the used methodological approach. While at the moment the final SWE time-series is obtained only after several steps, which may introduce uncertainty in cascade, we aim at developing a more complex architecture based for example on deep learning approaches that

encloses all the raw input data to derive the final product of interest. We believe that such an approach may outperform the proposed method and be used operationally. Indeed, we expect that a deep learning architecture if properly trained and constrained, can learn and improve automatically some of the cumbersome rules that we had to set up in this thesis. However, our multi-step approach has helped in investigating the physical aspects and the driving factors of the accumulation and snowmelt phenomena.

Another interesting item that needs to be better investigated is related to the operational application of the proposed method. In other words, the approach should be tested on a large number of catchments. Different conditions may lead to different results (e.g., different land cover type or weather forcings). Also the size of the analyzed area is an interesting variable to investigate, since larger areas would require more computational time and may represent a bottleneck given the large amount of data involved in the computation. Moreover, all the analyses are driven at a catchment scale. In this sense, considering the correct size of the catchment is very important, since the area should be not too big in order to be subjected to the same weather forcings. For this reason, it is still recommended to consider subcatchments instead of too large areas. Apart from the spatial generalization, the method represents potential attractiveness also to be tested on a long time frame. In particular, it would be interesting to check whether the information acquired in the last years with the current satellite missions can be transferred also in the past, when the Sentinel missions were not available yet. This would allow us to better investigate the relationship between SCA and SWE, possibly leading to a derivation of the SDC that may be exploited also for a near real-time prediction. Moreover, such a long term analysis is interesting for giving insights on variations related to climate change.

Finally, another future development is represented by the derivation of a complete hydrological study for a given catchment. For this purpose, also other factors as the evapotranspiration and the subsurface runoff need to be considered possibly by coupling the obtained results with physically-based model. Especially in areas where resources are mostly dependent by the nival melt, a correct determination of SWE is essential for retrieving as final variable the streamflow runoff. Once again, the crucial advantage of remote sensing observations is in this sense represented by their application in poorly-monitored system with low cost strategies.

Bibliography

- Aalstad, K., Westermann, S. & Bertino, L. (2020), ‘Evaluating satellite retrieved fractional snow-covered area at a high-arctic site using terrestrial photography’, *Remote Sensing of Environment* **239**, 111618.
- Anderton, S., White, S. & Alvera, B. (2002), ‘Micro-scale spatial variability and the timing of snow melt runoff in a high mountain catchment’, *Journal of Hydrology* **268**(1-4), 158–176.
- Archer, D. & Stewart, D. (1995), ‘The installation and use of a snow pillow to monitor snow water equivalent’, *Water and environmental management: journal of the Institution of Water and Environmental Management* **9**(3), 221–230.
- Arsenault, K. R. & Houser, P. R. (2018), ‘Generating observation-based snow depletion curves for use in snow cover data assimilation’, *Geosciences* **8**(12), 484.
- Avanzi, F., De Michele, C., Morin, S., Carmagnola, C. M., Ghezzi, A. & Lejeune, Y. (2016), ‘Model complexity and data requirements in snow hydrology: seeking a balance in practical applications’, *Hydrological processes* **30**(13), 2106–2118.
- Baghdadi, N., Gauthier, Y. & Bernier, M. (1997), ‘Capability of multitemporal ers-1 sar data for wet-snow mapping’, *Remote sensing of environment* **60**(2), 174–186.
- Baghdadi, N., Gauthier, Y., Bernier, M. & Fortin, J.-P. (2000), ‘Potential and limitations of radarsat sar data for wet snow monitoring’, *IEEE Transactions on Geoscience and Remote sensing* **38**(1), 316–320.
- Bair, E. H., Rittger, K., Davis, R. E., Painter, T. H. & Dozier, J. (2016), ‘Validating reconstruction of snow water equivalent in california’s sierra nevada using measurements from the nasa airborne snow observatory’, *Water Resources Research* **52**(11), 8437–8460.
- Bair, E. H., Stillinger, T. & Dozier, J. (2021), ‘Snow property inversion from remote sensing (spires): A generalized multispectral unmixing approach with examples from modis and landsat 8 oli’, *IEEE TGRS* **59**(9), 7270–7284.
- Balk, B. & Elder, K. (2000), ‘Combining binary decision tree and geostatistical methods to estimate snow distribution in a mountain watershed’, *Water Resources Research* **36**(1), 13–26.

- Barella, R., Marin, C., Gianinetto, M. & Notarnicola, C. (2022), A novel approach to high resolution snow cover fraction retrieval in mountainous regions, *in* '2022 IEEE International Geoscience and Remote Sensing Symposium IGARSS', IEEE.
- Bartelt, P. & Lehning, M. (2002), 'A physical snowpack model for the swiss avalanche warning: Part i: numerical model', *Cold Regions Science and Technology* **35**(3), 123–145.
- Bavay, M. & Egger, T. (2014), 'Meteoio 2.4. 2: a preprocessing library for meteorological data', *Geoscientific Model Development* **7**(6), 3135–3151.
- Bellaire, S., van Herwijnen, A., Mitterer, C. & Schweizer, J. (2017), 'On forecasting wet-snow avalanche activity using simulated snow cover data', *Cold Regions Science and Technology* **144**, 28–38.
- Beniston, M., Farinotti, D., Stoffel, M., Andreassen, L. M., Coppola, E., Eckert, N., Fantini, A., Giacona, F., Hauck, C., Huss, M. et al. (2018), 'The european mountain cryosphere: a review of its current state, trends, and future challenges', *Cryosphere* **12**(2), 759–794.
- Berman, E. E., Bolton, D. K., Coops, N. C., Mityok, Z. K., Stenhouse, G. B. & Moore, R. D. (2018), 'Daily estimates of landsat fractional snow cover driven by modis and dynamic time-warping', *Remote Sensing of Environment* **216**, 635–646.
- Brun, E., David, P., Sudul, M. & Brunot, G. (1992), 'A numerical model to simulate snow-cover stratigraphy for operational avalanche forecasting', *Journal of Glaciology* **38**(128), 13–22.
- Callegari, M., Mazzoli, P., De Gregorio, L., Notarnicola, C., Pasolli, L., Petitta, M. & Pistocchi, A. (2015), 'Seasonal river discharge forecasting using support vector regression: a case study in the italian alps', *Water* **7**(5), 2494–2515.
- Chen, S., Wang, X., Guo, H., Xie, P. & Sirelkhatim, A. M. (2020), 'Spatial and temporal adaptive gap-filling method producing daily cloud-free ndsi time-series', *IEEE Journal of Selected Topics in Applied Earth Observations and Remote Sensing*.
- Chen, S., Wang, X., Guo, H., Xie, P., Wang, J. & Hao, X. (2020), 'A conditional probability interpolation method based on a space-time cube for modis snow cover products gap filling', *Remote Sensing* **12**(21), 3577.
- Cline, D. W. (1997), 'Snow surface energy exchanges and snowmelt at a continental, midlatitude alpine site', *Water Resources Research* **33**(4), 689–701.
- Cline, D. W., Bales, R. C. & Dozier, J. (1998), 'Estimating the spatial distribution of snow in mountain basins using remote sensing and energy balance modeling', *Water Resources Research* **34**(5), 1275–1285.
- Crane, R. & Anderson, M. (1984), 'Satellite discrimination of snow/cloud surfaces', *International Journal of Remote Sensing* **5**(1), 213–223.

- Cristea, N. C., Breckheimer, I., Raleigh, M. S., HilleRisLambers, J. & Lundquist, J. D. (2017), ‘An evaluation of terrain-based downscaling of fractional snow covered area data sets based on lidar-derived snow data and orthoimagery’, *Water Resources Research* **53**(8), 6802–6820.
- Czyzowska-Wisniewski, E. H., van Leeuwen, W. J., Hirschboeck, K. K., Marsh, S. E. & Wisniewski, W. T. (2015), ‘Fractional snow cover estimation in complex alpine-forested environments using an artificial neural network’, *Remote Sensing of Environment* **156**, 403–417.
- Da Ronco, P. & De Michele, C. (2014), ‘Cloud obstruction and snow cover in alpine areas from modis products’, *Hydrology and earth system sciences* **18**(11), 4579–4600.
- DeBeer, C. M. & Pomeroy, J. W. (2017), ‘Influence of snowpack and melt energy heterogeneity on snow cover depletion and snowmelt runoff simulation in a cold mountain environment’, *Journal of hydrology* **553**, 199–213.
- Deng, J., Huang, X., Feng, Q., Ma, X. & Liang, T. (2015), ‘Toward improved daily cloud-free fractional snow cover mapping with multi-source remote sensing data in china’, *Remote Sensing* **7**(6), 6986–7006.
- Denoth, A. (1989), ‘Snow dielectric measurements’, *Advances in Space Research* **9**(1), 233–243.
- Deschamps-Berger, C., Gascoin, S., Berthier, E., Deems, J., Gutmann, E., Dehecq, A., Shean, D. & Dumont, M. (2020), ‘Snow depth mapping from stereo satellite imagery in mountainous terrain: evaluation using airborne laser-scanning data’, *The Cryosphere* **14**(9), 2925–2940.
- DeWalle, D. R. & Rango, A. (2008a), *Principles of snow hydrology*, Cambridge University Press.
- DeWalle, D. & Rango, A. (2008b), ‘Modelling snowmelt runoff’, *Principles of Snow Hydrology. Cambridge University Press, New York, USA* pp. 266–305.
- Dietz, A. J., Kuenzer, C., Gessner, U. & Dech, S. (2012), ‘Remote sensing of snow—a review of available methods’, *International Journal of Remote Sensing* **33**(13), 4094–4134.
- Dilley, A. & O’Brien, D. (1998), ‘Estimating downward clear sky long-wave irradiance at the surface from screen temperature and precipitable water’, *Quarterly Journal of the Royal Meteorological Society* **124**(549), 1391–1401.
- Dingman, S. L. (2015), *Physical hydrology*, Waveland press.
- Dobrevá, I. D. & Klein, A. G. (2011), ‘Fractional snow cover mapping through artificial neural network analysis of modis surface reflectance’, *Remote Sensing of Environment* **115**(12), 3355–3366.

- Dong, C. (2018), ‘Remote sensing, hydrological modeling and in situ observations in snow cover research: A review’, *Journal of Hydrology* **561**, 573–583.
- Dong, C. & Menzel, L. (2016), ‘Producing cloud-free modis snow cover products with conditional probability interpolation and meteorological data’, *Remote Sensing of Environment* **186**, 439–451.
- Dozier, J. (1989), ‘Spectral signature of alpine snow cover from the landsat thematic mapper’, *Remote sensing of environment* **28**, 9–22.
- Dozier, J. & Painter, T. H. (2004), ‘Multispectral and hyperspectral remote sensing of alpine snow properties’, *Annu. Rev. Earth Planet. Sci.* **32**, 465–494.
- Dozier, J., Painter, T. H., Rittger, K. & Frew, J. E. (2008), ‘Time–space continuity of daily maps of fractional snow cover and albedo from modis’, *Advances in Water Resources* **31**(11), 1515–1526.
- Durand, M., Molotch, N. P. & Margulis, S. A. (2008), ‘Merging complementary remote sensing datasets in the context of snow water equivalent reconstruction’, *Remote Sensing of Environment* **112**(3), 1212–1225.
- Dyer, J. (2008), ‘Snow depth and streamflow relationships in large north american watersheds’, *Journal of Geophysical Research: Atmospheres* **113**(D18).
- Earman, S., Campbell, A. R., Phillips, F. M. & Newman, B. D. (2006), ‘Isotopic exchange between snow and atmospheric water vapor: Estimation of the snowmelt component of groundwater recharge in the southwestern united states’, *Journal of Geophysical Research: Atmospheres* **111**(D9).
- Endrizzi, S., Gruber, S., Dall’Amico, M. & Rigon, R. (2014), ‘Geotop 2.0: simulating the combined energy and water balance at and below the land surface accounting for soil freezing, snow cover and terrain effects’, *Geoscientific Model Development* **7**(6), 2831–2857.
- Engel, M., Notarnicola, C., Endrizzi, S. & Bertoldi, G. (2017), ‘Snow model sensitivity analysis to understand spatial and temporal snow dynamics in a high-elevation catchment’, *Hydrological processes* **31**(23), 4151–4168.
- Essery, R., Morin, S., Lejeune, Y. & Ménard, C. B. (2013), ‘A comparison of 1701 snow models using observations from an alpine site’, *Advances in water resources* **55**, 131–148.
- Fassnacht, S. R., Williams, M. & Corrao, M. (2009), ‘Changes in the surface roughness of snow from millimetre to metre scales’, *Ecological Complexity* **6**(3), 221–229.
- Fierz, C., Armstrong, R. L., Durand, Y., Etchevers, P., Greene, E., McClung, D. M., Nishimura, K., Satyawali, P. K. & Sokratov, S. A. (2009), ‘The international classification for seasonal snow on the ground’.

- Fromm, R., Baumgärtner, S., Leitinger, G., Tasser, E. & Höller, P. (2018), ‘Determining the drivers for snow gliding’, *Natural Hazards and Earth System Sciences* **18**(7), 1891–1903.
- Gafurov, A. & Bárdossy, A. (2009), ‘Cloud removal methodology from modis snow cover product’, *Hydrology and Earth System Sciences* **13**(7), 1361–1373.
- Gafurov, A., Vorogushyn, S., Farinotti, D., Duethmann, D., Merkushev, A. & Merz, B. (2015), ‘Snow-cover reconstruction methodology for mountainous regions based on historic in situ observations and recent remote sensing data’, *The Cryosphere* **9**(2), 451–463.
- Gascoin, S., Barrou Dumont, Z., Deschamps-Berger, C., Marti, F., Salgues, G., López-Moreno, J. I., Revuelto, J., Michon, T., Schattan, P. & Hagolle, O. (2020), ‘Estimating fractional snow cover in open terrain from sentinel-2 using the normalized difference snow index’, *Remote Sensing* **12**(18), 2904.
- Ge, Y. & Gong, G. (2010), ‘Land surface insulation response to snow depth variability’, *Journal of Geophysical Research: Atmospheres* **115**(D8).
- Groisman, P. Y. (2001), ‘Snow cover and the climate system’, *Snow ecology: an interdisciplinary examination of snow-covered ecosystems*.
- Guneriussen, T., Hogda, K. A., Johnsen, H. & Lauknes, I. (2001), ‘Insar for estimation of changes in snow water equivalent of dry snow’, *IEEE Transactions on Geoscience and Remote Sensing* **39**(10), 2101–2108.
- Günther, D., Marke, T., Essery, R. & Strasser, U. (2019), ‘Uncertainties in snow-pack simulations—assessing the impact of model structure, parameter choice, and forcing data error on point-scale energy balance snow model performance’, *Water Resources Research* **55**(4), 2779–2800.
- Hall, D. & Riggs, G. (2021), ‘Modis/terra snow cover daily l3 global 500 m sin grid,[2000–2021], version 61’.
- Hanzer, F., Carmagnola, C. M., Ebner, P. P., Koch, F., Monti, F., Bavay, M., Bernhardt, M., Lafaysse, M., Lehning, M., Strasser, U. et al. (2020), ‘Simulation of snow management in alpine ski resorts using three different snow models’, *Cold Regions Science and Technology* **172**, 102995.
- Hastie, T. & Tibshirani, R. (1987), ‘Generalized additive models: some applications’, *Journal of the American Statistical Association* **82**(398), 371–386.
- Helfricht, K., Hartl, L., Koch, R., Marty, C. & Olefs, M. (2018), ‘Obtaining sub-daily new snow density from automated measurements in high mountain regions’, *Hydrology and Earth System Sciences* **22**(5), 2655–2668.
- Hirashima, H., Yamaguchi, S., Sato, A. & Lehning, M. (2010), ‘Numerical modeling of liquid water movement through layered snow based on new measurements of the water retention curve’, *Cold Regions Science and Technology* **64**(2), 94–103.

- Hock, R. (2003), ‘Temperature index melt modelling in mountain areas’, *Journal of hydrology* **282**(1-4), 104–115.
- Hou, J., Huang, C., Zhang, Y., Guo, J. & Gu, J. (2019), ‘Gap-filling of modis fractional snow cover products via non-local spatio-temporal filtering based on machine learning techniques’, *Remote Sensing* **11**(1), 90.
- Hürkamp, K., Tafelmeier, S. & Tschiersch, J. (2017), ‘Influence of melt-freeze-cycles on the radionuclide transport in homogeneous laboratory snowpack’, *Hydrological Processes* **31**(6), 1360–1370.
- Hürkamp, K., Zentner, N., Reckerth, A., Weishaupt, S., Wetzels, K.-F., Tschiersch, J. & Stumpp, C. (2019), ‘Spatial and temporal variability of snow isotopic composition on mt. zugspitze, bavarian alps, germany’, *Journal of Hydrology and Hydromechanics* **67**(1), 49–58.
- Immerzeel, W. W., Lutz, A., Andrade, M., Bahl, A., Biemans, H., Bolch, T., Hyde, S., Brumby, S., Davies, B., Elmore, A. et al. (2020), ‘Importance and vulnerability of the world’s water towers’, *Nature* **577**(7790), 364–369.
- Jones, H. (2001), *Snow ecology: an interdisciplinary examination of snow-covered ecosystems*, Cambridge University Press.
- Jost, G., Weiler, M., Gluns, D. R. & Alila, Y. (2007), ‘The influence of forest and topography on snow accumulation and melt at the watershed-scale’, *Journal of Hydrology* **347**(1-2), 101–115.
- Kattelmann, R. & Dozier, J. (1999), ‘Observations of snowpack ripening in the sierra nevada, california, usa’, *Journal of Glaciology* **45**(151), 409–416.
- Kendra, J. R., Sarabandi, K. & Ulaby, F. T. (1998), ‘Radar measurements of snow: Experiment and analysis’, *IEEE Transactions on Geoscience and Remote Sensing* **36**(3), 864–879.
- Kerr, T., Clark, M., Hendrikx, J. & Anderson, B. (2013), ‘Snow distribution in a steep mid-latitude alpine catchment’, *Advances in water resources* **55**, 17–24.
- Kinar, N. & Pomeroy, J. (2015), ‘Measurement of the physical properties of the snowpack’, *Reviews of Geophysics* **53**(2), 481–544.
- Klein, A. G., Hall, D. K. & Riggs, G. A. (1998), ‘Improving snow cover mapping in forests through the use of a canopy reflectance model’, *Hydrological Processes* **12**(10-11), 1723–1744.
- Koch, F., Henkel, P., Appel, F., Schmid, L., Bach, H., Lamm, M., Pransch, M., Schweizer, J. & Mauser, W. (2019), ‘Retrieval of snow water equivalent, liquid water content, and snow height of dry and wet snow by combining gps signal attenuation and time delay’, *Water Resources Research* **55**(5), 4465–4487.

- Koch, F., Prasch, M., Schmid, L., Schweizer, J. & Mauser, W. (2014), ‘Measuring snow liquid water content with low-cost gps receivers’, *Sensors* **14**(11), 20975–20999.
- Koskinen, J. T., Pulliainen, J. T., Luoju, K. P. & Takala, M. (2009), ‘Monitoring of snow-cover properties during the spring melting period in forested areas’, *IEEE transactions on geoscience and remote sensing* **48**(1), 50–58.
- Lehning, M., Bartelt, P., Brown, B., Fierz, C. & Satyawali, P. (2002), ‘A physical snowpack model for the swiss avalanche warning: Part ii. snow microstructure’, *Cold regions science and technology* **35**(3), 147–167.
- Lehning, M., Bartelt, P., Brown, B., Russi, T., Stöckli, U. & Zimmerli, M. (1999), ‘Snowpack model calculations for avalanche warning based upon a new network of weather and snow stations’, *Cold Regions Science and Technology* **30**(1-3), 145–157.
- Lehning, M., Völksch, I., Gustafsson, D., Nguyen, T. A., Stähli, M. & Zappa, M. (2006), ‘Alpine3d: a detailed model of mountain surface processes and its application to snow hydrology’, *Hydrological Processes: An International Journal* **20**(10), 2111–2128.
- Leinss, S., Wiesmann, A., Lemmetyinen, J. & Hajnsek, I. (2015), ‘Snow water equivalent of dry snow measured by differential interferometry’, *IEEE Journal of Selected Topics in Applied Earth Observations and Remote Sensing* **8**(8), 3773–3790.
- Li, D., Lettenmaier, D. P., Margulis, S. A. & Andreadis, K. (2019), ‘The value of accurate high-resolution and spatially continuous snow information to streamflow forecasts’, *Journal of Hydrometeorology* **20**(4), 731–749.
- Li, H. Y., He, Y. Q., Hao, X. H., Che, T., Wang, J. & Huang, X. D. (2015), ‘Downscaling snow cover fraction data in mountainous regions based on simulated inhomogeneous snow ablation’, *Remote Sensing* **7**(7), 8995–9019.
- Li, X., Fu, W., Shen, H., Huang, C. & Zhang, L. (2017), ‘Monitoring snow cover variability (2000–2014) in the hengduan mountains based on cloud-removed modis products with an adaptive spatio-temporal weighted method’, *Journal of hydrology* **551**, 314–327.
- Li, X., Jing, Y., Shen, H. & Zhang, L. (2019), ‘The recent developments in cloud removal approaches of modis snow cover product’, *Hydrology and Earth System Sciences* **23**(5), 2401–2416.
- Lievens, H., Brangers, I., Marshall, H.-P., Jonas, T., Olefs, M. & De Lannoy, G. (2022), ‘Sentinel-1 snow depth retrieval at sub-kilometer resolution over the european alps’, *The Cryosphere* **16**(1), 159–177.
- Lievens, H., Demuzere, M., Marshall, H.-P., Reichle, R. H., Brucker, L., Brangers, I., de Rosnay, P., Dumont, M., Giroto, M., Immerzeel, W. W. et al. (2019), ‘Snow depth variability in the northern hemisphere mountains observed from space’, *Nature communications* **10**(1), 1–12.

- Lindsay, C., Zhu, J., Miller, A. E., Kirchner, P. & Wilson, T. L. (2015), ‘Deriving snow cover metrics for alaska from modis’, *Remote sensing* **7**(10), 12961–12985.
- Liston, G. E. (2004), ‘Representing subgrid snow cover heterogeneities in regional and global models’, *Journal of climate* **17**(6), 1381–1397.
- Liu, M., Xiong, C., Pan, J., Wang, T., Shi, J. & Wang, N. (2020), ‘High-resolution reconstruction of the maximum snow water equivalent based on remote sensing data in a mountainous area’, *Remote Sensing* **12**(3), 460.
- Longepe, N., Allain, S., Ferro-Famil, L., Pottier, E. & Durand, Y. (2009), ‘Snowpack characterization in mountainous regions using c-band sar data and a meteorological model’, *IEEE Transactions on Geoscience and Remote Sensing* **47**(2), 406–418.
- López-Burgos, V., Gupta, H. V. & Clark, M. (2013), ‘Reducing cloud obscuration of modis snow cover area products by combining spatio-temporal techniques with a probability of snow approach’, *Hydrology and Earth System Sciences* **17**(5), 1809.
- Lopez, P., Sirguey, P., Arnaud, Y., Pouyaud, B. & Chevallier, P. (2008), ‘Snow cover monitoring in the northern patagonia icefield using modis satellite images (2000–2006)’, *Global and Planetary Change* **61**(3-4), 103–116.
- Luce, C. H., Tarboton, D. G. & Cooley, K. R. (1998), ‘The influence of the spatial distribution of snow on basin-averaged snowmelt’, *Hydrological Processes* **12**(10-11), 1671–1683.
- MacDonald, L. & Stednick, J. (2003), ‘Forests and water: A state-of-the-art review for colorado’, *CWRRI Completion Report No. 196. Fort Collins, CO: Colorado State University. 65 p. .*
- Magagi, R. & Bernier, M. (2003), ‘Optimal conditions for wet snow detection using radarsat sar data’, *Remote Sensing of Environment* **84**(2), 221–233.
- Magnusson, J., Nævdal, G., Matt, F., Burkhart, J. F. & Winstral, A. (2020), ‘Improving hydropower inflow forecasts by assimilating snow data’, *Hydrology Research* **51**(2), 226–237.
- Mair, E., Bertoldi, G., Leitinger, G., Della Chiesa, S., Niedrist, G. & Tappeiner, U. (2013), ‘Esolip–estimate of solid and liquid precipitation at sub-daily time resolution by combining snow height and rain gauge measurements’, *Hydrology and Earth System Sciences Discussions* **10**(7), 8683–8714.
- Mair, E., Leitinger, G., Della Chiesa, S., Niedrist, G., Tappeiner, U. & Bertoldi, G. (2016), ‘A simple method to combine snow height and meteorological observations to estimate winter precipitation at sub-daily resolution’, *Hydrological Sciences Journal* **61**(11), 2050–2060.

- Malnes, E., Buanes, A., Nagler, T., Bippus, G., Gustafsson, D., Schiller, C., Metsämäki, S., Pulliainen, J., Luoju, K., Larsen, H. et al. (2015), ‘User requirements for the snow and land ice services–cryoland’, *The Cryosphere* **9**(3), 1191–1202.
- Margulis, S. A., Cortés, G., Giroto, M. & Durand, M. (2016), ‘A landsat-era sierra nevada snow reanalysis (1985–2015)’, *Journal of Hydrometeorology* **17**(4), 1203–1221.
- Margulis, S. A., Liu, Y. & Baldo, E. (2019), ‘A joint landsat-and modis-based reanalysis approach for midlatitude montane seasonal snow characterization’, *Frontiers in Earth Science* **7**, 272.
- Margulis, S. A., Wood, E. F. & Troch, P. A. (2006), ‘The terrestrial water cycle: Modeling and data assimilation across catchment scales’, *Journal of Hydrometeorology* **7**(3), 309–311.
- Marin, C., Bertoldi, G., Premier, V., Callegari, M., Brida, C., Hürkamp, K., Tschiersch, J., Zebisch, M. & Notarnicola, C. (2020), ‘Use of sentinel-1 radar observations to evaluate snowmelt dynamics in alpine regions’, *The Cryosphere* **14**(3), 935–956.
- Mark, A. F., Korsten, A. C., Guevara, D. U., Dickinson, K. J., Humar-Maegli, T., Michel, P., Halloy, S. R., Lord, J. M., Venn, S. E., Morgan, J. W. et al. (2015), ‘Ecological responses to 52 years of experimental snow manipulation in high-alpine cushionfield, old man range, south-central new zealand’, *Arctic, Antarctic, and Alpine Research* **47**(4), 751–772.
- Martinec, J. & Rango, A. (1981), ‘Areal distribution of snow water equivalent evaluated by snow cover monitoring’, *Water Resources Research* **17**(5), 1480–1488.
- Meløysund, V., Leira, B., Høiseth, K. V. & Lisø, K. R. (2007), ‘Predicting snow density using meteorological data’, *Meteorological Applications: A journal of forecasting, practical applications, training techniques and modelling* **14**(4), 413–423.
- Mendoza, P. A., Musselman, K. N., Revuelto, J., Deems, J. S., López-Moreno, J. I. & McPhee, J. (2020), ‘Interannual and seasonal variability of snow depth scaling behavior in a subalpine catchment’, *Water Resources Research* **56**(7), e2020WR027343.
- Mityók, Z. K., Bolton, D. K., Coops, N. C., Berman, E. E. & Senger, S. (2018), ‘Snow cover mapped daily at 30 meters resolution using a fusion of multi-temporal modis ndsi data and landsat surface reflectance’, *Canadian Journal of Remote Sensing* **44**(5), 413–434.
- Molotch, N. P. & Margulis, S. A. (2008), ‘Estimating the distribution of snow water equivalent using remotely sensed snow cover data and a spatially distributed snowmelt model: A multi-resolution, multi-sensor comparison’, *Advances in water resources* **31**(11), 1503–1514.

- Mott, R., Egli, L., Grünewald, T., Dawes, N., Manes, C., Bavay, M. & Lehning, M. (2011), ‘Micrometeorological processes driving snow ablation in an alpine catchment’, *The Cryosphere* **5**(4), 1083–1098.
- Mott, R., Vionnet, V. & Grünewald, T. (2018), ‘The seasonal snow cover dynamics: review on wind-driven coupling processes’, *Frontiers in Earth Science* **6**, 197.
- Murphy, B., Müller, S. & Yurchak, R. (2020), ‘Geostat-framework/pykrige: v1. 5.0’, *Version v1* **5**.
- Nagler, T. & Rott, H. (2000), ‘Retrieval of wet snow by means of multitemporal sar data’, *IEEE Transactions on Geoscience and Remote Sensing* **38**(2), 754–765.
- Nagler, T., Rott, H., Ripper, E., Bippus, G. & Hetzenecker, M. (2016), ‘Advancements for snowmelt monitoring by means of sentinel-1 sar’, *Remote Sensing* **8**(4), 348.
- Nijhawan, R., Das, J. & Raman, B. (2019), ‘A hybrid of deep learning and hand-crafted features based approach for snow cover mapping’, *International journal of remote sensing* **40**(2), 759–773.
- Niroumand-Jadidi, M., Santoni, M., Bruzzone, L. & Bovolo, F. (2020), ‘Snow cover estimation underneath the clouds based on multitemporal correlation analysis in historical time-series imagery’, *IEEE Transactions on Geoscience and Remote Sensing* .
- Nolin, A. W. (2010), ‘Recent advances in remote sensing of seasonal snow’, *Journal of Glaciology* **56**(200), 1141–1150.
- Notarnicola, C. (2020), ‘Hotspots of snow cover changes in global mountain regions over 2000–2018’, *Remote Sensing of Environment* **243**, 111781.
- Oaida, C. M., Reager, J. T., Andreadis, K. M., David, C. H., Levee, S. R., Painter, T. H., Bormann, K. J., Trangsrud, A. R., Giroto, M. & Famiglietti, J. S. (2019), ‘A high-resolution data assimilation framework for snow water equivalent estimation across the western united states and validation with the airborne snow observatory’, *Journal of Hydrometeorology* **20**(3), 357–378.
- Painter, T. (2018), ‘Aso l4 lidar snow depth 3m utm grid, version 1’, *Boulder, Colorado, USA: NASA National Snow and Ice Data Center Distributed Active Archive Center* **10**.
- Painter, T. H., Berisford, D. F., Boardman, J. W., Bormann, K. J., Deems, J. S., Gehrke, F., Hedrick, A., Joyce, M., Laidlaw, R., Marks, D. et al. (2016), ‘The airborne snow observatory: Fusion of scanning lidar, imaging spectrometer, and physically-based modeling for mapping snow water equivalent and snow albedo’, *Remote Sensing of Environment* **184**, 139–152.
- Painter, T. H., Rittger, K., McKenzie, C., Slaughter, P., Davis, R. E. & , J. (2009), ‘Retrieval of subpixel snow covered area, grain size, and albedo from modis’, *Remote Sensing of Environment* **113**(4), 868–879.

- Painter, T. H., Roberts, D. A., Green, R. O. & Dozier, J. (1998), ‘The effect of grain size on spectral mixture analysis of snow-covered area from aviris data’, *Remote Sensing of Environment* **65**(3), 320–332.
- Parajka, J. & Blöschl, G. (2006), ‘Validation of modis snow cover images over austria’.
- Parajka, J. & Blöschl, G. (n.d.), ‘Spatio-temporal combination of modis images—potential for snow cover mapping: Spatio-temporal combination of modis images’, *Water Resour. Res* **44**.
- Parajka, J., Pepe, M., Rampini, A., Rossi, S. & Blöschl, G. (2010), ‘A regional snow-line method for estimating snow cover from modis during cloud cover’, *Journal of Hydrology* **381**(3-4), 203–212.
- Picard, G., Sandells, M. & Löwe, H. (2018), ‘Smrt: An active–passive microwave radiative transfer model for snow with multiple microstructure and scattering formulations (v1. 0)’, *Geoscientific Model Development* **11**(7), 2763–2788.
- Poggio, L. & Gimona, A. (2015), ‘Sequence-based mapping approach to spatio-temporal snow patterns from modis time-series applied to scotland’, *International journal of applied earth observation and geoinformation* **34**, 122–135.
- Pomeroy, J. & Brun, E. (2001), Physical properties of snow, *in* H. G. Jones et al., ed., ‘Snow Ecology: An Interdisciplinary Examination of Snow-Covered Ecosystems’, Cambridge Univ. Press, Cambridge, U. K., pp. 45–126.
- Prein, A. F. & Gobiet, A. (2017), ‘Impacts of uncertainties in european gridded precipitation observations on regional climate analysis’, *International Journal of Climatology* **37**(1), 305–327.
- Premier, V., Marin, C., Notarnicola, C. & Bruzzone, L. (2021), A multisource statistical method to downscale snow cover fraction in mountain regions, *in* ‘IGARSS 2021’.
- Premier, V., Marin, C., Steger, S., Notarnicola, C. & Bruzzone, L. (2021), ‘A novel approach based on a hierarchical multiresolution analysis of optical time series to reconstruct the daily high-resolution snow cover area’, *IEEE Journal of Selected Topics in Applied Earth Observations and Remote Sensing* **14**(3), 9223–9240.
- Proksch, M., Mätzler, C., Wiesmann, A., Lemmetyinen, J., Schwank, M., Löwe, H. & Schneebeli, M. (2015), ‘Memls3&a: Microwave emission model of layered snowpacks adapted to include backscattering’, *Geoscientific Model Development* **8**(8), 2611–2626.
- Pulliainen, J., Luojus, K., Derksen, C., Mudryk, L., Lemmetyinen, J., Salminen, M., Ikonen, J., Takala, M., Cohen, J., Smolander, T. et al. (2020), ‘Patterns and trends of northern hemisphere snow mass from 1980 to 2018’, *Nature* **581**(7808), 294–298.
- Qegan, S. & Yu, J. J. (2001), ‘Filtering of multichannel sar images’, *IEEE Transactions on geoscience and remote sensing* **39**(11), 2373–2379.

- Raleigh, M., Lundquist, J. & Clark, M. (2015), ‘Exploring the impact of forcing error characteristics on physically based snow simulations within a global sensitivity analysis framework’, *Hydrology and Earth System Sciences* **19**(7), 3153–3179.
- Rappl, A., Wetzel, K.-F., Büttner, G. & Scholz, M. (2010), ‘Scientific reports dye tracer investigations at the partnach spring (german alps)’, *Hydrologie und Wasserbewirtschaftung* **54**(4), 220.
- Rees, W. G. (2005), *Remote sensing of snow and ice*, CRC press.
- Revuelto, J., Alonso-González, E., Gascoin, S., Rodríguez-López, G. & López-Moreno, J. I. (2021), ‘Spatial downscaling of modis snow cover observations using sentinel-2 snow products’, *Remote Sensing* **13**(22), 4513.
- Riggs, G. A., Hall, D. K. & Román, M. O. (2015), ‘Modis snow products collection 6 user guide’, *National Snow and Ice Data Center: Boulder, CO, USA* p. 66.
- Rinaldo, A., Beven, K. J., Bertuzzo, E., Nicotina, L., Davies, J., Fiori, A., Russo, D. & Botter, G. (2011), ‘Catchment travel time distributions and water flow in soils’, *Water resources research* **47**(7).
- Rittger, K., Bair, E. H., Kahl, A. & Dozier, J. (2016), ‘Spatial estimates of snow water equivalent from reconstruction’, *Advances in water resources* **94**, 345–363.
- Rodell, M. & Houser, P. (2004), ‘Updating a land surface model with modis-derived snow cover’, *Journal of Hydrometeorology* **5**(6), 1064–1075.
- Rott, H. & Mätzler, C. (1987), ‘Possibilities and limits of synthetic aperture radar for snow and glacier surveying’, *Annals of Glaciology* **9**, 195–199.
- Rott, H., Yueh, S. H., Cline, D. W., Duguay, C., Essery, R., Haas, C., Heliere, F., Kern, M., Macelloni, G., Malnes, E. et al. (2010), ‘Cold regions hydrology high-resolution observatory for snow and cold land processes’, *Proceedings of the IEEE* **98**(5), 752–765.
- Salomonson, V. V. & Appel, I. (2004), ‘Estimating fractional snow cover from modis using the normalized difference snow index’, *Remote sensing of environment* **89**(3), 351–360.
- Salomonson, V. V. & Appel, I. (2006), ‘Development of the aqua modis ndsi fractional snow cover algorithm and validation results’, *IEEE Transactions on geoscience and remote sensing* **44**(7), 1747–1756.
- Sayer, A., Hsu, N. & Bettenhausen, C. (2015), ‘Implications of modis bow-tie distortion on aerosol optical depth retrievals, and techniques for mitigation.’, *Atmospheric Measurement Techniques Discussions* **8**(12).
- Schattan, P., Köhli, M., Schrön, M., Baroni, G. & Oswald, S. E. (2019), ‘Sensing area-average snow water equivalent with cosmic-ray neutrons: The influence of fractional snow cover’, *Water Resources Research* **55**(12), 10796–10812.

- Schmid, L., Heilig, A., Mitterer, C., Schweizer, J., Maurer, H., Okorn, R. & Eisen, O. (2014), ‘Continuous snowpack monitoring using upward-looking ground-penetrating radar technology’, *Journal of Glaciology* **60**(221), 509–525.
- Schneider, D., Molotch, N. P., Deems, J. S. & Painter, T. H. (2021), ‘Analysis of topographic controls on depletion curves derived from airborne lidar snow depth data’, *Hydrology Research* **52**(1), 253–265.
- Schneider, E. E., Affleck, D. L. & Larson, A. J. (2019), ‘Tree spatial patterns modulate peak snow accumulation and snow disappearance’, *Forest Ecology and Management* **441**, 9–19.
- Schratz, P., Muenchow, J., Iturrutxa, E., Richter, J. & Brenning, A. (2019), ‘Hyperparameter tuning and performance assessment of statistical and machine-learning algorithms using spatial data’, *Ecological Modelling* **406**, 109–120.
- Seibert, J., Jenicek, M., Huss, M., Ewen, T. & Viviroli, D. (2021), Snow and ice in the hydrosphere, in ‘Snow and ice-related hazards, risks, and disasters’, Elsevier, pp. 93–135.
- Selkowitz, D. J., Forster, R. R. & Caldwell, M. K. (2014), ‘Prevalence of pure versus mixed snow cover pixels across spatial resolutions in alpine environments’, *Remote Sensing* **6**(12), 12478–12508.
- Servén, D. & Brummitt, C. (2018), ‘pygam: generalized additive models in python’, *Zenodo*. DOI **10**.
- Sevruk, B., Ondrás, M. & Chvíla, B. (2009), ‘The wmo precipitation measurement intercomparisons’, *Atmospheric Research* **92**(3), 376–380.
- Shafer, B., Jones, E. B. & Frick, D. M. (1982), ‘Snowmelt runoff modeling in simulation and forecasting modes with the martinec-mango model’.
- Shi, J. & Dozier, J. (1993), ‘Measurements of snow-and glacier-covered areas with single-polarization sar’, *Annals of Glaciology* **17**, 72–76.
- Shi, J. & Dozier, J. (1995), ‘Inferring snow wetness using C-band data from SIR-C’s polarimetric synthetic aperture radar’, *IEEE Transactions on Geoscience and Remote Sensing* (4), 905–914.
- Shi, J., Dozier, J. & Rott, H. (1994), ‘Snow mapping in alpine regions with synthetic aperture radar’, *IEEE Transactions on Geoscience and Remote Sensing* **32**(1), 152–158.
- Slater, A., Barrett, A., Clark, M., Lundquist, J. & Raleigh, M. (2013), ‘Uncertainty in seasonal snow reconstruction: Relative impacts of model forcing and image availability’, *Advances in water resources* **55**, 165–177.
- Small, D. (2011), ‘Flattening gamma: Radiometric terrain correction for sar imagery’, *IEEE Transactions on Geoscience and Remote Sensing* **49**(8), 3081–3093.

- Stähli, M., Stacheder, M., Gustafsson, D., Schlaeger, S., Schneebeli, M. & Brandelik, A. (2004), ‘A new in situ sensor for large-scale snow-cover monitoring’, *Annals of Glaciology* **38**, 273–278.
- Starr, G. & Oberbauer, S. F. (2003), ‘Photosynthesis of arctic evergreens under snow: implications for tundra ecosystem carbon balance’, *Ecology* **84**(6), 1415–1420.
- Stethem, C., Jamieson, B., Schaerer, P., Liverman, D., Germain, D. & Walker, S. (2003), ‘Snow avalanche hazard in Canada—a review’, *Natural Hazards* **28**(2-3), 487–515.
- Strasser, U., Bernhardt, M., Weber, M., Liston, G. & Mauser, W. (2008), ‘Is snow sublimation important in the alpine water balance?’, *The Cryosphere* **2**(1), 53–66.
- Strasser, U., Warscher, M. & Liston, G. E. (2011), ‘Modeling snow–canopy processes on an idealized mountain’, *Journal of Hydrometeorology* **12**(4), 663–677.
- Tappeiner, U., Tappeiner, G., Aschenwald, J., Tasser, E. & Ostendorf, B. (2001), ‘Gis-based modelling of spatial pattern of snow cover duration in an alpine area’, *Ecological Modelling* **138**(1-3), 265–275.
- Techel, F. & Pielmeier, C. (2011), ‘Point observations of liquid water content in wet snow—investigating methodical, spatial and temporal aspects’, *The Cryosphere* **5**(2), 405–418.
- Thirel, G., Salamon, P., Burek, P. & Kalas, M. (2013), ‘Assimilation of modis snow cover area data in a distributed hydrological model using the particle filter’, *Remote Sensing* **5**(11), 5825–5850.
- Thorp, J. M. & Scott, B. C. (1982), ‘Preliminary calculations of average storm duration and seasonal precipitation rates for the northeast sector of the united states’, *Atmospheric Environment (1967)* **16**(7), 1763–1774.
- Tran, H., Nguyen, P., Ombadi, M., Hsu, K.-l., Sorooshian, S. & Qing, X. (2019), ‘A cloud-free modis snow cover dataset for the contiguous united states from 2000 to 2017’, *Scientific data* **6**, 180300.
- Tsang, L., Durand, M., Derksen, C., Barros, A. P., Kang, D.-H., Lievens, H., Marshall, H.-P., Zhu, J., Johnson, J., King, J. et al. (2021), ‘Global monitoring of snow water equivalent using high frequency radar remote sensing’, *The Cryosphere Discussions* pp. 1–57.
- Tuia, D., Persello, C. & Bruzzone, L. (2016), ‘Domain adaptation for the classification of remote sensing data: An overview of recent advances’, *IEEE geoscience and remote sensing magazine* **4**(2), 41–57.
- Ulaby, F., Moore, R. & Fung, A. (2015), ‘Microwave remote sensing active and passive’.
- Ulaby, F. T., Dubois, P. C. & Van Zyl, J. (1996), ‘Radar mapping of surface soil moisture’, *Journal of hydrology* **184**(1-2), 57–84.

- Ulaby, F. T., Moore, R. K. & Fung, A. K. (1981), ‘Microwave remote sensing: Active and passive. volume 1-microwave remote sensing fundamentals and radiometry’.
- Unsworth, M. H. & Monteith, J. (1975), ‘Long-wave radiation at the ground i. angular distribution of incoming radiation’, *Quarterly Journal of the Royal Meteorological Society* **101**(427), 13–24.
- Veyssi re, G., Karbou, F., Morin, S., Lafaysse, M. & Vionnet, V. (2018), ‘Evaluation of sub-kilometric numerical simulations of c-band radar backscatter over the french alps against sentinel-1 observations’, *Remote Sensing* **11**(1), 8.
- Vionnet, V., Brun, E., Morin, S., Boone, A., Faroux, S., Le Moigne, P., Martin, E. & Willemet, J.-M. (2012), ‘The detailed snowpack scheme crocus and its implementation in surfex v7. 2’, *Geoscientific Model Development* **5**(3), 773–791.
- Vionnet, V., Marsh, C. B., Menounos, B., Gascoin, S., Wayand, N. E., Shea, J., Mukherjee, K. & Pomeroy, J. W. (2020), ‘Multi-scale snowdrift-permitting modelling of mountain snowpack’, *The Cryosphere Discussions* pp. 1–43.
- Viviroli, D. & Weingartner, R. (2004), ‘The hydrological significance of mountains: from regional to global scale’.
- Viviroli, D., Weingartner, R. & Messerli, B. (2003), ‘Assessing the hydrological significance of the world’s mountains’, *Mountain research and Development* **23**(1), 32–40.
- Walters, R. D., Watson, K. A., Marshall, H.-P., McNamara, J. P. & Flores, A. N. (2014), ‘A physiographic approach to downscaling fractional snow cover data in mountainous regions’, *Remote sensing of environment* **152**, 413–425.
- Warscher, M., Marke, T. & Strasser, U. (2021), ‘Operational and experimental snow observation systems in the upper rofental: data from 2017–2020’, *Earth System Science Data Discussions* pp. 1–24.
- Wehren, B., Weingartner, R., Sch dler, B. & Viviroli, D. (2010), ‘General characteristics of alpine waters’, *Alpine waters* pp. 17–58.
- Wever, N., Fierz, C., Mitterer, C., Hirashima, H. & Lehning, M. (2014), ‘Solving richards equation for snow improves snowpack meltwater runoff estimations in detailed multi-layer snowpack model’, *The Cryosphere* **8**(1), 257–274.
- Wever, N., Schmid, L., Heilig, A., Eisen, O., Fierz, C. & Lehning, M. (2015), ‘Verification of the multi-layer snowpack model with different water transport schemes’, *The Cryosphere* **9**(6), 2271–2293.
- Winther, J.-G. & Hall, D. K. (1999), ‘Satellite-derived snow coverage related to hydropower production in norway: Present and future’, *International Journal of Remote Sensing* **20**(15-16), 2991–3008.
- Wood, S. N. (2017), *Generalized additive models: an introduction with R*, CRC press.

- WSL Institute for Snow and Avalanche Research SLF (2015), ‘WFJ_MOD: Meteorological and snowpack measurements from Weissfluhjoch, Davos, Switzerland’’.
URL: <https://www.envidat.ch/dataset/10-16904-1>
- Yang, K., Musselman, K. N., Rittger, K., Margulis, S. A., Painter, T. H. & Molotch, N. P. (2022), ‘Combining ground-based and remotely sensed snow data in a linear regression model for real-time estimation of snow water equivalent’, *Advances in Water Resources* **160**, 104075.
- Zhang, H., Zhang, F., Zhang, G., Che, T., Yan, W., Ye, M. & Ma, N. (2019), ‘Ground-based evaluation of modis snow cover product v6 across china: Implications for the selection of ndsi threshold’, *Science of the Total Environment* **651**, 2712–2726.
- Zhang, T. (2005), ‘Influence of the seasonal snow cover on the ground thermal regime: An overview’, *Reviews of Geophysics* **43**(4).
- Zupanc, A. (2017), ‘Improving cloud detection with machine learning’, *Accessed: Oct 10*, 2019.

Appendix A

Supplementary Material to Chapter 4

A.1 In-situ snow measurements

The state characterization is done by observing available SWE or SD in-situ measurements. For the South Fork catchment, SWE continuous measurements are available for 7 different sites. As shown in Fig. 4.4a, only one station is inside the considered area, i.e. the Volcanic Knob station (VLC). However, we considered also the stations in the surrounding area to smooth out possible sensor errors or redistribution effects.

In the Schnals catchment, SWE continuous records are available only for the location Bella Vista. For this reason, the decision on the catchment state is based on the SD records available for 5 stations (see Fig. 4.4b). Three stations are inside the study area and the remaining ones are very close to the study area.

Note that for the same catchment, all the stations show a coherent pattern, meaning that we can consider the catchment subjected to the same major weather forcings.

In Fig. A.1 we also report the location of some of the manual SWE observations collected internally by Eurac Research (Institute for Earth Observation) for the Schnals catchment. These few points have been used in Fig. 4.10 to show some examples of reconstructed SWE trend and its behaviour against the manual measurements. For an overview of the location of all the collected manual observations used to compute the performances of the approach, see Fig. 4.4b.

A.2 Degree day estimation

The degree day (DD) is estimated starting from the available in-situ temperature observations for both catchments. Regarding the South Fork catchment, the temperature is available in 11 different stations located within a radius of around 15 km from the study area (see Fig. 4.4a). Due to the presence of some gaps in the data, we excluded from the computation of the DD the station "RKC" for season 2018/19, "WWC" for 2019/20 and "DKY", "VLC", and "UBC" for 2020/21. For the Schnals catchment, the temperature is available in 15 different locations within

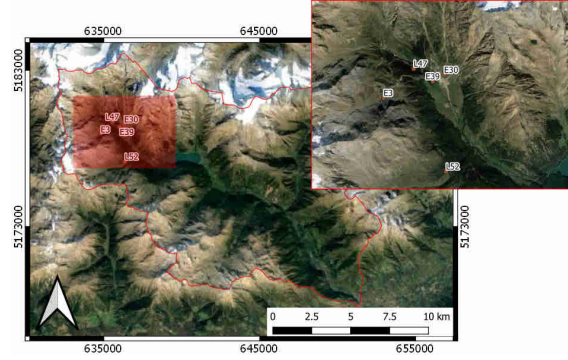


Figure A.1: Overview of the measurements ((©)2022 Google Maps).

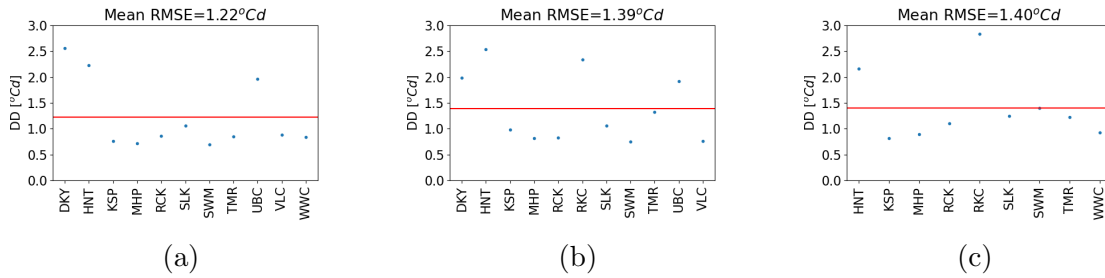


Figure A.2: Leave-one-out cross validation results for the South Fork catchment for the hydrological seasons a) 2018/19, b) 2019/20 and c) 2020/21.

a maximum distance of around 10 km (see Fig. 4.4b). Once the DD is computed for each station through Eq. 4.2, the DD is spatially interpolated with the kriging routine as explained in Sec. 4.2.3. The goodness of the spatial interpolation is tested through a leave one out (LOO) cross validation. The results in terms of root mean square error (RMSE) are reported in Fig. A.2 for South Fork and in Fig. A.3 for Schnals, showing a mean RMSE that never exceeds 1.5°Cd .

A.3 SWE results for the South Fork catchment

Fig. A.4 shows the SWE maps derived with the proposed method, the ASO reference product and the bias calculated as difference between the proposed and the reference

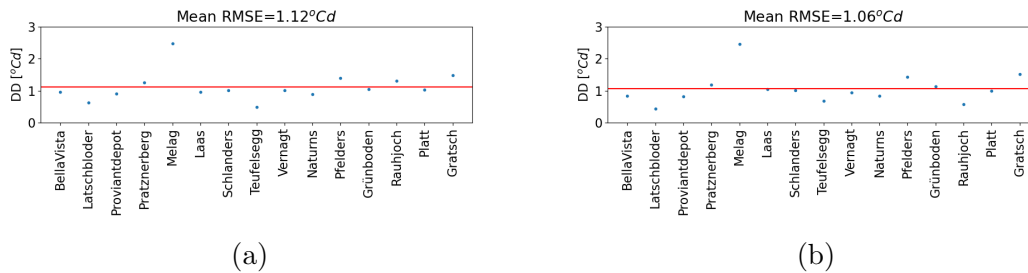


Figure A.3: Leave-one-out cross validation results for the Schnals catchment for the hydrological seasons a) 2019/20 and b) 2020/21).

maps.

Fig. A.5 shows the total amount of SWE calculated for different elevation, slope and aspect bands for the 12 dates when also the ASO product is available. We can notice a general good agreement showing that the proposed method is able to represent the typical geomorphological variability of the snow processes.

Fig. A.6 shows the boxplots relative to the total amount of SWE calculated for different elevation, slope and aspect bands for the 12 dates when also the ASO product is available. We remind that a boxplot represents the Interquartile Range (IQR) and is composed by the median (orange line), the first quartile Q1 (or 25th percentile) and the third quartile Q3 (or 75th percentile). The whiskers show the "minimum" ($Q1 - 1.5 * IQR$) and the "maximum" ($Q3 + 1.5 * IQR$). In this representation we omit the outliers.

**DOCTORAL PROGRAM IN
INFORMATION AND COMMUNICATION TECHNOLOGY**

Doctoral candidate

Valentina Premier

Cycle	34th Cycle
Thesis	Development of Novel Approaches to Snow Parameter Retrieval in Alpine Areas by Using Multi-temporal and Multi-sensor Remote Sensing Images
Advisor	Lorenzo Bruzzone (RSLab, University of Trento)
Co-advisor	Carlo Marin (Institute for Earth Observation, Eurac Research) Claudia Notarnicola (Institute for Earth Observation, Eurac Research)

1. List of publications

C. Marin, G. Bertoldi, **V. Premier**, M. Callegari, C. Brida, K. Hürkamp, J. Tschiersch, M. Zebisch, C. Notarnicola, *Use of Sentinel-1 radar observations to evaluate snowmelt dynamics in alpine regions* in The Cryosphere, v. 14, n.3 (2020), p. 935-956.

P. P. Ebner, F. Koch, **V. Premier**, C. Marin, F. Hanzer, C. M. Carmagnola, H. Francois, D. Gunther, F. Monti, O. Hargoaa, U. Strasser, S. Morin, M. Lehning, *Evaluating a prediction system for snow management* in The Cryosphere, v. 15, n.8 (2021), p. 3949-3973.

X. Wu, K. Naegeli, **V. Premier**, C. Marin, D. Ma, J. Wang, S. Wunderle, *Evaluation of snow extent time series derived from Advanced Very High Resolution Radiometer global area coverage data (1982–2018) in the Hindu Kush Himalayas* in The Cryosphere, vol. 15, n. 9 (2021), p. 4261-4279.

V. Premier, C. Marin, S. Steger, C. Notarnicola, L. Bruzzone, *A Novel Approach Based on a Hierarchical Multiresolution Analysis of Optical Time Series to Reconstruct the Daily High-Resolution Snow Cover Area* in IEEE Journal of Selected Topics in Applied Earth Observations and Remote Sensing, vol. 14 (2021), p. 9223-9240.

F. Hofmeister, L. F. Arias-Rodriguez, **V. Premier**, C. Marin, C. Notarnicola, M. Disse, G. Chiogna, *Intercomparison of Sentinel-2 and modelled snow cover maps in a high-elevation Alpine catchment* in Journal of Hydrology, v. 15 (2022), p. 100-123.

Submitted Papers

V. Premier, C. Marin, G. Bertoldi, R. Barella, C. Notarnicola, L. Bruzzone, *Exploring the Use of Multi-source High-Resolution Satellite Data for Snow Water Equivalent Reconstruction over Mountainous Catchments* in The Cryosphere.

Conference Papers

C. Marin, G. Bertoldi, **V. Premier**, M. Callegari, C. Brida, K. Hürkamp, J. Tschiersch, M. Zebisch, C. Notarnicola, *The Relationship Between the Multi-Temporal Sentinel-1 Backscattering and the Snow Melting Dynamics in Alpine Regions*, 13th European Conference on Antennas and Propagation (EuCAP 2019), Krakow, Poland, 31 March – 5 April 2019.

M. Pasian, P. F. Espín-López, **V. Premier**, C. Notarnicola, C. Marin, *Identification of multi-temporal snow melting patterns with microwave radars*, 14th European Conference on Antennas and Propagation (EuCAP 2020), online, 15-20 March 2020.

V. Premier, C. Marin, C. Notarnicola, L. Bruzzone, *A multisource statistical method to downscale snow cover fraction in mountain regions*, IEEE International Geoscience and Remote Sensing Symposium (IGARSS 2021), online, 12-16 July 2021.

M. Pasian, M. Lodigiani, C. Marin, **V. Premier**, C. Notarnicola, *Numerical Investigation on the Effect of the Snowpack Surface Roughness on the Radar Echo*, IEEE International Geoscience and Remote Sensing Symposium (IGARSS 2021), online, 12-16 July 2021.

2. Research/study activities

Research projects

- Participation in the H2020 PROSNOW research project:
 - Evaluation of hindcast simulations through remotely-sensed observations
 - Classification of Sentinel-2 data with machine learning algorithms
- Participation in the ESA CCI research project:
 - Set up of the reference dataset (high-resolution optical data – Landsat missions) by using state-of-the-art algorithms
 - Validation activity
 - Intercomparison of the validated product
- Participation in the ACR Water research project (Legge 14):
 - Classification of Sentinel-2 data with machine learning algorithms
- Participation in the SnowTinel research project (SNSF):
 - Understanding the interactions of the radar signal with the wet snowpack temporal evolution
 - Integration with physically distributed models
 - Monitoring of SWE and snowmelt runoff in mountain catchments.

Conferences

- Participation at the ESA Living Planet Symposium (13-17 May 2019, Milan – Italy) with an oral presentation titled *Identifying snow melt dynamics by exploiting multi-temporal Sentinel-1 backscattering*, V. Premier, G. Bertoldi, M. Callegari, C. Brida, K. Hürkamp, J. Tschiersch, M. Zebisch, C. Notarnicola, L. Bruzzone, C. Marin
- Participation at SnowHydro (28-31 January 2020) with an oral presentation titled *Development of a novel approach for snowmelt monitoring in alpine areas by using multi-temporal and multi-sensor remote sensing imagery*, V. Premier, C. Marin, G. Bertoldi, C. Notarnicola, L. Bruzzone
- Participation at IGARSS (12-16 July 2021, online) with an oral presentation titled *A multisource statistical method to downscale snow cover fraction in mountain regions*, V. Premier, C. Marin, C. Notarnicola, L. Bruzzone

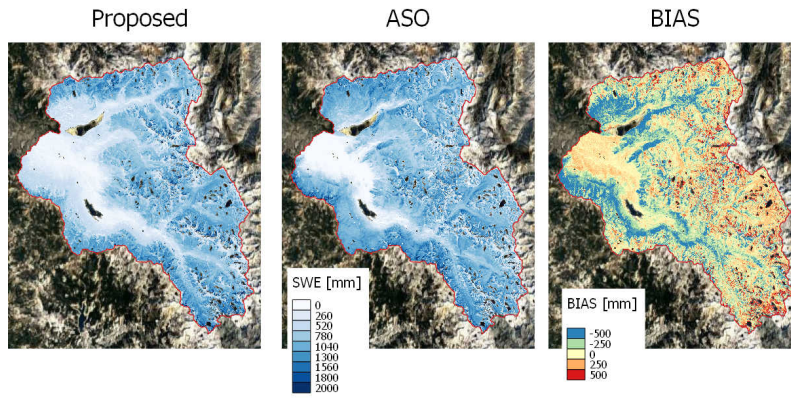
- Participation at SnowHydro (1-4 February 2022, online) with an oral presentation titled *A multisource approach to reconstruct high-resolution daily SWE estimates during the melting on mountainous catchments*, V. Premier, C. Marin, G. Bertoldi, C. Notarnicola, L. Bruzzone

Other Conferences as Co-author

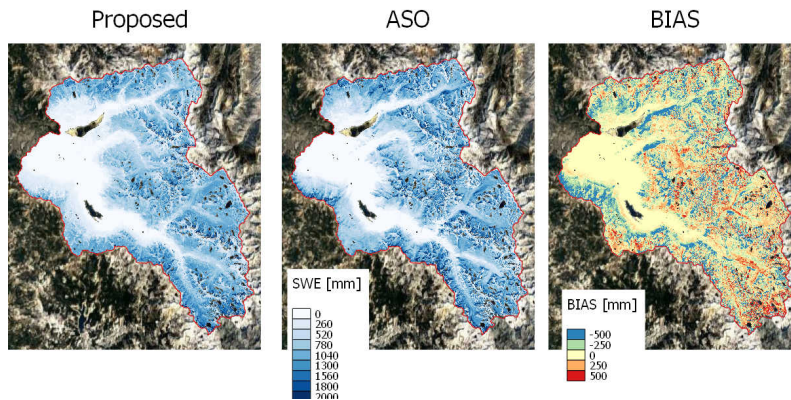
- A. Jacob, A. Bertone, R. Barella, M. Callegari, G. Cuzzo, L. De Gregorio, C. Kofler, C. Marin, C. Notarnicola, V. Premier, R. Sonnenschein, S. Steger, M. Zebisch (2019). *Machine Learning in Earth Observation: examples from the daily work at the Institute for Earth Observation*. In Davinci: Know How Transfer Event Artificial Intelligence/Machine Learning 4th Meeting.
- M. Matiu, M. Petitta, C. Notarnicola, V. Premier, M. Zebisch (2019). *Future snow cover in the alps: Using MODIS satellite observations to bias correct snow cover from the EURO-CORDEX regional climate model ensemble*. In International Mountain Conference.
- M. Matiu, M. Petitta, C. Notarnicola, V. Premier, M. Zebisch (2019, January). *Present and future snow cover in the alps: Using MODIS satellite observations to evaluate and bias correct the EURO-CORDEX regional climate model ensemble*. In Geophysical Research Abstracts (Vol. 21).
- K. Naegeli, N. Rietze, J. Franke, M. Stengel, C. Neuhaus, X. Wu, C. Marin, V. Premier, G. Schwaizer, Wunderle, S. (2021, April). *Long-term spatio-temporal seasonal snow cover variability in the Hindu Kush Himalaya*. In EGU General Assembly Conference Abstracts (pp. EGU21-14693).
- F. Hofmeister, L. F. Arias-Rodriguez, M. Borga, V. Premier, C. Marin, C. Notarnicola, M. Disse, G. Chiogna (2021, April). *Generation of a high-resolution snow cover dataset from Sentinel-2 images for snow model calibration*. In EGU General Assembly Conference Abstracts (pp. EGU21-16016).
- F. Hanzer, D. Günther, U. Strasser, V. Premier, M. Callegari, C. Marin, C. Notarnicola (2020, May). *Process-based simulation of snow cover evolution in ski resorts using the AMUNDSEN model: results and validation*. In EGU General Assembly Conference Abstracts (p. 17783).

Study activities

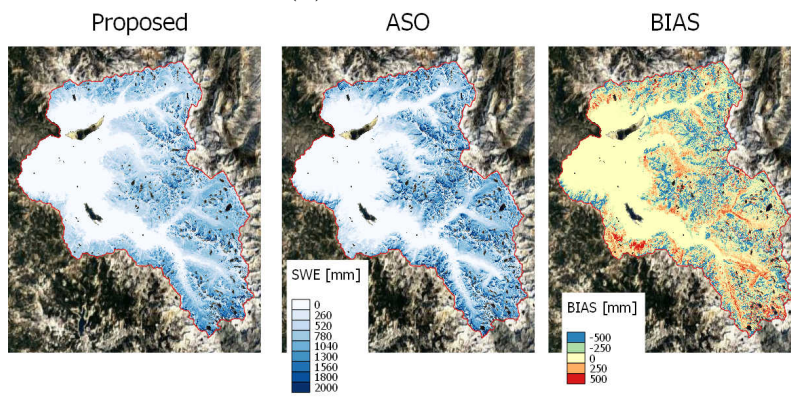
- Participation at the 6th Snow Science Winter School in Grenoble (16-22 February 2020)
- Participation at the GEOframe Winter School 2021 in Trento (7-16 January 2021)



(a) 17th March 2019.

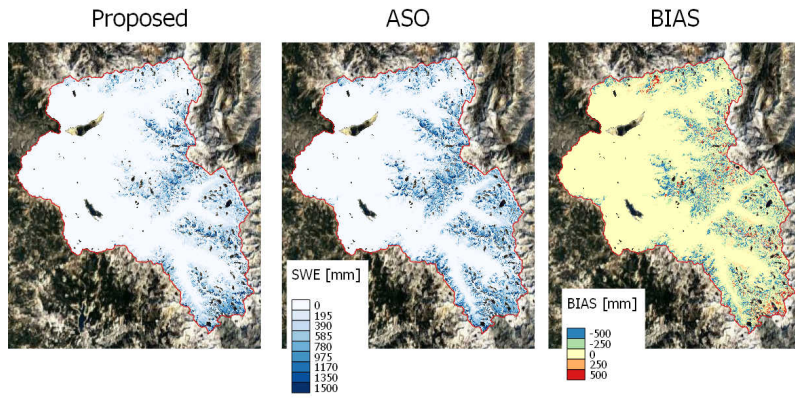


(b) 2nd May 2019.

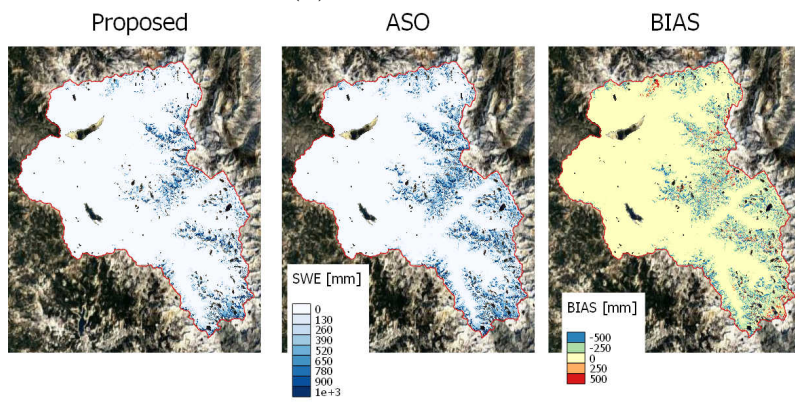


(c) 9th June 2019.

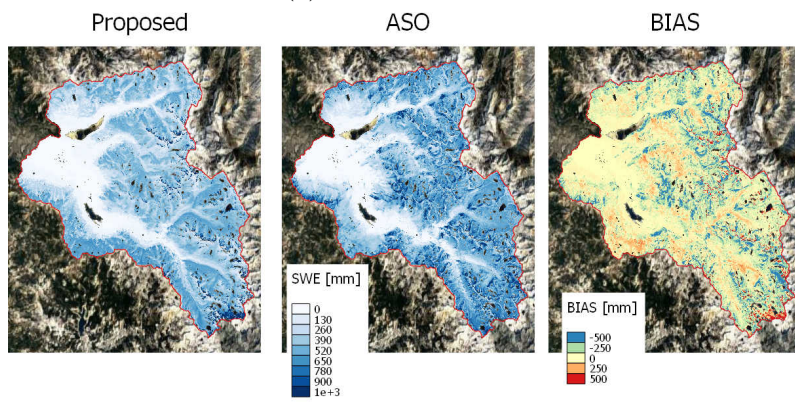
Figure A.4: Proposed SWE (left), ASO SWE (centre) and bias (right) for the 12 analyzed dates over the three hydrological season (2018-2021) for the South Fork catchment. (©2022 Google Maps)



(d) 4th July 2019.

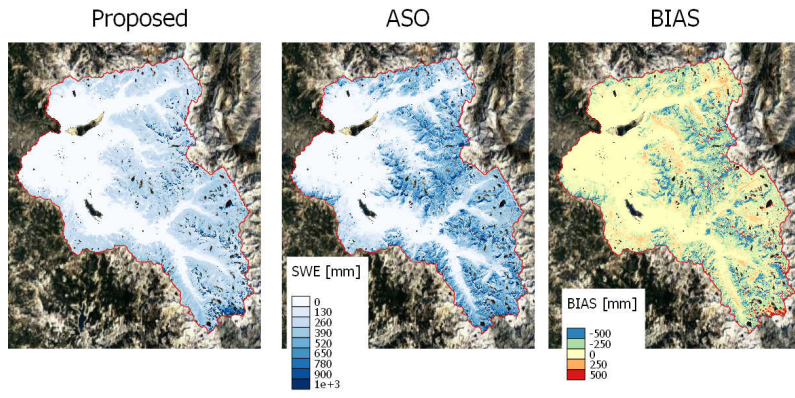


(e) 14th July 2019.

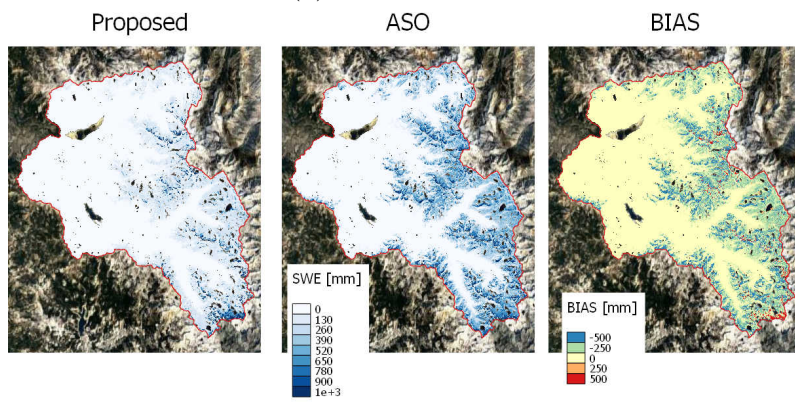


(f) 15th April 2020.

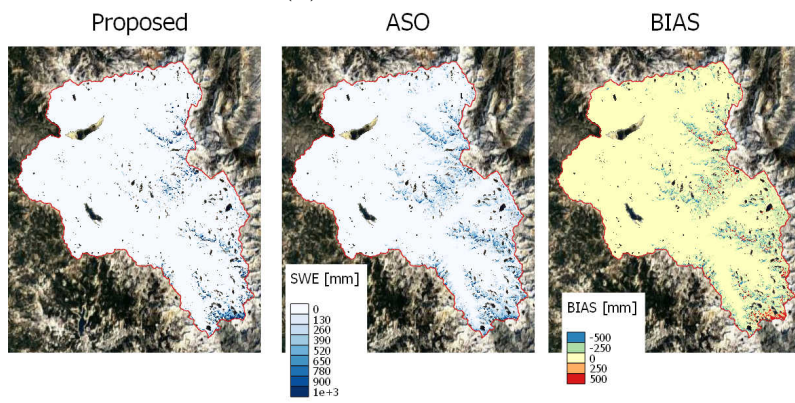
Figure A.4: Proposed SWE (left), ASO SWE (centre) and bias (right) for the 12 analyzed dates over the three hydrological season (2018-2021) for the South Fork catchment (cont.). (©2022 Google Maps)



(g) 5th May 2020.

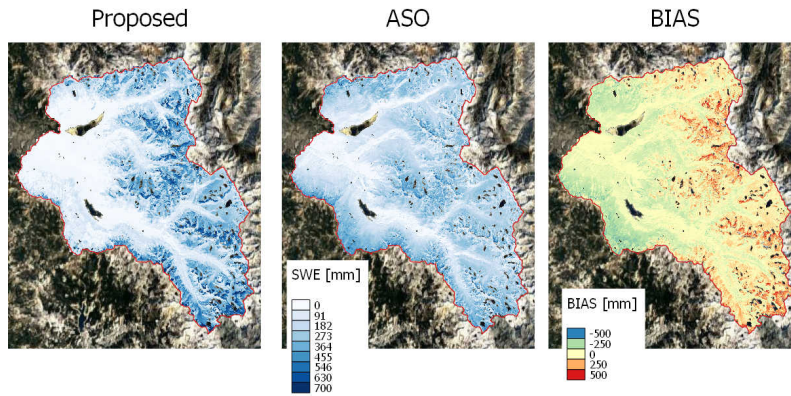


(h) 23th May 2020.

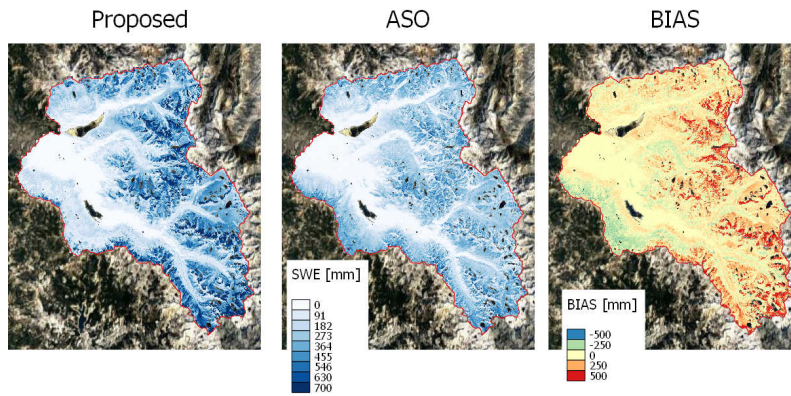


(i) 8th June 2020.

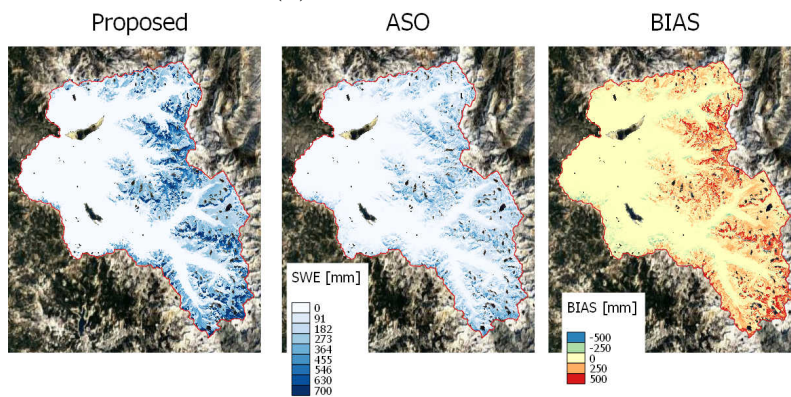
Figure A.4: Proposed SWE (left), ASO SWE (centre) and bias (right) for the 12 analyzed dates over the three hydrological season (2018-2021) for the South Fork catchment (cont.). (©2022 Google Maps)



(j) 26th February 2021.

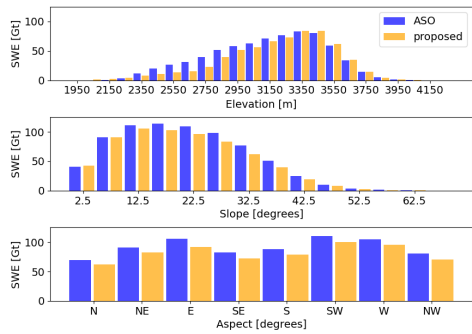


(k) 31st March 2021.

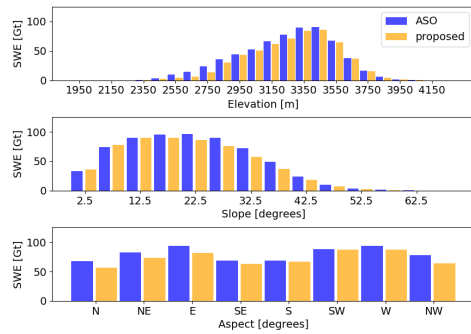


(l) 3rd May 2021.

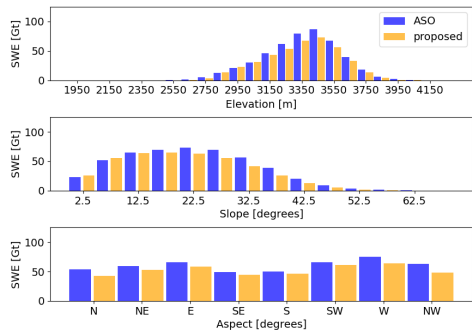
Figure A.4: Proposed SWE (left), ASO SWE (centre) and bias (right) for the 12 analyzed dates over the three hydrological season (2018-2021) for the South Fork catchment (cont.). (©2022 Google Maps)



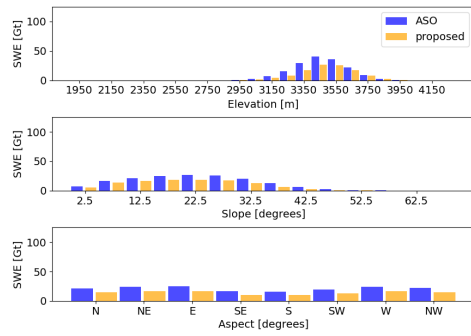
(a) 17th March 2019.



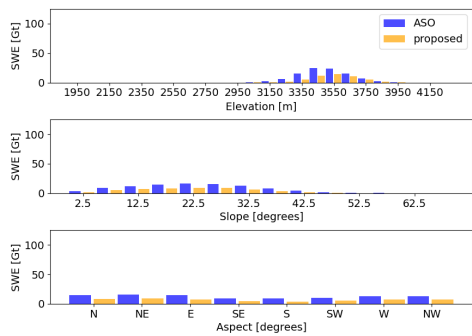
(b) 2nd May 2019.



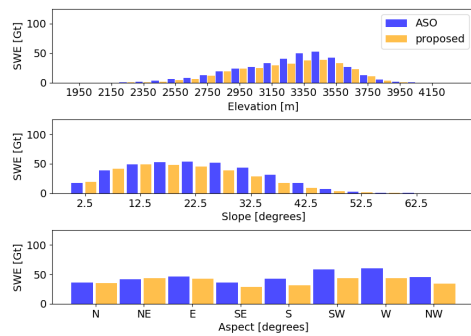
(c) 9th June 2019.



(d) 4th July 2019.

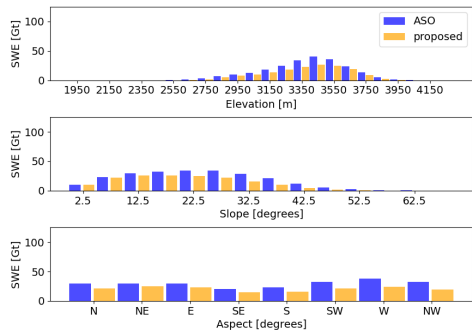


(e) 14th July 2019.

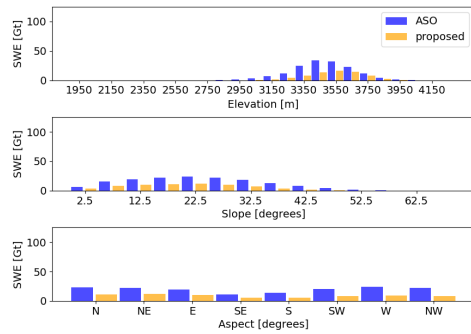


(f) 15th April 2020.

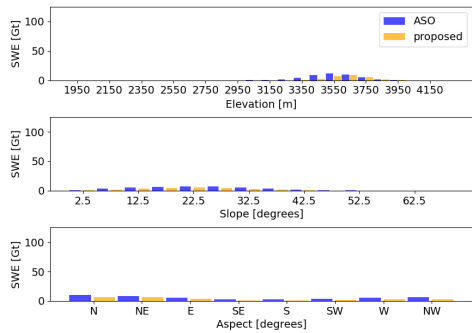
Figure A.5: Total SWE [Gt] distributed for each elevation, slope and aspect belt. The proposed product (in yellow) is evaluated against ASO (in blue) for the 12 analyzed dates over the three hydrological season (2018-2021) for the South Fork catchment.



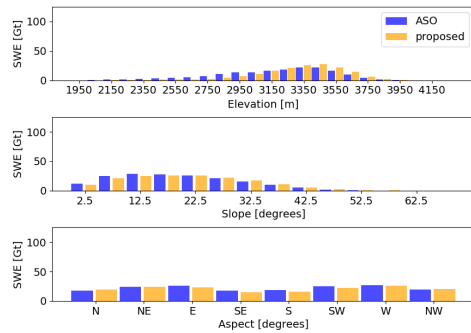
(g) 5th May 2020.



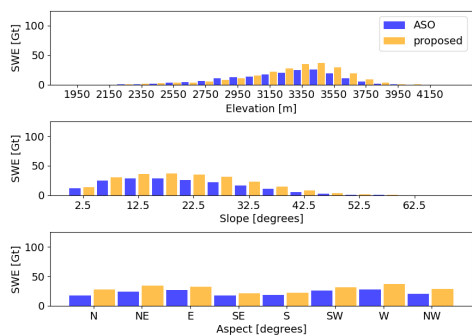
(h) 23th May 2020.



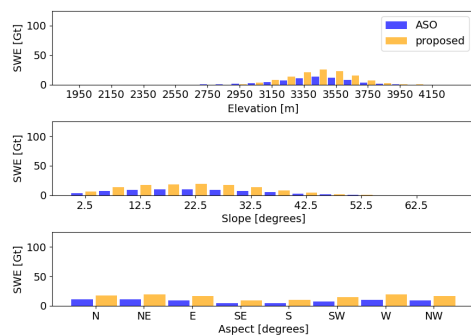
(i) 8th June 2020.



(j) 26th February 2021.

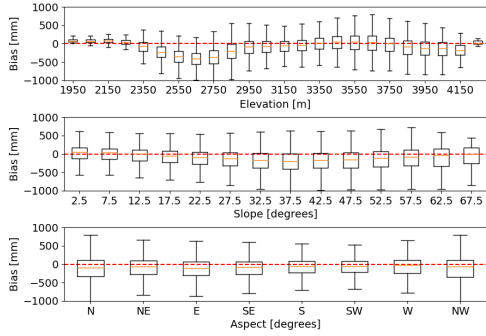


(k) 31st March 2021.

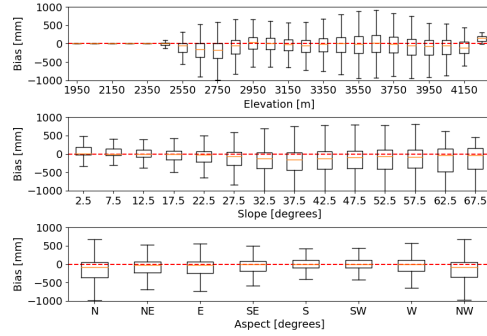


(l) 3rd May 2021.

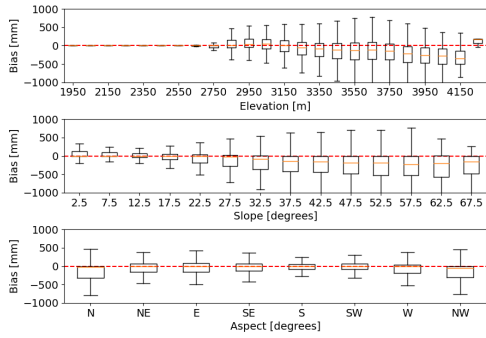
Figure A.5: Total SWE [Gt] distributed for each elevation, slope and aspect belt. The proposed product (in yellow) is evaluated against ASO (in blue) for the 12 analyzed dates over the three hydrological season (2018-2021) for the South Fork catchment (cont.).



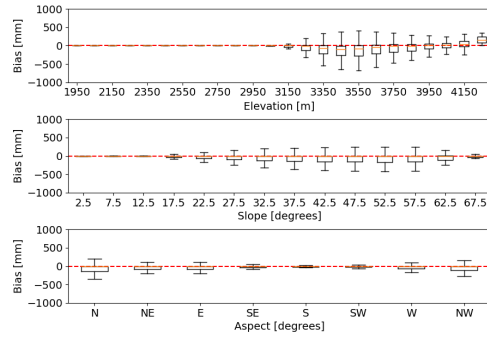
(a) 17th March 2019.



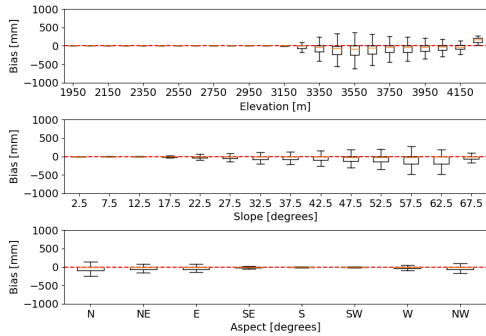
(b) 2nd May 2019.



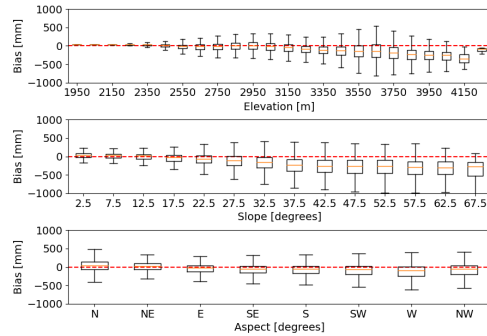
(c) 9th June 2019.



(d) 4th July 2019.

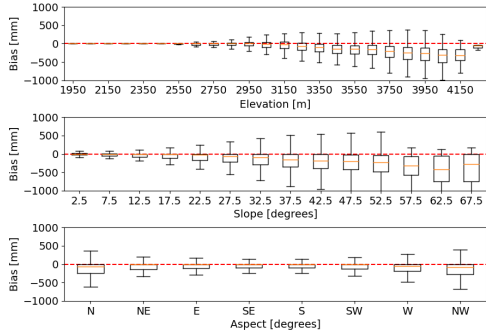


(e) 14th July 2019.

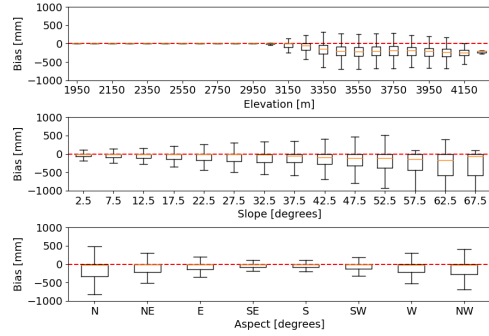


(f) 15th April 2020.

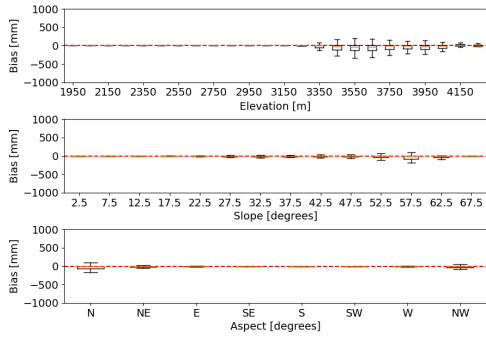
Figure A.6: Boxplots of the bias calculated as the SWE generated by the proposed approach minus the ASO product for each elevation, slope and aspect belt. The results are represented for the 12 analyzed dates over the three hydrological season (2018-2021) for the South Fork catchment.



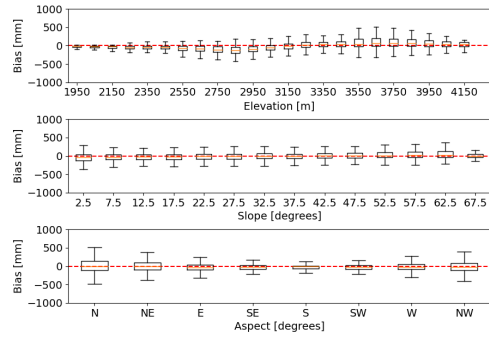
(g) 5th May 2020.



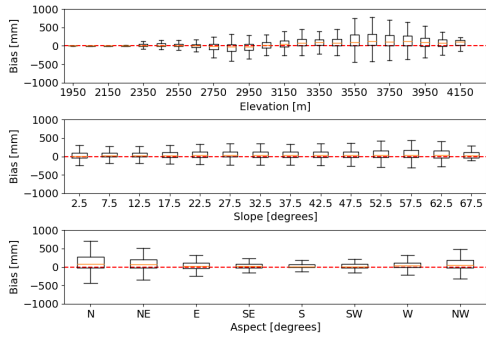
(h) 23th May 2020.



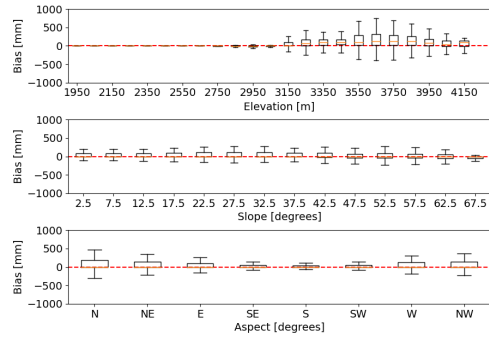
(i) 8th June 2020.



(j) 26th February 2021.



(k) 31st March 2021.



(l) 3rd May 2021.

Figure A.6: Boxplots of the bias calculated as the SWE generated by the proposed approach minus the ASO product for each elevation, slope and aspect belt. The results are represented for the 12 analyzed dates over the three hydrological season (2018-2021) for the South Fork catchment (cont.).